National Library of Canada

Acquisitions and Bibliographic Services Branch

395 Wellington Street
Ottawa, Ontario
K1A 0N4

Bibliothèque nationale du Canada

Direction des acquisitions et des services bibliographiques

395, rue Wellington
Ottawa (Ontario)
K1A 0N4

Your file Votre référence

Our file Notre référence

NOTICE

The quality of this microform is heavily dependent upon the quality of the original thesis submitted for microfilming. Every effort has been made to ensure the highest quality of reproduction possible.

If pages are missing, contact the university which granted the degree.

Some pages may have indistinct print especially if the original pages were typed with a poor typewriter ribbon or if the university sent us an inferior photocopy.

AVIS

La qualité de cette microforme dépend grandement de la qualité de la thèse soumise au microfilmage. Nous avons tout fait pour assurer une qualité supérieure de reproduction.

S'il manque des pages, veuillez communiquer avec l'université qui a conféré le grade.

La qualité d'impression de certaines pages peut laisser à désirer, surtout si les pages originales ont été dactylographiées à l'aide d'un ruban usé ou si l'université nous a fait parvenir une photocopie de qualité inférieure.

Canada

Temperature Dependence of the Electrical Resistivity in Quasicrystals

by

Massoud Akbari-Moghanjoughi

M.Sc. Thesis

Thesis submitted to the School of Graduate Studies and Research

of the University of Ottawa

in partial fulfilment of the requirements for the degree of

Master of Science

Department of Physics

University of Ottawa

Ottawa, Ontario

Canada

ISBN 0-612-11535-6

UNIVERSITÉ D'OTTAWA
UNIVERSITY OF OTTAWA

ABSTRACT

The applicability of the weak-localization theory to highly ordered quasicrystals raises the question of whether or not the long-range order in these alloys can be reconciled with the electronic disorder. This study did not detect any unusual structure-induced contribution to the resistivity at low temperatures other than those known for metallic glasses.

The temperature dependence of the resistivity in icosahedral quasicrystals of high structural quality showed that the transport behaviour of these alloys at low temperatures can be satisfactorily explained in terms of conventional weak-localization and electron-electron interaction theories. The temperature dependence of the resistivity in weakly disordered (low-resistivity) alloys can be explained qualitatively in terms of the classical theories extended to liquids and disordered alloys. The experimental evidence shows the existence of a close relationship between the icosahedral quasicrystalline structure and the weak localization tendency of the electronic states at the Fermi level. To explain the temperature dependence of the resistivity at high temperatures additional models based on the concept of the band transition and hopping have to be invoked.

In the high-resistivity stable icosahedral Al-Cu-Ru alloy the insulating-like (electron hopping) behaviour was found to dominate the electron transport even at low temperatures. This causes the deviations from the weak-localization theory and is due to the enhancement of the density of localized electronic states at the Fermi level. Consequently, the Anderson localization is collapsed in the vicinity of the metal-insulator transition.

The values of the correlation gap in the Al-Cu-Fe-Mn icosahedral system suggest a considerably different nature for the pseudogap around the Fermi level in amorphous and icosahedral phases. However, unless an ideal quasicrystal belongs to the metal-insulator transition region (if it exists), the weak-localization theory will be the most appropriate tool to investigate the low temperature electron transport properties in icosahedral phases.

ACKNOWLEDGEMENT

I would like to acknowledge the support of individuals and organizations, without which this work would not have been accomplished. I wish to thank Dr. Z. M. Stadnik, my thesis supervisor, for his guidance and advices. I would like to acknowledge the financial support from the Iranian Ministry of Culture and Higher Education. I would like to thank Profs. A.- P. Tsang and A. Inoue for providing the samples. I also thank the staff of the mechanical workshop, the electronics workshop, and the third year laboratory for their cooperation. Thanks are also extended to the workshop of the geology department for their assistance in cutting the samples.

Most of all, I wish to thank my family for their encouragement during the course of this study.

LIST OF CONTENTS

CHAPTER 1

INTRODUCTION

Since the discovery of the Al-Mn alloy with icosahedral point-group symmetry and no translational symmetry (Shechtman et al. 1984), much effort has been devoted to explore the expected unusual properties of this new class of materials. These alloys are known as quasicrystals (QCs). Before the year 1987 all of the QCs found were thermodynamically metastable. Since 1987 more than 20 thermodynamically stable QCs have been discovered. These stable QCs are characterized by the high structural quality comparable with that of the best crystalline alloys. X-ray diffraction (Stadnik and Zhang 1995), high-resolution electron microscopy (HREM) (Chen et al. 1990), transmission electron microscopy (TEM) (Angale et al. 1988), and scanning tunnelling microscopy (STM) (Kortan et al. 1990) investigations show a high degree of structural order for icosahedral (i) QCs. The crystallographic studies showed that the x-ray diffraction patterns of i-QCs can be indexed satisfactorily by the icosahedral point group symmetry. The quasicrystals occur predominantly as icosahedral and decagonal (d) (Bendersky 1985) alloys.

Full determination of a crystal structure of QCs is still an unsolved problem. The important question is whether new transport properties are associated with the quasiperiodic order characteristic of QCs. The first studies of the transport properties of QCs did not show a major deviation from the properties known for amorphous and

crystalline counterparts. However, as it became known later, the existence of a few percent of contaminant phases, phason strain (Goldman and Widom 1991, Lubensky et al. 1986) or dislocations in the studied samples can drastically change the transport properties of QCs. Phasons are elementary excitations associated with the local structural rearrangements in QCs. In many cases, dramatic changes in transport features are caused by small amount of fcc aluminum contaminant phase or approximant phases (Poon 1993) which may occur during the production of QCs. Often such a small amount of impurity (phase) can not be detected even in a high-resolution neutron or x-ray diffraction pattern. It has been shown experimentally (Mizutani et al. 1991, Kimura and Takeuchi 1991, Biggs et al. 1992) that annealing of an i-alloy for a few hours (typically 48 hours) can partly eliminate the phason strain, leading to a larger resistivity and to a larger temperature coefficient of resistivity (TCR). This is exactly opposite to the case of crystalline alloys in which an improvement of the sample structural quality lowers its resistivity.

QCs are characterized by an unexpected high resistivity. Also a small variation in their composition leads to a drastic change in the residual resistivity value. The recent discovery of stable QCs, such as Al-Cu-Fe (Tsai et al. 1987), Al-Cu-Ru (Tsai 1988), and Al-Pd-Re (Akiyama et al. 1993b) ternary systems, have initiated new experimental studies of these alloys. The resistivities in these alloys are much higher than those known for corresponding metallic glasses, and are usually associated with a negative TCR. In the newly discovered QCs of the Al-Pd-Re system the residual conductivity is 10 $(\Omega cm)^{-1}$ (ρ_0~0.1Ωcm) (Akiyama et al. 1993b). This is much lower than the Mott minimum

metallic conductivity of 200 $(\Omega cm)^{-1}$ (Mott 1987). The recent studies have revealed that high resistivity is an intrinsic property of QCs.

The origin of the high resistivity in stable QCs has been considered to be the combination of the two dominant effects. The first is associated with the existence of a wide pseudogap in the electronic density of states (DOS) at the Fermi level (Wagner et al. 1990, Pierce et al. 1993b), which is believed to be caused by a strong interaction between the Fermi surface and the Brillion-Jones zone boundary (FS-JZB) (Poon 1992). This effect has been related to the Hume-Rothery-like phase stabilization mechanism (Friedel 1988, Fujiwara 1994b). The second effect invokes the localization tendency of the electronic states near the Fermi energy (Kohmoto et al. 1983). The existence of the pseudogap at the Fermi level in QCs has been concluded from specific-heat (Wagner et al. 1988, Mizutani et al. 1990) and spectroscopic (Sadoc et al. 1993, Belin 1992) measurements.

Systematic studies of the resistivity show that the electron transport properties in both amorphous and quasicrystalline alloys can be explained in the scope of an identical theory, the so-called weak-localization theory. The weak-localization theory was originally developed for highly disordered systems (Lee and Ramakrishnan 1985). Therefore, it is concluded that QCs are electronically disordered. However, this seems to be at variance with the long-range order observed in the x-ray diffraction patterns. Some of the researchers believe that the application of Anderson localization theory to high-quality QCs is unjustified (Pierce et al. 1994). However, there still remains the question of applicability of this theory to highly ordered QCs.

Theoretical studies show (Lee and Ramakrishnan 1985) that a *finite* disorder in one and two dimensions will cause the electron localization, leading to a new type of electronic structure. Calculations for the Fibonacci chain (Kohmoto et al. 1983), which is a one-dimensional analog of the Penrose tiling, have revealed the localization tendency of electronic states. Consequently, the energy spectrum has been shown (Smith and Ashcroft 1987) to be singular continuous, i.e., neither continuous nor point-like. The eigen-states were shown (Kohmoto et al. 1987) to be critical, i.e., neither localized nor extended. The critical electronic states have also been suggested for two- and three-dimensional quasiperiodic structures (Niizeki and Akamatsu 1990).

Since the discovery of an insulating-like behaviour in the highly ordered Al-Pd-Re system (Pierce et al. 1994), which shows pronounced deviations from weak localization theory, several models have been proposed to describe the anomalous transport behaviour of QCs. Of these models, the variable range hopping (Tamura et al. 1995), local hopping between structural entities (Phillips and Rabe 1991), and band structure (Mayou et al. 1993) models are the best known. Band structure calculations (Smith and Ashcroft 1987, Fujiwara et al. 1994a) show sharp Van-Hove singularities in the DOS. The increased intraband transition resulting from the spiky structure (Fujiwara et al. 1993, Fujiwara 1989) in the calculated DOS leads to the enhanced electrical conductivity at higher temperatures and additional features in the optical conductivity (Burkov et al. 1992). The existence of the spiky structure in the calculated DOS (Fujiwara et al. 1993) with very narrow peak widths (typically of the order of 0.01-0.02 eV) supports the model associated with the band transition and local hopping of electrons at higher temperatures. These

transitions can occur between neighbouring states differing slightly in energy (Poon 1992). The strong compositional dependence of the quasicrystalline alloys has been also related to the band structure effect (Laissardière and Fujiwara 1994a, Carlsson 1991, Pierce et al. 1993c).

1.1) PURPOSE OF THE THESIS

In this work the temperature dependence of the resistivity in several i-QCs in the temperature range 10-300 K is studied. The question of the applicability of the weak-localization theory to quasicrystalline alloys, which may reveal the influence of the new structure on the electron transport properties, is addressed. The investigation of the electron scattering mechanisms in i-QCs, which is the main part of this study, may provide a useful picture of the electron behaviour in this quasiperiodic structure. The electron scattering phenomenon is studied in two subsections. First, the classical predictions for the disordered systems are applied to the QCs. Then, the temperature dependence of the resistivity in these QCs is studied in terms of the quantum interference effect. This study aims at finding possible deviations from the existing conventional theories.

1.2) SCOPE OF THE WORK

The temperature dependence of the resistivity in the temperature range 10-300 K in eight paramagnetic or diamagnetic and two magnetically ordered i-QCs is discussed within the framework of the classical and new quantum theories. The resistivity of an amorphous alloy has also been measured to compare the electron transport behaviour in different systems. The quality improvement due to the elimination of the crystalline phase by etching method has been also studied in the $Al_{62}Cu_{25.5}Fe_5Mn_{7.5}$ sample.

CHAPTER 2

THEORETICAL REVIEW OF TRANSPORT PROPERTIES OF ALLOYS

Many experiments on the electron transport properties of alloys have shown that the physical aspects of the electron transport in high-resistivity metallic glasses (amorphous alloys) can't be described by the classical theory. Even the treatment of the low-resistivity disordered alloys in the classical models, such as the nearly-free electron model, requires knowledge of the pseudo-potential caused by the disordered structure. For the interacting electrons in a highly disordered structure the electron wavevector **k** is no longer a good quantum number. Therefore, the concept of a well defined Fermi surface looses the meaning and the nearly-free electron assumptions become invalid . In the low mean-free path (strong disorder) limit, the electrons carry the charge diffusively rather than in a Boltzmann classical trajectory. As it will be discussed later, in this limit the electron transport behaviour can't be described in terms of the classical theories and the quantum corrections should be taken into account.

The classical and quantum theories developed to interpret the experimental data of disordered systems are discussed in this chapter. First the classical models are put forward to see how far the properties of metallic glasses and QCs can be understood in terms of the conventional theories and where they seem to be inadequate. Then the quantum corrections to the classical theories, which are nessesary to explain the transport properties of strong-scattering alloys, are reviewed. At the end of this chapter the variable

range hopping and phonon assisted tunnelling models, which describe the insulating-like behaviour observed in high resistivity QCs, are discussed.

2.1) FREE-ELECTRON MODEL

In this model the electrical resistivity arises only from the incoherent scattering of the electrons. Therefore, an ideal crystalline metal without any defects has infinite conductivity at absolute zero temperature. At finite temperature, the resistivity is caused by the thermal vibrations of ions. Other mechanisms of the electron scattering are caused by chemical impurities, defects, and surface scattering which (to a good approximation) are temperature independent. The electrical resistivity in this model can be described by the simple relation (Kittel 1986):

$$\rho = m/ne^2\tau \quad , \tag{1}$$

where ρ is the resistivity, τ is the electron scattering relaxation time, n is the electron density, and m is the electron mass. The electron scattering rate, which is the reciprocal of the scattering relaxation time, can be considered as the sum of several terms, such as elastic, inelastic, impurity scattering, etc. The anomalous electron transport behaviour caused by the band structure of the material can't be understood within this model.

2.2) NEARLY-FREE ELECTRON THEORY

This model explains (Kittel 1986) the unusual electronic transport properties, such as the positive Hall coefficient, the band transition in semiconductors, and many other electron transport aspects which could not be described by the free-electron model. The problem of impurities, defects, and topological disorder in crystalline materials can be approximately treated in the scope of the perturbed Bloch states. Introduction of the Bloch states in this model does not introduce an additional mechanism for the resistivity in a crystalline system since the resistivity is caused only by the incoherent scattering of electrons. In the liquid (disordered) metals and amorphous alloys the Bloch assumption is not valid and the problem of evaluation of the transport phenomenon depends on the knowledge of the potential caused by the disorder. The problem of the resistivity calculation in disordered systems is twofold. The first problem is how to treat the amorphous structure, which is still unsolved. The second problem is how to calculate an electron-wave packet diffracted from this structure. The nearly-free electron theory was extended to disordered systems by Ziman in 1961 (Ziman 1961). Ziman's model overcomes both problems associated with the resistivity treatment by the direct use of the experimental structure factor. Consequently, the electron scattering probability is calculated from the experimental x-ray or neutron diffraction pattern.

2.3) ZIMAN MODEL

In the original Ziman model it is assumed that the electrons in the alloy can be described by plane waves and consequently the concept of the Fermi surface is well defined. This is applicable only in the limit of $k_F l_e >> 1$, where k_F is the Fermi wavevector and l_e is the electron mean-free path. This condition is fulfilled only for low-resistivity amorphous and liquid metals. However, for high-resistivity disordered alloys the disorder parameter ($k_F l_e$) can be of the order of unity (Howson and Gallagher 1988). This model also assumes that the Born approximation is valid, i.e., the scattering potential interacting with the electrons can be treated by the first order perturbation theory. This treatment can be carried out by choosing an appropriate pseudo-potential, which is not unique and which requires detailed knowledge of the partial structure factor. Finally, the model assumes that $k_F l_e > 1$ for which the Boltzmann equation is applicable. The last assumption is implicitly mentioned in the first ($k_F l_e >> 1$).

The above assumptions are all satisfied for simple amorphous and simple liquid metals and good agreement between the experiment and the theory is achieved. However, the effect of s-d scattering, which causes the high resistivity in transition-metal containing alloys, is not considered in this model. This model also neglects the multiple scattering effect which causes the deviations from the Boltzman transport equation for highly disordered systems. In principle, the interference of waves from different scattering centres should be taken into account (multiple scattering). In the Ziman model only the interferences between waves from a pair of atoms are taken into account (first order

perturbation).

The current is assumed to be carried by an unmodified free-electron band. Therefore, this model is unable to explain the electron transport in liquid transition metals in which hybridization or mixing of the bands play an important role in controlling the free-electron DOS at the Fermi level. To obtain the exact magnitude of the resistivity in the Ziman model one needs to calculate the relative intensity of the scattered wave from the structure factor and combine it with the cross section of an individual ion. Integration of the scattering probability of an individual electron over all possible k-vectors within the Fermi surface leads to the resistivity formula (Howson and Gallagher 1988):

$$\rho = \left(\frac{3\pi n e^2}{\hbar m \upsilon_F}\right)\int_0^1 |V(q)|^2 S_\rho(q)\, 4\left(\frac{q}{2k_F}\right)^3 d\left(\frac{q}{2k_F}\right) \quad , \tag{2}$$

where $V(q)$ is the corresponding pseudo-potential, $S_\rho(q)$ is the resistivity structure factor, v_F is the Fermi velocity, and k_F is the Fermi wavevector. The temperature dependence of the resistivity in this model comes from the temperature dependence of the structure factor.

The appropriate integral for the resistivity structure factor (given below) contains a weight function which takes into account the inelastic scattering of the electrons by phonons, within the energy range of ~kT, and the elastic contribution. The following expression describes the resistivity structure factor in terms of the experimental structure

factor (Howson and Gallagher 1988):

$$S_\rho(q) = \int_{-\infty}^{+\infty} d\omega S(q,\omega) \frac{x}{(e^x - 1)} \quad , \tag{3}$$

where $x=\hbar\omega/kT$ and $S(q)$ is the measured structure factor from the conventional x-ray diffraction pattern. At temperatures comparable to the Debye temperature (θ_D), the effect of the weight function becomes small and the resistivity structure factor will be essentially the same as the experimental structure factor.

At low temperatures the elastic electron-phonon scattering contribution is reduced by the Debye-Waller factor with increasing temperature (Howson and Gallagher 1988). Then, the low temperature ($T<\theta_D$) dependence of the resistivity becomes:

$$\rho(T) = \rho_0(1 - aT^2) \quad , \tag{4}$$

where ρ_0 is the residual resistivity, and $a>0$. The magnitude of the inelastic contribution is expected to be twice larger than that of the elastic contribution and it leads to the increase of the resistivity with increasing temperature (Howson and Gallagher 1988). Consequently, the resistivity changes the form to:

$$\rho(T) = \rho_0(1 + aT^2) \, . \tag{5}$$

The $+T^2$ dependence has been observed in many low-resistivity amorphous alloys, such

as $Fe_{80}B_{20-x}C_x$ (figure (1)), and is known to be a characteristic of the multiphonon scattering in disordered systems. However, for some of the high-resistivity alloys a $-T^2$ term is found instead of $+T^2$ term. To interpret this inconsistency within the Ziman model, this effect has been related to the *phonon ineffectiveness* in the low mean-free path regime. The phonon ineffectiveness occurs when the inelastic scattering of the short mean-free path electrons by the long wavelength phonons becomes less dominant (Howson and Gallagher 1988). The Ziman model is successful in describing the temperature dependence in simple (non-transition) crystalline and amorphous alloy. However, this model is unable to describe the negative TCR observed in many amorphous alloys since the contribution from the inelastic scattering is always larger than the elastic contribution.

2.4) TRANSITION METALS AND ALLOYS

These metals and alloys are characterized by atoms with unfilled d or f bands. Electrons in these alloys can be scattered to the high density and unfilled d or f band. In the transition metal containing alloys the scattering of the s electrons introduces an additional resistivity mechanism. The d wave functions of electrons in these alloys overlap less in comparison to the s or p wave functions and form narrower and flatter d bands with a high DOS. Consequently the s and p electrons have higher velocities than d electrons and carry most of the current. The modification of the s bands due to the presence of a half-filled d band is called the *hybridization* effect. The hybridization effect (figure (2)) strongly modifies the shape of the dispersion curves, leading to a "S" shaped band structure (figure (3)).

The hybridization effect also leads to anomalous transport behaviour, such as the positive Hall coefficient (Dugdale 1987) in the strong hybridization case. The resulting negative group velocities, obtained for electrons within the energy range of E1 and E2 (figure (3)) leads to a positive Hall coefficient. The sign change of the Hall coefficient with temperature has been observed in QCs (figure (4)) which is believed to be due to the band structure effect (Howson and Gallagher 1988). The unusual negative magneto-conductivity in some of the transition metal containing alloys has also been related (Howson and Gallagher 1988) to the hybridization effect.

2.5) EXTENSION OF THE ZIMAN MODEL TO TRANSITION METALS

In order to evaluate the electron transport in a transition-metal containing alloy, one has to take into account the s electron scattering into unfilled d states. Many attempts have been made to extend the Ziman theory to transition-metal containing disordered systems. The major problem is to choose the right pseudo-potential which describes the interaction between the free-electron s bands and the unfilled *localized* d bands. By using a muffin-tin model Evans et al. (Evans et al. 1971) extended the Ziman theory to the transition metals and alloys. The main difference between this model and the original Ziman model is that Evans' model does not rely on the Born approximation. The resistivity is assumed to arise from the back scattering of the incoming electron waves from the d states. The interference of the free-electron wave with the back-scattered waves causes a resonance state, the so-called *virtual bound* state (Friedel 1958), with a finite life time of $\hbar/\Gamma$, where Γ is the energy of the resonance state. The following expression is obtained from Evans' model for the resistivity (Kaul et al. 1986):

$$\rho \approx \left(\frac{30\pi^2\hbar^3}{meE_F k_F \Omega_0}\right)\sin^2(\eta_2(E_F))S_T(2k_F) \quad , \tag{6}$$

where E_F is the Fermi energy, Ω_0 is the atomic volume, $\eta_2(E_F)$ is the d partial-wave phase shift, and $S_T(2k_F)$ is the temperature dependent structure factor.

The structure factor is defined by:

$$S_T(k) \cong 1 + (S_E(k)-1)\exp(-2W_k(T)) \quad , \tag{7}$$

where $S_E(k)$ is the equilibrium structure factor and $\exp(-2W_k(T))$ is the Debye-Waller factor. $W_k(T)$ in the Debye approximation is given by:

$$W_k(T) = W_k(0) + 4W_k(0)[\frac{T}{\theta_D}]^2 \int_0^{\frac{\theta_D}{T}} \frac{zdz}{(\exp(z)-1)} \quad , \tag{8}$$

where:

$$W_k(0)=3\hbar^2k/8Mk_B\theta_D . \tag{9}$$

Here M is the atomic mass, k is the wavevector, and k_B is the Boltzmann constant. The exact integration from equation (8) gives:

$$\rho_{str} \approx (\frac{30\pi^2\hbar^3}{meE_Fk_F\Omega_0})\sin^2(\eta_2(E_F))$$

$$\times [1 + (S_0(2k_F)-1)\exp(-2(W(T)-W(0))] . \tag{10}$$

$S_0(2k_F)$ is the equilibrium structure factor at 0 K, W(0) is defined by equation (9) with $k=k_F$, and the subscript *str* represents the resistivity which is caused by the potential of the disordered structure. The exponent W(T) can be estimated for low-temperature ($T<\theta_D$) and high-temperature ($T\geq\theta_D$) limits as $W(0)+4W(0)\pi^2/6(T/\theta_D)^2$ and $4W(0)(T/\theta_D)$,

respectively. The low-temperature dependence of the resistivity varies as T^2 and is similar to that predicted by the original Ziman model. However, the coefficient of the Debye-Waller factor in equation (10) is the controlling factor for the sign the TCR. Therefore, a negative TCR can be explained by this model. At high temperatures the expansion of the Debye-Waller factor leads to a quadratic polynomial function. The quadratic term at high temperatures is introduced by taking into accout the higher-order term in the Debye-Waller factor. This quadratic temperature dependence should not be confused with the T^2 term caused by the electron-magnon scattering in magnetic alloys (Kaul et al. 1986). The quadratic form of the temperature dependence of the resistivity is commonly observed in many metallic glasses and QCs (figure (5)). The low- and high- temperature dependencies can be expressed as:

$$\rho = \alpha_0' + \alpha_1' T + \alpha_2' T^2 \qquad \text{(high-T)} \quad (11a)$$

$$\rho = \alpha_0 + \alpha_2 T^2 \qquad \text{(low-T)} \quad (11b)$$

The Debye temperature in this model is approximated as:

$$\theta_D \approx \pi^2 \alpha_1' / 6(\alpha_2 - \alpha_2') \, . \qquad (12)$$

Also, the TCR (α) is defined as (Kaul et al. 1986):

$$\alpha = [8W(0)(1-S_0(2k_F))/\theta_D] \, / \, [S_0(2k_F)+(2W(0)(1-S_0(2k_F))((4T_0/\theta_D)-1)] \, . \qquad (13)$$

It is evident from the estimated α (TCR) value that the TCR is negative if $S_0(2k_F)>1$ and positive if $S_0(2k_F)<1$. The observed magnitude of the α_2' in equation (11a) is much smaller than the magnitude of the linear term (α_1') for the low-resistivity alloys (Kaul et al. 1986). The magnitude of the T^2 term in equation (11a) depends on the coefficient of the Debye-Waller factor ($1-S_0(2k_F)$) and is indirectly linked to the Fermi velocity via the k value in equation (9).

Mott (Mott and Jones 1936) used a similar approach to calculate the resistivity of liquids and amorphous transition metals and alloys. His approach is based on the fluctuations in the local environment (due to the structural disorder) and assuming that the mean-free path of the s electrons is much larger than that of the d electrons. Similarly to the Ziman and Evans' models, it is assumed that the conduction is caused by an unmodified free-electron band. However, the electrons are assumed to be more tightly bound and the high resistivity arises from the high density of the d states at the Fermi level. The s-d scattering rate can be written as (Howson and Gallagher 1988):

$$\tau^{-1} = \frac{2\pi N_d(E_F)}{N\hbar}\left(\int_V \psi_{sp}^{*} V(r)\psi_d dr\right)^2 \quad , \tag{14}$$

where $N_d(E_F)$ is the density of the d states at the Fermi level, N is the total number of atoms, and V(r) is a suitable pseudo-potential. For the crystalline case, the term in the parenthesis (integral) gives the degree of hybridization. For a disordered system (in which the k selection rule breaks down), equation (14) gives the s-d electron scattering probability.

This approach approximates the resistivity as:

$$\rho = \rho_0(1 - \frac{1}{6}\pi^2 k^2 T^2 [3(\frac{d(lnN_d)}{dE})^2 - d^2\frac{(lnN_d)}{d^2E}]|_{E_F}) \qquad (15)$$

From equation (15) one gets an almost temperature independent resistivity since the derivative of the d-DOS can be negligibly small at the Fermi level because of the flat structure of the d-bands.

In the Evans' approach the main contribution to the resistivity comes from the temperature dependence of the structure factor, while the small temperature dependence in the Mott model comes from the broadening of the Fermi function. Therefore the Mott model predicts an almost temperature independent resistivity for the transition-metal containing alloys.

2.5.1) THE GENERALIZED FABER-ZIMAN MODEL

This model attempts to explain the unusual negative TCR observed in many high resistivity disordered alloys. The temperature dependence of the resistivity in the generalized Ziman model (Mizutani 1983) comes from two components. The first component is the Debye-Waller factor which lowers the resistivity with increasing temperature. This decrease of the resistivity is due to the quasi-elastic (combination of elastic and inelastic) contribution of the phonon scattering and is occasionally called the multiphonon scattering. The second component is the inelastic contribution which always

increases the resistivity with increasing temperature. Therefore, the temperature dependence of the resistivity is determined by a delicate interplay between the two competing terms. The temperature dependence of the resistivity can be written as (Mizutani 1993a):

$$\rho(T) = \exp(-2W(T))(\rho_0+\Delta\rho) \quad , \tag{16}$$

where the exponential term is the Debye-Waller factor and the second term (in the parenthesis) is the inelastic contribution. The second term in the formula plays a similar role as the coefficient of the Debye-Waller factor in the Evans' formula of the resistivity and controls the sign of the TCR. At low temperatures the contribution of the inelastic scattering is very small and the temperature dependence predicted by this model is essentially the same as that from the original Ziman model. At higher temperatures where $T \approx \theta_D$ one can assume a linear temperature dependence for $\Delta\rho$ (Yung-ping and Dian-lin 1994). The Debye-Waller factor can be expanded at higher temperatures. Then, the following dependence can be obtained for high temperatures:

$$\rho(T) = (1-\beta T)(\rho_0+\alpha T) = \rho_0 + (\alpha - \rho_0\beta)T - \alpha\beta T^2 \quad , \tag{17}$$

where it was assumed that (Yung-ping and Dian-lin 1994):

$$\exp(-2W(T)) \approx 1 - 2W(T) \approx 1 - \beta T. \tag{18}$$

In equation (17) ρ_0 is the residual resistivity, α is the parameter describing the electron-phonon interaction, and β is the parameter describing the phonon-phonon coupling. The temperature dependence of the resistivity in the high- and low-temperature limits in this model is identical with that from the Evans' model, although the mechanisms are slightly different. The phonon-phonon coupling parameter can be estimated as: $\beta=8W(0)/\theta_D$, using the high-temperature term for the Debye-Waller exponent (Kaul et al. 1986), i.e., $W(T)\approx 4W(0)T/\theta_D$.

2.6) MOOIJ CORRELATION

The origin of the negative TCR in disordered alloys has been a matter of debate for a long time. An extensive compilation of the data on disordered systems shows the existence of a correlation between the TCR and the residual resistivity in amorphous alloys (figure (6)). This has been known as the Mooij correlation and seems to be a common feature of disordered systems. The correlation indicates (Tsuei 1986, Kaiser 1986) that for amorphous systems the TCR changes sign at 150 $\mu\Omega$cm (figure (6)). Mizutani studied the temperature dependence of amorphous systems (Mizutani 1983) and QCs (Mizutani 1993a). He pointed out that the Mooij correlation holds only for the d electron systems (transition-metal containing systems) and that the sign change of the TCR for the s systems (simple alloys) occurs at much lower resistivity value (around 50 $\mu\Omega$cm).

A negative TCR in the Ziman model occurs when the upper limit $2k_F$ of the

integration (equation (2)) coincides with the wavevector k_p corresponding to the first peak in the structure factor. Frésard et al. (Frésard et al. 1990) used a muffin-tin effective medium approximation (EMA) formalism to evaluate the multiple scattering effect and showed that the sign of the TCR changes when the energy crosses the conductivity minimum induced by the Bragg reflections. By evaluating a large number of alloys Kaiser (Kaiser 1987) concluded that both the increase of the mean-free path with temperature and the incipient localization are needed to account for the negative TCR. As will be shown later in section 2.8, the inelastic electron-phonon and electron-electron scattering are the dominant cause of the TCR sign change in the highly disordered systems. Therefore, for a strong-scattering alloy the weak localization effects are essential to explain the sign and the magnitude of the TCR.

2.7) SCATTERING FROM TWO-LEVEL STATES (TLS)

It has been observed in many amorphous alloys and QCs (Kimura et al. 1988, Akiyama et al. 1993a) that the resistivity at low temperatures varies as log(T). This effect, which can not be explained in terms of the existing classical theories, has been ascribed to the tunnelling effect. It is based on the fact that in amorphous systems different groups of atoms can have different equilibrium positions, and thus can be in different states, and tunnelling between these states can occur. The formulation of the TLS effect has been reviewed by Baeck and Czycholl (Baeck and Czycholl 1984). It is based on the coherent potential approximation transport theory which shows a good agreement with the

experimental findings.

The TLS effect is analogous to the Kondo magnetic scattering effect in the sense that both effects show a log(T) dependence of the resistivity (Kimura and Takeuchi 1991) at low temperatures. The Kondo magnetic scattering, which arises from the scattering of the electrons from magnetic impurities, is usually associated with a shallow resistivity minimum (figure (7)) at low temperatures (Akiyama et al. 1992a). It was concluded from the magnetoresistance studies (Howson and Gallagher 1988) that in some cases the shape of the resistivity minimum is not changed in a magnetic field. Therefore, this minimum is not likely to be caused by the Kondo effect. Rapp et al. (Rapp et al. 1982) showed that the low-temperature anomaly can be best described by a $T^{1/2}$ term, which suggests an electron-electron interaction effect. Kaiser (Kaiser 1986) suggested a mechanism involving both the TLS and the localization that could contribute to the $T^{1/2}$ term at low temperatures.

2.8) WEAK-LOCALIZATION OR QUANTUM INTERFERENCE EFFECT (QIE)

2.8.1) MULTIPLE SCATTERING EFFECT

The experimental studies show that the temperature dependence of the resistivty in highly disordered alloys can't be described by the classical models. For instance, in most of the metallic glasses and QCs the low-temperature resistivity changes as $T^{1/2}$, instead of as T^2 predicted by the classical models. The extended Ziman model explains

the negative TCR in disordered alloys only qualitatively. However, the classical models do not give any insight into the scattering mechanisms involved in the electron transport phenomenon. The magnitude of the TCRs observed in metallic glasses also can't be understood in terms of the classical models. Apart from the facts mentioned above, many other transport anomalies can't be explained within the framework of the classical models.

In order to go beyond the Boltzmann picture the idea of the electron motion in a classical trajectory should be abandoned. Short mean-free path electrons in highly disordered alloys, including QCs, have a diffusive motion rather than a free-flight propagation (Dugdale 1987). The resulted electron elastic mean-free path for the high-resistivity metallic glasses and QCs (Matsuo et al. 1993) are as low as the interatomic distances in a crystalline metal (Kittel 1986). This means that the electrons are elastically diffused from site to site in a very small volume and the electronic states are weakly localized. The origin of this localization comes from the fact that the probability of returning of an electron to the starting point is by no means negligible. In this regime the interference of the electron wave from different scattering centres in the small volume tends to enhance the localization effect. This interference occurs because the scattered electron waves from different centres (figure (7)) are produced in the very small time intervals. Therefore, these almost instantly produced scattered waves can combine and localize the electron. The time interval between the two elastic scattering events is the elastic scattering relaxation time. The very small elastic scattering times have been reported for many high-resistivity metallic glasses and QCs (Matsuo et al. 1993). Thus,

the multiple scattering effect can enhance the resistivity by localizing the electrons. The formalism of the multiple scattering effect in electron transport of disordered metals has been reviewed by Frésard et al. (Frésard et al. 1990).

2.8.2) WEAK LOCALIZATION (WL) EFFECT

Multiple elastic scattering enhances the probability of returning the scattered electron to its starting point. This causes the electron localization and gives rise to an additional source of resistivity. At low temperatures, where the elastic scattering is dominant, the scattered electron wave in one direction in a closed path can combine with the wave scattered in the opposite direction in the same closed path. This causes a phase coherence between the two partial wave functions. If it is assumed that the probability of returning the particle to its starting point over all possible paths is:

$$W = \sum_i |\psi_i|^2 \quad , \tag{19}$$

where $|\psi_i|^2$ is the probability of returning of the electron from path i, then the probability for an identical path can be written in the form (Dugdale 1987):

$$W = |\psi_1|^2 + |\psi_2|^2 + \psi_1^* \psi_2 + \psi_1 \psi_2^* . \tag{20}$$

Here ψ_1 is the clockwise and ψ_2 is the anticlockwise direction wave-function. It is

concluded from equation (20) that the total interference term (in the case of phase coherence) gives a value twice larger than the classical value (the sum of the first two terms). However, any process which destroys this phase coherence, such as the inelastic scattering, will reduce the additional resistivity. This can explain the Mooij correlation observed in high-resistivity strong elastic scatterers, in which the introduction of inelastic scattering with increasing temperature leads to the negative TCR. A detailed review of the WL effect is given by Lee and Ramakrishnan (Lee and Ramakrishnan 1985).

In the three dimensional diffusion equation the probability of finding a particle at spacial element dr and in a time interval of dt is given by (Dugdale 1987):

$$p(r, t)drdt = 4\pi Dt^{\frac{-3}{2}} \exp(\frac{-r^2}{4Dt}) drdt \quad , \tag{21}$$

where D is the diffusion constant. The resistivity caused by the QIE is proportional to this probability. The integration of this probability from τ_0, the elastic scattering time, to τ_i, the inelastic scattering time, gives: $\rho \propto (\tau_0)^{1/2} - (\tau_i)^{1/2}$. This result indicates that the temperature dependence of the resistivity due to the WL effect is determined by the temperature dependence of τ_i. It also implies that the interference effect is completely turned off when $\tau_0 = \tau_i$ which is an indication of the saturation in the WL effect. More recently, Plenet et al. (Plenet et al. 1992) have studied the magneto-resistivity of $Al_{100-x}Fe_x$ quasicrystalline alloys and have found a T^{-2} dependence for τ_i above 36 K. A similar result had already been reported for amorphous metals by Bieri et al. (Bieri et al. 1984). Therefore, the WL theory predicts linear temperature dependence for the conductivity at

low temperatures (figure (9)). It is observed (Poon 1992) that in amorphous metals the $\sigma(T) \propto T$ behaviour changes over to $\sigma(T) \propto T^n$ at higher temperatures. This indicates that the electron-phonon inelastic scattering time can no longer be explained by a simple T^{-2} dependence. The quantum correction to the conductivity which takes into account the elastic (τ_o), inelastic (τ_i), and spin-orbit (τ_{so}) scattering is given by Fukuyama and Hoshino (Fukuyama and Hoshino 1981). The simplified conductivity expression (Fukuyama and Hoshino 1981) is obtained by assuming that $\tau_{so} \gg \tau_i, \tau_0$:

$$\sigma'(T) = A[3\sqrt{1+t} - \sqrt{t}] + \sigma_o, \quad A = \left(\frac{\sqrt{3}e^2}{2\pi^2 l_e \hbar}\right)\sqrt{(\tau_o/\tau_{so})}, \tag{22}$$

where:

$$t = \tau_{so}/4\tau_i, \quad \sigma_o = (4e^2/3\pi^2 l_e)(E_F\tau_o)^2 . \tag{23}$$

The experimental studies show that equation (22) well describes the experimental data for quasicrystalline alloys below 20 K (Sahnoune et al. 1992, Haberkern et al. 1993). In the case of strong spin-orbit scattering, the spin-orbit scattering time can be comparable to the inelastic scattering time. Therefore, one needs to use a more accurate equation to fit the experimental data.

By exact integration of the magneto-conductivity formula Matsuo et al. (Matsuo et al. 1993) have obtained the precise quantum correction to the conductivity expression, i.e.,:

$$\sigma'(0, T) = (A/\pi)[-2\sqrt{t} \times \tan^{-1}(1/\sqrt{t_1}) + \sqrt{(t_2+4)/t_1} \times \tan^{-1}(1/\sqrt{t_2+4}) -$$

$$3\sqrt{(4t_1+t_2+4)/t_1} \times \tan^{-1}(1/\sqrt{4t_1+t_2+4}) + 3\sqrt{(4t_1+t_2)/t_1} \times \tan^{-1}(1/\sqrt{4t_1+t_2})$$

$$+ (1/2\sqrt{t_1})\{\log(\frac{t_2+5}{t_2+1}) + 3\log(\frac{4t_1+t_2+1}{4t_1+t_2+5})\}] \quad , \qquad (24)$$

where:

$$A = \frac{\sqrt{3}e^2}{2\pi^2\hbar v_F}\sqrt{\tau_o\tau_{so}}, \quad t=\tau_{so}/4\tau_i, \quad t_1=3\tau_o/\tau_{so}, \quad t_2=3\tau_o/\tau_i. \qquad (25)$$

Here $\tau_i = \tau_{io}T^p$ and p is the power of inelastic dephasing. Equation (24) is more informative in giving the transport parameters than equation (22) and can be fitted to the experimental data to higher temperatures (Matsuo et al. 1993). To obtain the full expression for conductivity one needs to add this quantum correction term to the normal Boltzmann conductivity. The total conductivity function becomes:

$$\sigma(0, T)=e^2DN(E_F) + \sigma'(0, T) \quad , \qquad (26)$$

where the first term is the Boltzmann contribution. From the fitting of equation (24) to the experimental data one obtains the scattering parameters, such as the temperature

dependence of the inelastic scattering, $\tau_{so}/4\tau_{io}$, $\tau/4\tau_{io}$, l_e and the Boltzmann conductivity. However, by using the approximate equation (22) only the magnitude of $\tau_{so}/4\tau_{io}$ and the power of dephasing rate can be deduced.

The dephasing of the phase coherence is not limited to the inelastic scattering but is also caused by the electron-electron scattering. For the strong-scattering alloys the application of the WL theory results in a value ~1.5 for the dephasing power parameter. The $\tau_i \sim T^{1.5}$ is known to be the characteristic of the electron-electron scattering in the strong scattering limit, the so-called dirty limit (Sahnoune et al. 1992). This limit is characterized by $k_F l_e < 1$. A general relation for the temperature dependence of the electron-electron dephasing rate can be written as (Altshuler and Aronov 1985, Schmid 1974):

$$\frac{1}{\tau_{ee}} = \frac{1}{3}\frac{(kT)^2}{\hbar E_F} + \sqrt{3}\frac{(k_F l_e)^{\frac{3}{2}}(kT)^{\frac{3}{2}}}{2(\hbar\sqrt{E_F})}. \qquad (27)$$

The T^2 term in equation (27) corresponds to the weak-scattering limit. However, for the inelastic scattering rate the general form of T^p ($2<p<4$) is present (Sahnoune et al. 1992). It is concluded that a T^2 dependence of the inelastic scattering rate is predicted for both inelastic electron-phonon and electron-electron scattering effects. However, the power of the temperature dependence of the inelastic scattering can be a determining factor for the degree of disorder in alloys. A major criticism (Howson and Gallagher 1988) of the WL theory is that it is valid only for the limit $k_F l_e > 1$. However, for most of the high-resistivity amorphous or quasicrystalline alloys this parameter is of the order of unity or even less (Matsuo et al. 1993). It was mentioned (Coffey et al. 1984) that the condition $k_F l_e > 1$ can

be relaxed to $k_F l_e \geq 1$ since the higher order corrections in the perturbation term in the WL theory have insignificant effect.

The applicability of the WL theory to the high-resistivity metallic glasses and QCs is still being debated (Pierce et al. 1994). However, the observed temperature dependence of the resistivities in high-quality stable QCs is in agreement with the prediction of the WL theory (Kimura and Takeuchi 1991). Hence, a close relationship is claimed to exist between the WL and the quasicrystalline structure (Akiyama et al. 1992a).

(2.8.3) SPIN-ORBIT INTERACTION AND WL EFFECT

The spin of the electron is a quantum characteristic of an electron wave function. In the case of the strong spin-orbit coupling, i.e., when $\tau_{so} \approx \tau_i$, the spin of the electron changes the direction. The incoming electron wave recombines with the back-scattered wave and the phase coherence between the two waves randomizes quickly (Dugdale 1987). The time for this to occur is characterised by the temperature independent spin-orbit scattering time which depends on the spin-orbit coupling strength. However, if the inelastic collision time is long as compared to τ_{so} then the spin-orbit effect will destroy the constructive interference between the spin triplet states (Dugdale 1987). Consequently, the quantum interference effect will be reversed to the antilocalization effect (Dugdale 1987). In order to show this formally, consider the electron spin in the triplet state (the singlet state gives rise to the normal interference efffect). Then the interference term

becomes (Dugdale 1987):

$$I = \frac{1}{2} \times \{ \sum_{m} |\psi_{lm}|^2 - |\psi_{00}|^2 \} \tag{28}$$

where m=1,0,-1 is the spin state and $|\psi_{00}|^2$ is the classical probability of finding an electron in its starting point. In the absence of the spin-orbit coupling $\psi_{1m}=\psi_{00}$ and the summation gives $I=|\psi_{00}|^2$. This is the classical probability. However, if $\tau_{so}>\tau_i$, the spin-orbit effect dominates and ψ_{1m} randomizes rapidly, giving $I=-1/2|\psi_{00}|^2$. This is the half of the classical value. The negative sign indicates the fact that the strong spin-orbit case is an antilocalization effect (figure (10)) and results in a positive TCR. This strong spin-orbit scattering acts only at very low temperatures since by increasing the inelastic rate at higher temperatures this effect is weakened. The low-temperature resistivity maximum (Akyiama et al. 1992, Sahnoune et al. 1992) has been related to the competition between the localization (caused by the inelastic scattering) and the antilocalization (due to the spin-orbit scattering) effects.

2.9) ELECTRON-ELECTRON INTERACTION (EEI)

It is well known that in strong-scattering alloys, such as metallic glasses, the conductivity varies as $T^{1/2}$ at low temperatures (typically below 36 K) (Howson and Gallagher 1988, Chernikov et al. 1993). This square-root anomaly is ascribed to the electron-electron or Coulomb interaction. Experimental results of the resistivity

measurements show (Chernikov et al. 1993) that even at very low temperatures (100 mK), where no inelastic scattering occurs, the QIE exists. The dephasing of the phase coherence at very low temperatures is ascribed to the electron-electron interaction effect. Altshuler and Aronov (1985) (Altshuler and Aronov 1985) developed a theory that describes the electron-electron scattering mechanism which causes the QIE at low temperatures. It is not easy to have a classical picture of this effect. Aronov (Aronov 1993) and Dugdale (Dugdale 1987) gave a useful semiclassical approach to the effect, which will be followed here. In this explanation an electron which goes round a closed path creates a charge pattern, the so-called an electron hologram, which is a record of the phase shift in the closed path. If the second electron wave goes round the *same* path in the *same* direction and receives the *same* phase shift, the phase shift of the electron wave can be restored and enhanced by the hologram. In this way a holographic interference can enhance the electron-wave function, creating a mutual interference effect. The case of an electron pair of opposite spins results in a more familiar phenomenon, i.e., superconductivity effect. In this case the coupled electrons carry the current in a multiple elastic scattering media without an attenuation in the wave-function. Both the Coulomb attraction (superconductivity) and the Coulomb interaction (EEI) can dominate the low temperature transport behaviour.

To calculate the temperature dependence of the EEI effect, consider the fact that the energy of the interacting electrons is limited to the range kT. Hence, a thermal coherence time, τ_i, is associated with each interacting electron. Integration of the three dimensional diffusion equation (21) from τ_0 to $\tau_i \sim \hbar/kT$ gives: $\rho \propto T^{-1/2}$. Therefore, the

conductivity due to the EEI effect varies as $T^{1/2}$ (figure (11)). At higher temperatures the effect is overwhelmed by other dominant effects. The EEI effect is independent of the magnetic field since the two electrons traverse the same path in the same direction.

2.10) PHONON-ASSISTED TUNNELLING AND HOPPING MODEL

For a disordered alloy the quantum interference is expected to become less dominant at higher temperatures since the inelastic scattering rate increases and destroys the phase coherence. This occurs when the inelastic scattering time becomes comparable to the elastic scattering time. Therefore, one expects the negative TCR caused by the WL, to become positive. The temperature dependence of the conductivity of the $Al_{62.5}Cu_{25}Fe_{12.5}$ and $Al_{65}Cu_{20}Ru_{15}$ strong-scattering i-alloys (Mayou et al. 1993) show continuous increase in the conductivity up to 1000 K. The increase of the conductivity in the absence of the WL effect may be explained in terms of the non-metallic phonon-assisted tunnelling. This behaviour has been reported for the Al-Co-Ni d-system (Martin et al. 1991).

The theoretical analysis (Tsunetsugu and Ueda 1991) of one- and two-dimensional QCs has shown that the electron wave functions are of the power law decaying type, i.e., $\Psi \propto r^{-\nu}$, where $\nu>0$. The overlap integral of the states separated by distance r is proportional to $r^{2\nu/\beta}$, where β is the dimensionality. Then the predicted conductivity becomes $\sigma=\sigma_0+AT^n$ with $n<1$ (Mott 1987), where σ_0 is due to the tunnelling effect between the electronic states (Pierce et al. 1993a, Poon 1992). It has been shown (Tamura et al. 1995,1994a) that the high-resistivity i-alloys, such as Al-Cu-Ru and Al-Pd-Re

(figure (12)), can be fitted well, based on the variable range hopping model (Mott and Davis 1971). The hopping of the electrons in insulators and semiconductors can be described by $\rho \propto \exp(AT^{-1/4})$ which was predicted by Mott. This temperature dependence of the resistivity has been observed in high-resistivity amorphous alloys (Xiao and Chien 1986).

The existence of the electron hopping behaviour in metallic alloys is due to the enhanced localized states and the vicinity of the metal-insulator transition (Xiao and Chien 1986). Therefore the very high resistivity found in the newly discovered Al-Cu-Re icosahedral alloys ($\rho \sim 0.1 \Omega$cm) may be an indication of the metal-insulator transition. Klein et al. (Klein et al. 1991) evaluated the residual ($\sigma(0)$) and the room temperature conductivity for high-quality i-alloys. They found that most of such alloys lie on a line in the plot of σ_0 vs. σ_{300}, where σ_0 and σ_{300} are respectively the residual and room temperature conductivities. This line has often been refered to as the metal-insulator transition line.

2.11) PROPOSED SCATTERING PICTURE FOR NON-PERIODIC SYSTEMS

The existence of the Mooij correlation for QCs and amorphous systems together with the metallic-glass-like (Rapp 1993) behaviour observed in QCs indicate the close similarity of the transport mechanisms in these systems. Mizutani (Mizutani 1993a) has given a unified interpretation of scattering mechanisms in both systems. He classified these systems into five different groups depending on the temperature dependence of the

resistivity. The classified alloys (figure (13)) vary from the weak or sp-scattering to the strong-scattering systems. The *a*, *b*, and *c* type conductors, in which the sp electrons are the dominant charge carriers, follow the normal Boltzmann mechanism and the Ziman theory is applicable to them. The strong-scattering systems are characterized by higher resistivities and TCRs. These systems can't be described within the classical theory (types *d* and *e* in figure (13)). It has been shown experimentally (Klein et al. 1992) that for the strong-scattering alloys γ_{exp} (the electronic specific coefficient) is well below (about one third) the free-electron value. This results in a much lower free-electron DOS at the Fermi level. The electronic specific heat coefficient is related to the free-electron DOS by:

$$\gamma = (\frac{1}{3})\pi^2 k_B N(E_F) . \tag{29}$$

The electron mean-free paths for these type of alloys are of the order of the interatomic distances. The corresponding Fermi velocity ($\upsilon_F = l_e/\tau_o$) is also much lower than that for a crystalline alloy. The g factor is defined by Mott relation (Mizutani 1993a):

$$\sigma = \frac{1}{3} e^2 g^2 l_e \upsilon_F^{free} N(E_F)^{free} , \tag{30}$$

where:

$$g = N(E_F)^{exp}/N(E_F)^{free} = \upsilon_F^{exp}/\upsilon_F^{free} = R_H^{free}/R_H^{exp} . \tag{31}$$

The studies of the $(Ag_{0.5}Cu_{0.5})_{100-x}Ge_x$ amorphous system have shown (Mizutani 1993a) that the g factor is reduced with increasing the residual resistivity (ρ_0). This decrease in the g follows the above relationship (equation (30)). The g-σ_0 graph shows a sharp cut-off at g=1 which corresponds to the weak-scattering limit. The g value then starts to level off at about 300 $\mu\Omega$cm (figure (14)). The decrease of l_e with increasing ρ_{300} shows a rather slow dependence at higher resistivities and seems to saturate around the Mott minimum metallic conductivity value ($200\Omega^{-1}cm^{-1}$) (figure (15)). It is concluded that the increase in ρ_{300} is due to the decrease in the electron mean-free path only in the limit ρ_{300}<300 $\mu\Omega$cm. In the strong-scattering limit, where the l_e becomes comparable to the interatomic distances, the temperature dependence is mostly determined by the decrease in g or the density of the charge carriers. This indicates that in the strong scattering alloys one expects much lower charge carrier density at the Fermi level than in a normal alloy. The low density of charge carriers has also been concluded (Pierce et al. 1994) from the specific heat measurments for QCs. The presence of this effect (low free electron DOS) in amorphous and quasicrystalline alloys has been related (Wagner et al. 1990) to the existence of a wide pseudogap at the Fermi level. The existence of such a pseudogap is considered to have an important role in the stability of QCs (Poon 1992).

SUMMARY

Several facts can be concluded from the above review:

1-The original Ziman model only explains the transport properties in weakly disordered alloys. However, when the mean-free path is lowered by the high rate of elastic scattering, the multiple scattering effect should be taken into account.

2-In the Evans' model low mean-free path alloys can be described provided that the low mean-free path or high resistivity arises from the presence of the unfilled d band at the Fermi level, which causes the s-d scattering. The concept of a negative TCR can be qualitatively understood within this model.

3-The Mott model predicts an almost temperature independent resistivity and is appropriate for the alloys in which the s-d scattering is a dominant scattering mechanism. This model can not explain the high negative TCR observed in some alloys. The s-d scattering, which is dominant in the transition-metal containing alloys, can introduce large resistivities with negligibly small TCRs. Hence, these alloys are more prone to deviate the Mooij correlation.

4-In the generalized Ziman model a high negative TCR can be explained qualitatively. However this model is unable to give a proper insight into the scattering mechanisms. It also does not give a quantitative explanation of the magnitude of the TCR in the strong-scattering alloys.

5-The WL theory is successful in explaining the transport anomalies in the strong-scattering alloys. The only condition for the application of this theory is that it can be

applied in the limit $k_F l_e > 1$. According to this theory the dephasing of the phase coherence in weak-scattering alloys is due to inelastic electron-phonon scattering if the dephasing varies as T^p ($2<p<4$). The dephasing of the form $T^{1.5}$ always corresponds to the electron-electron scattering in the strong-scattering limit (dirty limit). The dephasing of the form T^2 can be due to either electron-phonon or electron-electron interaction in the weak-scattering regime.

6-For the phonon assisted tunnelling or hopping model one expects a temperature dependence of the form $\sigma=\sigma_0+AT^n$ ($n<1$) for metallic alloys. For insulators the temperature dependence of the form $\rho \propto \exp(AT^{-1/4})$ is expected. The electron hopping behaviour dominates at high temperatures and can be an indication of the reduced carrier density at the Fermi level.

7-High resistivity is not necessarily introduced by strong disorder but can be due to the low mean-free path caused by the s-d scattering. In strong scattering alloys the transport properties are mostly governed by the reduction in the g factor (and consequently by the reduction in the density of charge carriers and in the Fermi velocity) The electron mean-free path in these alloys can be even higher than that in weak-scattering alloys.

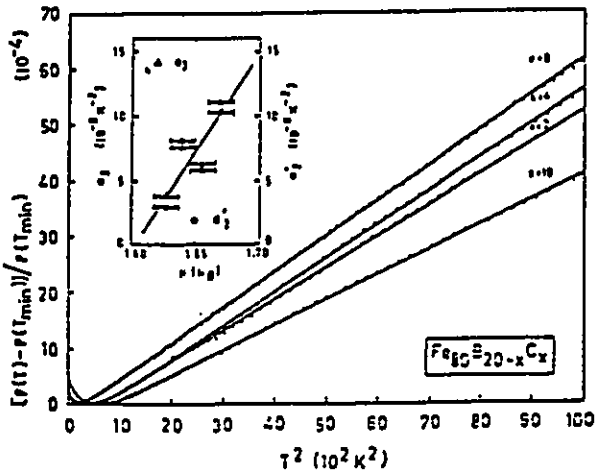

Figure 1: Straight lines through the data serve as guide lines to Ziman T^3 dependence in a-$Fe_{80}B_{20-x}C_x$ amorphous alloys (Kaul et al. 1985).

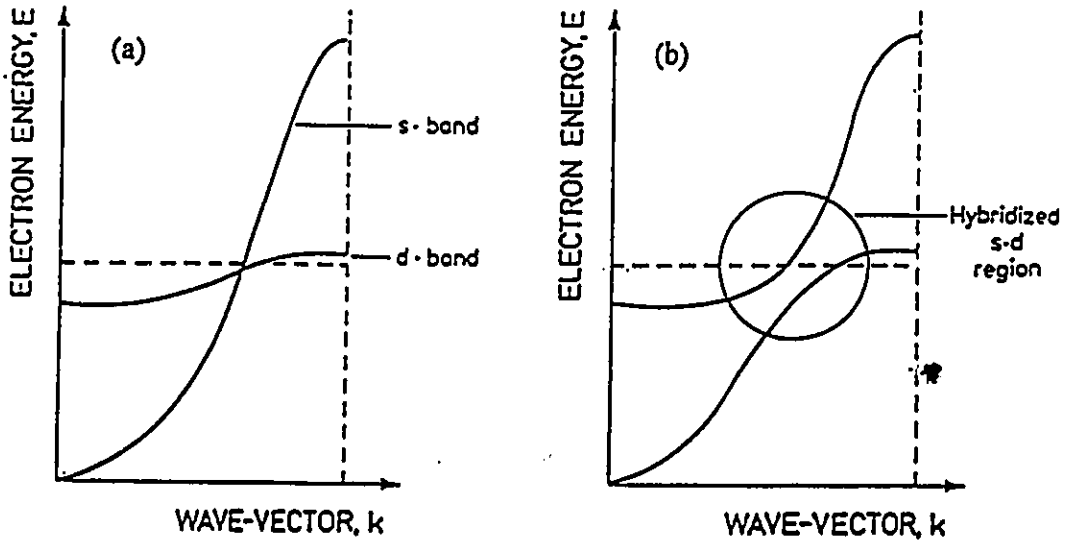

Figure 2: Electron energy against wave-vector in a given symmetry direction of a crystalline metal (a) without (b) with hybridization between the s-like and d-like branches (Dugdale 1987).

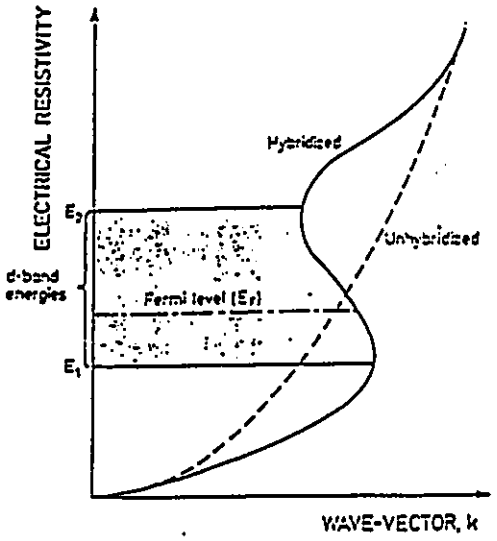

Figure 3: The effect of s-d hybridization on the dispersion curve of the s-like band. In the energy range between E_1 and E_2, where the d band crossethe s band, the two bands repel each other creating an s-shaped band (Dugdale 1987).

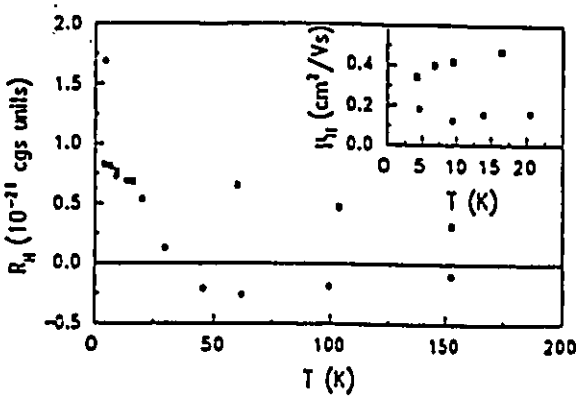

Figure 4: Hall coefficient and mobility (inset) for $Al_{70.5}Pd_{21}Re_{8.5}$ quasicrystalline alloy (Pierce et al. 1994).

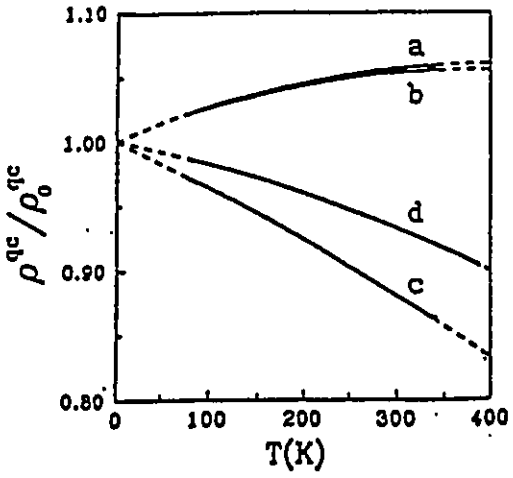

Figure 5: The normalized resistivity in the quasicrystalline plane. The solid curves are measured data, and the dashed lines are their quadratic polynomial fits ($A+BT+CT^2$) to the following decagonal alloys: (a) Al-Cu-Co No-1, (b) Al-Ni-Co, (c) Al-Si-Cu-Co, (d) Al-Cu-Co No.2 (Yung-ping and Dian-lin 1994)

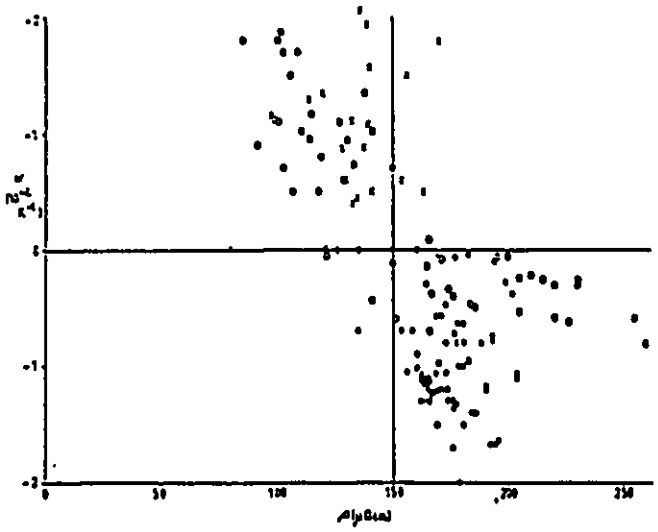

Figure 6: Mooij plot for a large number of different alloy systems: ○metal-metal, ●metal-metalloid, ×ferromagnetic alloy (Howson and Gallagher 1988)

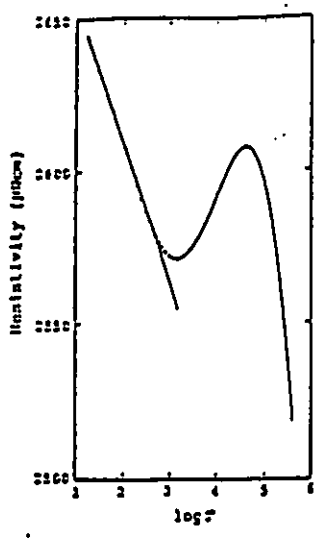

Figure 7: Temperature dependence of the resistivity at low temperatures in poly-grained Al-Pd-Mn quasicrystalline sample ploted in a logT scale (Akiyama et al. 1993a).

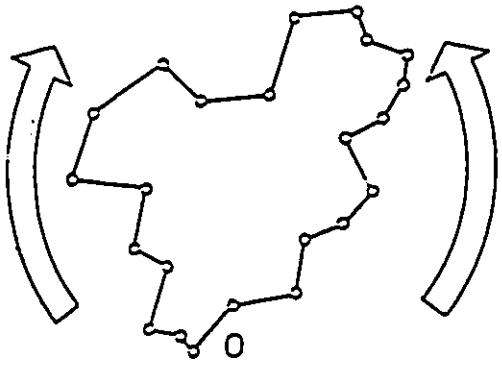

Figure 8: Closed path of an electron moving diffusively under the influence of elastic scattering from ions (Dugdale 1987).

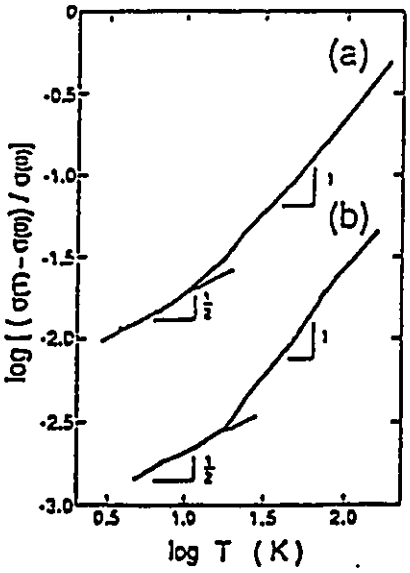

Figure 9: Temperature dependence of conductivity on a log scale for as-quenched icosahedral (a) $Al_{61.5}Cu_{25}Ru_{13.5}$ and (b) $Al_{63}Cu_{29}Ru_{13.5}$ QCs. The slope is 0.5 below about 15K and 1.0 above 36K (Nakamura and Mizutani 1994).

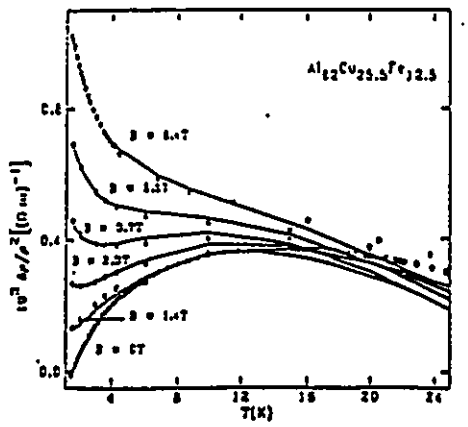

Figure 10: Low-temperature dependence of the resistivity of i-Al-Cu-Fe in a magnetic field. The negative TCR is progressively recovered as the field increases as a result of the destruction of the spin-orbit effect (Sahnoune et al. 1992)

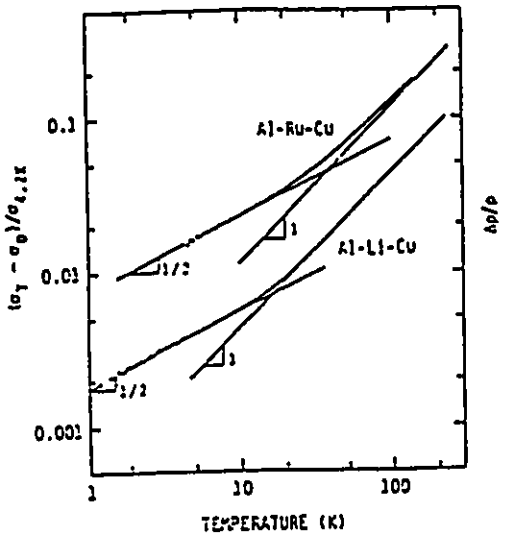

Figure 11: The normalized conductivity to 4.2K values vs. temperature on a log-log scale for Al-Li-Cu i-phase and Al-Cu-Ru i-phase (Kimura and Takeuchi 1991).

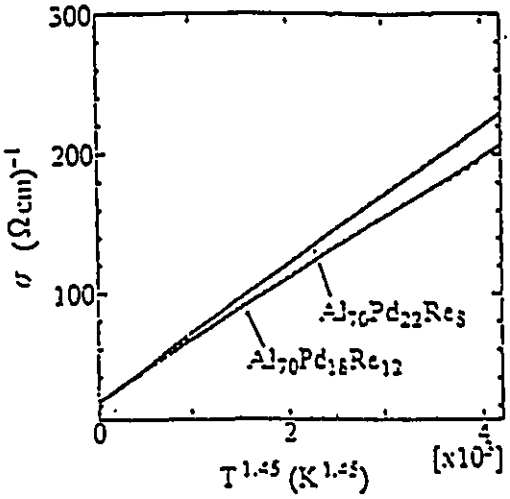

Figure 12: Electrical conductivity plotted against $T^{1.45}$ for $Al_{70}Pd_{18}Re_{12}$ and $Al_{70}Pd_{22}Re_8$ QCs (Tamura et al. 1995)

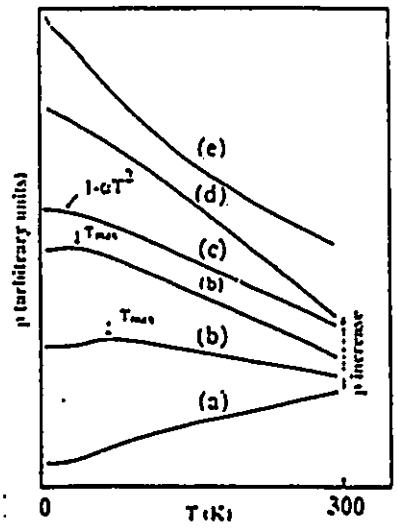

Figure 13: The observed non-metallic temperature dependence for amorphous alloys, quasicrystals, and their corresponding approximant phases (Mizutani 1993a).

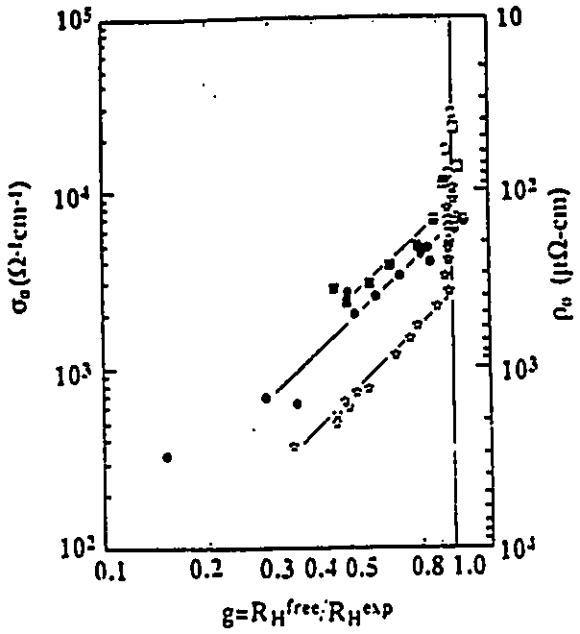

Figure 14: Conductivity or resistivity at 300 K as a function of the g factor. Circle variants: amorphous Ag-Cu-Ge alloys, square variants: amorphous Ca-Mg-Ga alloys, and stars: expanded liquid mercury. Different symbols for respective amorphous alloys are used to differentiate the ρ-T type: open for type (a), that with a horizontal bar for type (b), half-filled for type (c), and solid for types (d) and (e) (Mizutani 1993a)

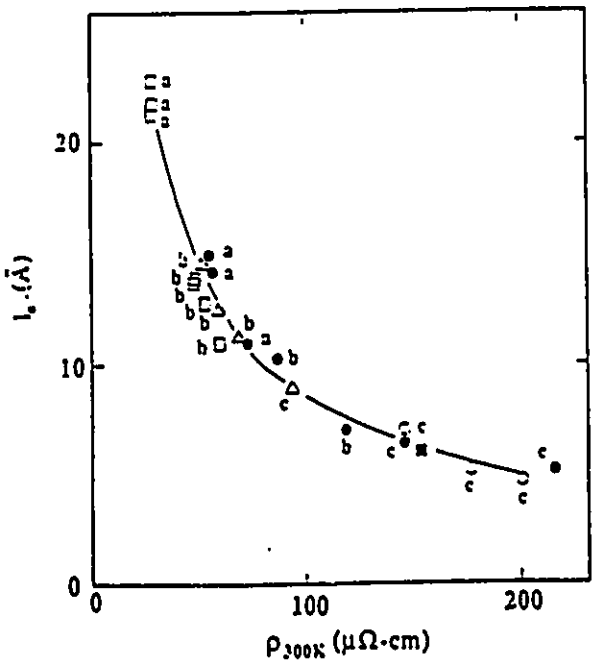

Figure 15: Mean-free path l_e as a function of resistivity for sp-electron amorphous alloys. The temperature dependence types of the resistivities are also indicated. Open circles: Ag-Cu-Ge, filled boxes: Ag-Cu-Si, triangles: Mg-Ga-Zn, filled circles: Ca-Mg-Al, and open squares: Ag-Cu-Mg (Mizutani 1993a).

CHAPTER 3

EXPERIMENTAL PROCEDURE

The resistivity measurement system consists of two major parts: 1) cryostat, 2) hardware. A simple cryostat is used to cool down the sample to the desired temperature. A temperature controller provides the control and monitor of the sample temperature. The microvoltmeter and nanoammeter are used to measure the voltage and the current applied to the sample, respectively. The hardware of the system consists of a conventional four-probe dc wiring for the resistivity measurement, as well as the temperature sensor wiring and the heater wiring to control the temperature. The hardware uses an IEEE standard digital interface to control the electronic meters. The IEEE-488 bus is a control bus designed to allow the control and data collection from instruments through a remote controller or a computer. The computer is used to perform the resistivity measurement on an automated basis. Also the driver program (the software) provides a routine for desired data acquisition from the meters. Then the collected data, simultaneously from the multimeters and the thermometer, are accumulated and stored on a 286-PC computer hard-disk through the interface remote lines.

3.1) SYSTEM DESIGN

Making an accurate measurement of the resistivity is associated with several

technical difficulties. Because of the small size of the samples and the corresponding low values of the resistances, the resistivity measurement requires several considerations. For these low-resistance materials the current of several milliamps are needed to be measured within a high accuracy. Electronic instruments, such as multimeters, put limitations on their accuracy once being used for low-voltage or low-current measurements. A low-level measurement is defined as a measurement which is close to the theoretical limit (Keithley 1984). The accuracy is also limited to the values of the lead resistances since the voltage noise produced in the measurement loop is proportional to the square root of the resistance. Therefore, high lead resistances limit the theoretical sensitivity of the measurement. Apart from these practical problems, there are other phenomenological effects, such as magnetic and electric field interference, ground-loop current, and the thermal emf's, which need additional considerations.

The resistances of the samples used in the measurements range from a few miliohms to several ohms. These low resistances require a four-wire technique. Four-probe dc method, which eliminates the lead resistances effect (Peltser 1988), is conventionally used for low-resistance measurements (Saito et al. 1994, Kimura et al. 1990, Takeuchi et al. 1993). One of the advantages of this method is that the electrical wiring is quite simple. It consists of two wires that bring the current into the sample and another couple of wires which pick up the voltage drop across the sample. The detailed description of the electronics is given in section 3.1.2.

3.1.1) CRYOSTAT

The cryostat consists of a liquid nitrogen dewar, a liquid helium dewar, a sample chamber, and an electrical insert. The liquid dewars are used to maintain the cold liquids for the required amount of time. Figure (1) shows schematically the different parts of the cryostat. The liquid nitrogen dewar (part M), which is the outermost part of the cryostat, is made of two separated cylindrical steel containers that are connected to each other on the top. This dewar, when under good vacuum, isolates thermally the inside of the container from the outside. The liquid helium container (L) is quite similar, but relatively smaller in size. This dewar is appropriately mounted inside the liquid nitrogen dewar by a mechanical clamp (T) of low thermal conductivity. The high vacuum valves (H,R) are used to control the pressures inside the dewars in order to control the isolation. The gas vents (G) let out the pressurized nitrogen and helium gases above the liquid nitrogen (J) and the liquid helium (I) levels. Also, the inlets (S,Q) are used to fill the containers with the corresponding liquids.

The sample chamber (K) is made of a long single-layer cylindrical steel tube, closed at the bottom, and open on the top which is immersed into the liquid helium. This chamber is centrally fixed in the liquid helium container by means of a low-thermal conductor clamp. The electrical insert (N) is the innermost part of the cryostat and carries the internal wirings (D) to the sample holder (P) which is located at the coldest part of the sample chamber. The sample holder contains a 25 Ω solenoid which is used as a heater (O). The head of the insert (U) is made of a light aluminum alloy and consists of

two vacuum-tight feedthroughs (C) which connect the inside wirings to the electrical outlets (B). The vacuum valves (E) are attached to the head on the top and are used to control the pressure inside the sample chamber. The height of the insert can be adjusted by means of the top screw (A) connecting the steel rod to the head.

Different parts of the electrical insert are shown in figure (2). The electrical outlets (cables) are carried to the sample through the internal delicate wirings (L) which are wrapped around the long steel rod (K) (the electrical insert). The sample holder, which is screwed to the end of the insert, holds the heater (B), the temperature sensor (E), and the sample (D) inside the sample chamber very close to the bottom. The temperature sensor is embedded inside the sample holder near to the flat surface on which the sample is located on a glass substrate (H). The glass substrate is attached to the sample holder by means of Apiezon-N grease (G), which is used as a good thermal conductor. The current wires (F) and the voltage wires (C) are also shown in this figure.

3.1.2) ELECTRONICS

Apart from minor low-current phenomena, such as triboelectric, piezoelectric, space charge, and electro-chemical effects (Keithley 1984)) that can cause noise current as high as 10 nA in the circuit, there are low-voltage phenomena which can introduce significant errors. Thermal emf's are the most common sources of errors in low-voltage measurements. These error voltages are produced either when different parts of a circuit are at different temperatures or when different materials are joined to make an electrical

contact. For instance, the thermal emf caused in a Cu-Cu connection is estimated as 0.2 μV/°C. The thermal gradient which causes this effect can be partially controlled by using a cold trap that thermally connects all of the wires to a large thermal mass. An alternative method to cancel the emf errors is to use a quasi-dc technique. In this method the measured voltage across the sample, V_1, is compared to the voltage with the reversed current, V_2. If the second voltage reading is accomplished before the thermal gradient change, the thermal emf's cancel in the final calculations (Peltser, 1988). This method requires a special current source with an automated current switch mode.

In order to minimize the thermal emf effect all of the connections other than sample connections are chosen to be Cu-Cu connections. The only connections which may cause major emf errors are sample-Cu connections. The emf errors caused by sample-Cu connections can also be minimized by keeping these connections at the same temperature. Therefore, the connections are attached to a thin glass substrate and located on the copper disk (sample holder), which is considered to be a large thermal mass and also a good thermal conductor. The Apiezon-N grease is used to make a good thermal contact between the glass substrate and the copper disk. Considering the fact that the sample to substrate contacts are made of silver paint, which is also a good thermal conductor, the error caused by thermal emf will be almost negligible.

The ground loop is another important effect that can cause error when the electronic equipment is connected to different grounds. A simple solution to prevent this effect is to connect all of the electronic elements to a single common ground. For instance, the body of the cryostat can be a good common ground for all of the electronic

instruments.

The next important effect is magnetic or electric field interference. Magnetic and electric fields are produced by electronic and electrical devices. Once the magnetic or electric flux passes through the measurement electronic circuit, the error current or voltage is induced in the measurement circuit. This phenomenon can be effectively controlled by using shielded or coaxial wires in different parts of the electronic circuit which are exposed to the field.

Figure (3) shows the block diagram and the layout of the electronic system. The multimeters are connected to the cryostat (A) through the triaxial shielded wires (E). These multimeters and the thermometer are interfacible and capable of communication through the listen/talk commands. The electronic devices are all connected to the interface, which is installed in a 286 PC-computer, by the interface remote lines. The interface uses a GPIB link (general purpose interface bus) to compile the driver program.

The thermometer reads the voltage of a silicon diode (temperature sesnor (C)) and converts it to the corresponding temperature value, based on a specified calibration curve. Then, the temperature is displayed on a digital monitor. The silicon diode is calibrated for the 1-325 K temperature range. The accuracy of the thermometer is 0.01 K in the 0-100 K temperature range. The voltmeter is a 4½ digit Keithley digital multimeter (DMM), with the accuracy of 0.04% (of the reading) + 3 (counts) and reads the direct voltage across the sample. The ammeter is a similar DMM with an accuracy of 0.2% (of the reading) + 2 (counts) in the 20 nA current range. The ammeter is in series with the current source, which supplies a regulated current up to 100 mA.

3.1.3) SOFTWARE

A driver program, written in the BASIC language, creates a routine to control the devices through the GPIB link. The corresponding program is given in the appendix "A". Each electronic device is defined by a primary and a secondary address. The electronic meters are addressed to talk or to listen through the IEEE-488 specific commands. The controller asks the device to standby or send the collected readings in an appropriate time intervals (timeout).

The timeout settings are implemented based on the individual instrument read rate. Through the IEEE-488 bus, the microvoltmeter makes a voltage reading in 700 ms and the output from the ammeter takes 600 ms. Since two readings are required to calculate the resistance, this process takes a total time of 2600 ms. Hence, the timeout for this measurement can't be less than 2.6 s. The default timeout setting in the driver program is 30 s for all of the instruments, which is enough time for the system.

3.2) SAMPLE PREPARATION

Quasicrystalline samples can be produced by several techniques. More commonly, these samples are produced in two different forms: either as ingots or as ribbons. Ingot samples are produced by melting the required amounts of the alloy in an arc-furnace in a low pressure argon atmosphere. Then, the homogenously melted ingot is solidified slowly to the room temperature. At the end, the produced master ingot is annealed at a selected temperature for a few hours and is fast water-quenched (Saito et al. 1994, Takeuchi et al. 1993). Ribbon samples are generally produced by fast quenching of the melt. In this method, the prepared master ingot is remelted instantly in a quartz tube under a rf field. Then, the corresponding melt is injected onto a high speed rotating wheel and is quenched in thin ribbon shapes (Kimura et al. 1987). The samples produced by the first method (ingots) are thermally stable, while the ribbon samples are not. Ribbon samples are the most common for the resistivity studies because of two main reasons. First, because of the relatively higher resistances of the ribbon samples, higher accuracy is achieved in the resistivity measurements. Second, they can be produced in a long ribbon shapes, which are more flexible at low temperatures and can be easily attached to any substrate.

One of the important processes in the resistivity measurement is preparing samples which are strain and stress free at low temperatures. Special care must be taken in making electrical connections which stay fixed at low temperatures. Ribbon samples are very thin (10 to 20 μm thickness) and therefore extremely fragile. Making the good electrical

contact is another practical problem associated with the ribbon samples. Unfortunately, most of the ribbon samples can't be soldered by the normal soldering method. Therefore, one needs to look for other ways of making good electrical contacts. Aluminum or gold soldering methods can be used for this purpose. But then a part of the sample may be transformed into the amorphous phase.

Making electrical contacts by silver paint or paste is known as a reliable method for the resistivity measurement purposes (Saito et al. 1994, Kimura et al. 1990, Takeuchi et al. 1993). Silver paint is a highly conductive material in the liquid form which can be applied to make contacts without heating the sample. The applied amount of this material can dry in a few (typically five) minutes. It remains a good conductor down to the lowest temperatures. The only difficulty associated with the application of silver paint is that in order to make good electrical contacts all the surfaces should be completely clean of dirt.

Surface cleaning is a necessary step in the sample preparation (Biggs et al. 1990). In some cases, the metal oxides produced on the surface of the sample cause large contact resistances. Etching (Kimura et al. 1990) is one of the effective methods to remove the surface contaminations and the phase impurities. Some of the workers (Kimura et al. 1990) in the quasicrystalline field believe that etching for a long time (five days) can help to eliminate fcc Al or amorphous contaminant phases, which are produced in quasicrystalline alloys during the fast quenching of the melt (Biggs et al. 1990).

In the ingot samples regular parallelepiped pieces were cut from the master ingots, using a diamond cutter, for the volume resistivity measurements. Then the irregularities on the surface were removed by means of a sand-paper. Uniform ribbons of length

typically 2 cm and with an appropriate curvature were chosen for the resistivity measurement. The typical width of the ribbons was 1 mm and the thicknesses varied from 10 to 20 μm. It should be noted that having the appropriate curvature is very important in keeping the sample strain and stress free at low temperatures. Samples were left in the 50% nitric acid for three hours to clean the dirt from the surface (etching). Some of the samples were etched for a longer time (60 hours) in order to evaluate the Al-fcc crystalline phase effect on the resistivity. For one of the samples the resistivity measurement was carried out in two different stages: the shallow etching (three hours) and the deep etching (60 hours) in order to compare the results.

Figure (4) shows the electrical connections on both kinds of the samples. The electrical contacts were made using the highly conductive silver paint and paste. In the ribbon samples, the two ends of the ribbon were silver glued onto a thin glass substrate (C) of thickness 0.1 mm and then a bundle of copper wires (D) was glued onto the silver paints (I) by means of silver paste (J,E). Silver paste was mainly used to keep the sample fixed on the substrate at very low temperatures. Then, two fine copper wires of 40 μm diameter (A) were spot-painted (F) onto the middle points of the sample for the voltage measurement.

In the ingot samples, two copper foils (G) of the thickness 0.05 mm and the area 1 mm^2 were painted onto the flat ends of the parallelepiped sample (B). Then a couple of wires (D) were soldered (I) to the copper foils by normal soldering method. Next, 40 μm copper wires (A) were attached to the middle points (F) by use of silver paint. The thin voltage wires were also silver glued (E) to the glass substrate (C).

The active dimensions of the parallelepiped samples were measured using a 1/100 mm micrometer. The voltage wire distances were measured by a 1/20 mm travelling microscope. The ribbon thickness, width, and length were measured by a 2/1000 mm micrometer, a 1/20 mm travelling microscope, and a flexible scaled paper (1/2 mm), respectively. The maximum relative errors of 7% for ingots and 20% for ribbons were estimated for the volume measurement. Considering the irregularities on the surface and the edges in the ribbon samples, the error can even exceed the estimated error value.

3.3) PROCEDURE

The resistivity measurements were carried out in a quasi-dynamic way in the sense that the readings were taken every 30 s with a maximum heating rate of 0.0067 K/s. At the beginning, all of the samples were tested in the temperature range of 77-300 K. Then, the lower temperature measurements, i.e., 10-77 K, were carried out for the ribbon samples with the least amount of fluctuation in the resistivity data. It was concluded that, generally, the magnitude of the scattering in the resistivity data for the ribbon samples was comparably lower than that in the ingot samples. Only the Al-Cu-Ru icosahedral ingot sample showed a reasonably low fluctuation in the resistivity data. The origin of the high fluctuation in the other ingot samples could not be determined.

The liquid nitrogen container was leak-detected and tested under a high-vacuum and confirmed to maintain the liquid nitrogen for few (two-three) days. However, the

high-vacuumed liquid helium dewar was not able to maintain the liquid helium more than six hours. The liquid nitrogen and the helium dewars were pumped down to the pressure of 10^{-7} mbar and fixed in their positions. This pumping took three-four days. The sample was attached to the holder and located inside the sample chamber. Then, the sample chamber was pumped down to 10^{-3} mbar and filled with the required amount of the helium gas.

For the first part of the measurement, i.e., in the range 77-300 K, the internal container was filled with the liquid nitrogen up to 3/4 level. After cooling down the sample to the liquid nitrogen temperature, the remaining liquid was pumped out and the system was let to heat steadily up to the room temperature. At the same time the program was run and the data points were collected every 30 seconds. The heating cycle was chosen instead of the cooling because of two main reasons. First, the presence of the unexplained artifacts, which only occurred during the cooling process at specific temperature range, was noticed. Second, the natural heating in the cold nitrogen gas provided a much steadier and nearly uniform rate of the temperature change. The natural heating up to the room temperature took typically 12 hours for each sample.

For the samples measured at lower temperature range (10-77 K), the procedure was nearly the same. At the beginning both containers were filled with the liquid nitrogen and the system was let to reach the liquid nitrogen temperature. Then, the remaining liquid nitrogen in the helium container was pumped out and the container was filled with the required amount of the liquid helium (about three litres for each sample). After the liquid helium evaporated, the system started to heat up steadily. The maximum heating

rate at low-temperature measurements was 0.2 K per 30 seconds (0.0067 K/s). After about five hours the sample reached the liquid nitrogen temperature. A large number of data points obtained from both temperature ranges (10-77 K and 77-300 K) were combined and plotted in a single graph. This was done by shifting the high temperature set of data with respect to that for the low temperatures in order to match the resistivity at the liquid nitrogen temperature. The magnitude of the shift did not exceed 100 μΩcm.

The reproducibility of the measurement was verified for several samples after thermal cycling of the samples. The results of two individual measurements (before and after heat cycling) for the sample of icosahedral $Al_{62}Cu_{25.5}Fe_{10}Mn_{2.5}$ were indistinguishable. Also different pieces of the same sample were measured separately. The result of this test showed only a slight shift in the resistivity curve, which was consistent with the error of the volume measurement.

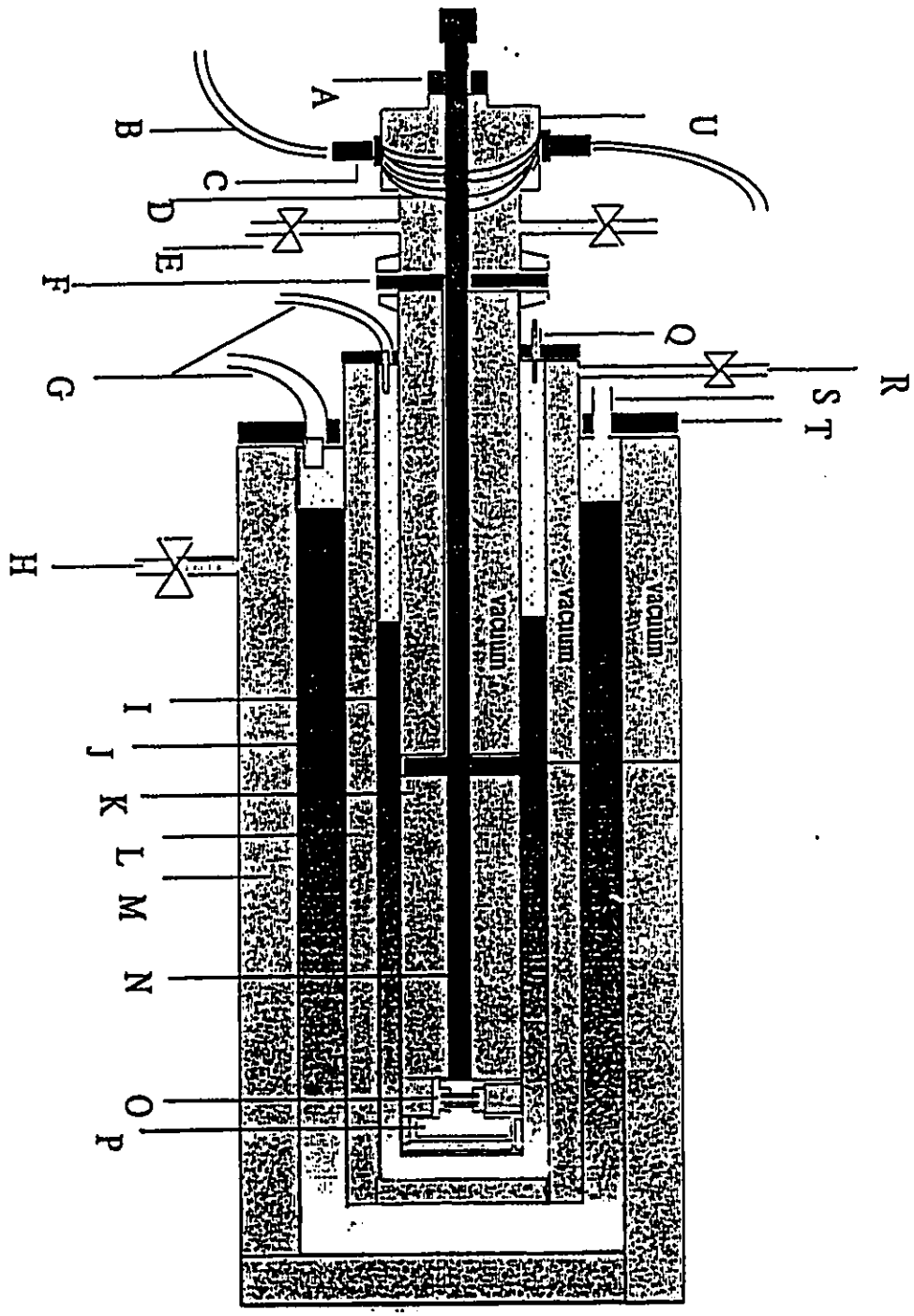

Figure 1: Different parts of the cryostat used for the resistivity measurement.

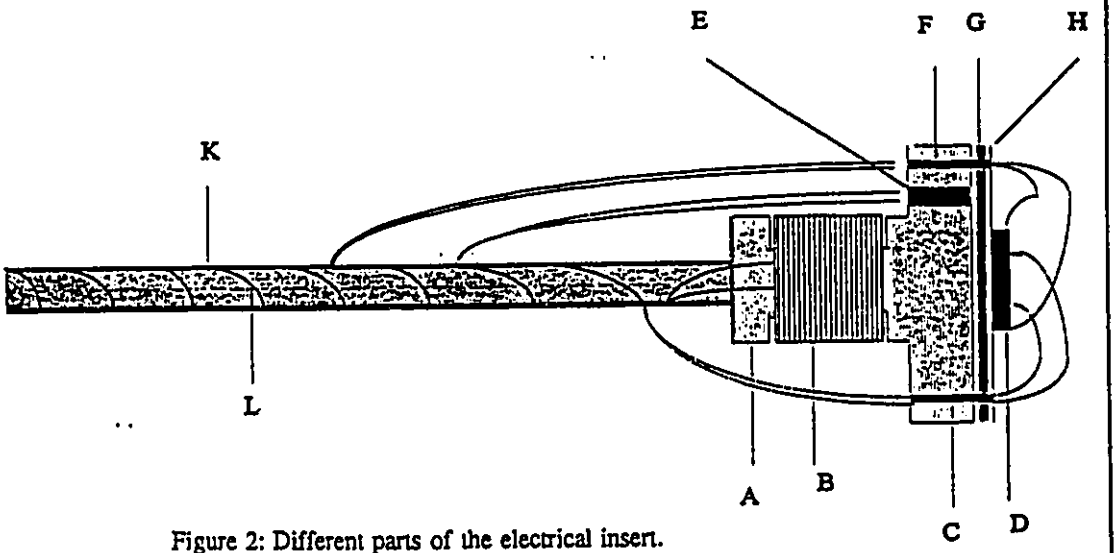

Figure 2: Different parts of the electrical insert.

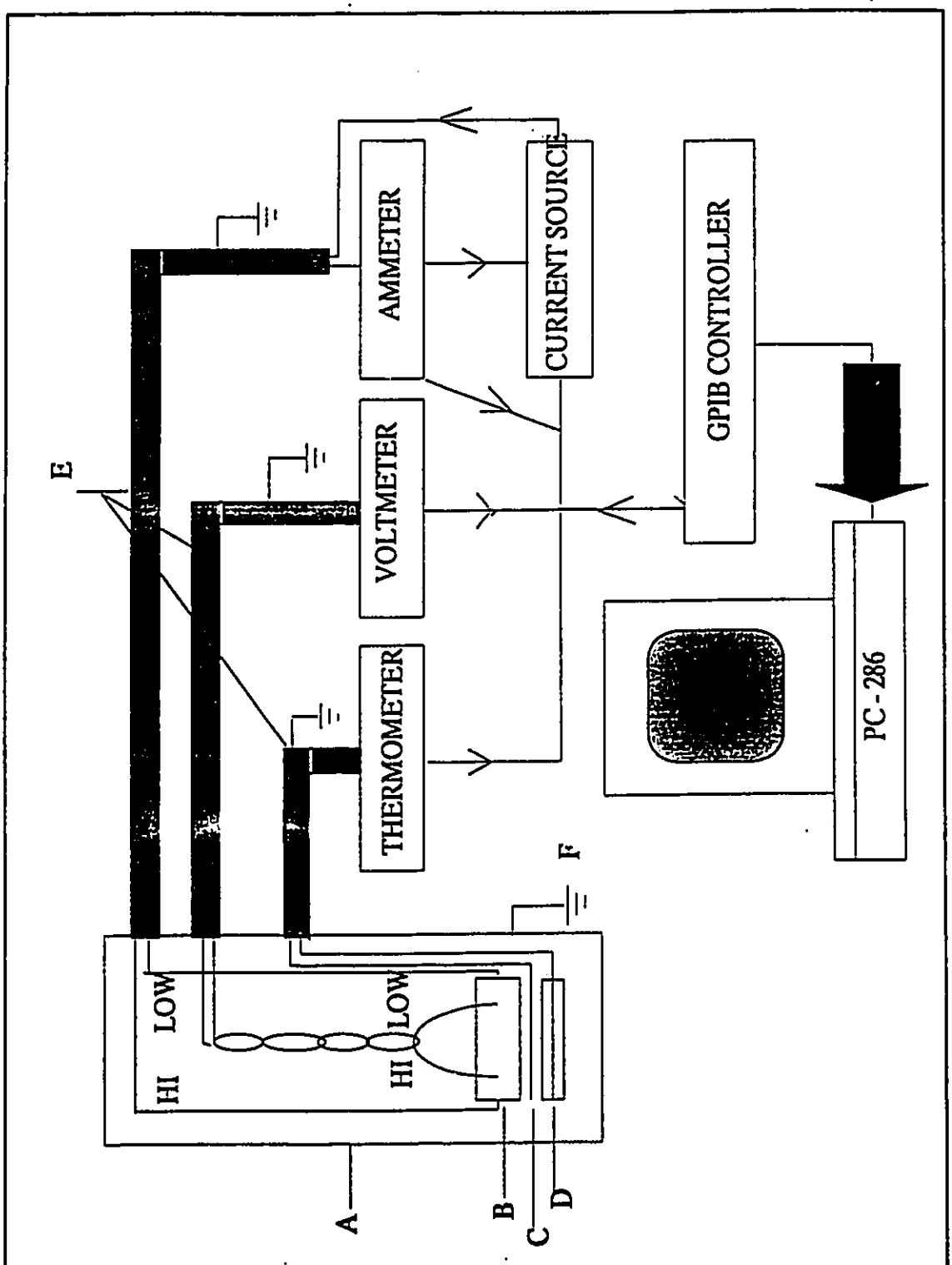

Figure 3: The electronic layout of the system hardware.

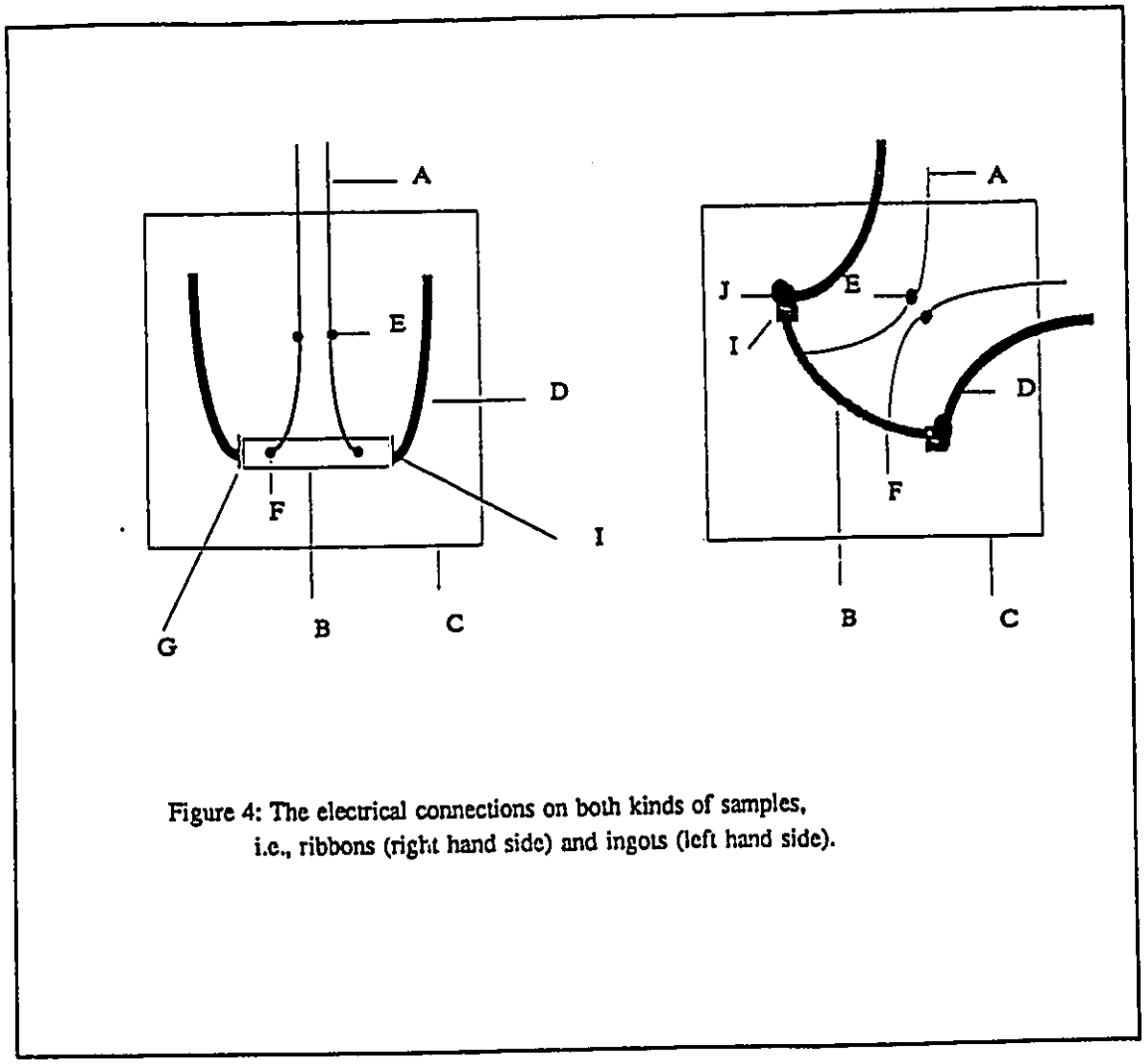

Figure 4: The electrical connections on both kinds of samples, i.e., ribbons (right hand side) and ingots (left hand side).

CHAPTER 4

RESULTS AND DISCUSSION

In this chapter the temperature dependencies of the resistivity of 10 Al-rich i-alloys, all of which contain transition metals, are discussed. Among these QCs, Al-Pd-Mn-B and Al-Cu-Mn-B are ferromagnetic alloys with Curie temperatures higher than the room temperature (Yokoyama et al. 1992). The rest of the samples are either paramagnetic or diamagnetic. An amorphous alloy has also been measured to compare the electron transport behaviour in different phases. All of the studied samples are of ribbon forms, except the i-Al-Cu-Ru stable alloy which is of an ingot form. For other ingot samples the measurement was carried out only in the temperature range 77-300 K. These samples are not discussed here since the large fluctuations in the resistivity data would not allow a correct analysis of the temperature dependence of the resistivity.

All of the studied samples are single-phase and of high structural quality except the $Al_{62}Cu_{25.5}Fe_5Mn_{7.5}$ sample which contains about 40% of the second phases (Stadnik and Zhang 1995). For the studied samples the x-ray diffraction spectra show sharp Bragg reflections with corresponding peak-widths comparable to those found for crystalline alloys (Stadnik and Zhang 1995). The $Al_{62}Cu_{25.5}Fe_5Mn_{7.5}$ sample was also measured after a 60 h etching to investigate the effect of the crystalline impurity on the temperature dependence of the resistivity. Tables and figures are given at the end of the chapter.

Attempts have been made to explain the temperature dependencies in the scope

of the existing theories. Occasionally, the unexpected electron transport behaviour in some alloys could not be explained within the framework of these theories. Comparisons have been made between the extracted parameters and the data from other experimental studies. The temperature dependence of the resistivity predicted by conventional theories has been fitted to the experimental data using a Peakfit algorithm (Peakfit 1990). The corresponding fits are non-linear least-squares fit based on the Marquardt's mathematical procedure of finding the global minimum. A goodness of the fits was judged based on the coefficients of determination (r^2) (Peakfit 1990) which are given by the program. The coefficient of determination is defined as (Peakfit 1990):

$$r^2 = 1.0 - \frac{\sum_{i=1}^{n} w_i (Y_i - y_i)^2}{\sum_{i=1}^{n} w_i (y_i - \bar{y})^2}, \qquad (32)$$

where Y_i is the y value of the curve fit at *i*th data point, y_i is the y value of *i*th data, y is the mean of the y_i and w_i is the weight corresponding to the *i*th point. Therefore, the closeness of the r^2 to unity can determine the goodness of the fit. These determination coefficients are given in the tables along with the fitted parameters.

4.1) CLASSICAL THEORIES

Table (1) lists the samples, the corresponding ρ values at 300 K, the TCRs, and the resistivity ratios. The ferromagnetic alloys are indicated by a star sign. Large errors in the resistivity values are mostly due to the errors in the volume measurement. The errors due to the resistance measurement are negligibly small as compared to the error caused by the volume measurements. It is assumed that the variation in the volume during the measurement is much smaller than the change in the resistance of the sample. Thus, the errors in the normalized resistivity values are much smaller than those of the resistance. The relative error corresponding to the normalized resistivity is about twice as larger as that associated with the resistance (0.1%). Consequently, it is negligible in comparison to the relative error of the resistivity (~20%).

Figure (1) shows the effect of identical etching (60 hours) on three different compositions in the Al-Cu-Fe-Mn i-system. The resistivity values are normalized to the corresponding values at 280 K. It is concluded from this graph that etching greatly affects the resistivity of the $Al_{62}Cu_{25.5}Fe_{10}Mn_{2.5}$ sample. In particular, it causes an increase in the resistivity ratio. This ratio is an indication of the degree of purity in a crystalline sample (Kittel 1986). For the $Al_{62}Cu_{25.5}Fe_{7.5}Mn_5$ sample the slope decreases slightly due to the etching. However, this small change is within the experimental error, and thus can be neglected. The etching effect on $Al_{62}Cu_{25.5}Fe_5Mn_{7.5}$ (already known to contain about 40% of the second phase) is intermediate between those for other two samples.

The resistivity ratio and the TCR were found to be sensitive to the composition

in the Al-Cu-Fe-Mn i-system (table (1)). It is known that a slight change in the composition of an i-alloy leads to a drastic change in the resistivity (Pierce et al. 1993c). In Al-Cu-Fe-Mn i-system one expects the largest resistivity ratio for $Al_{62}Cu_{25.5}Fe_{10}Mn_{2.5}$ since the composition of this alloy is close to the $Al_{62}Cu_{25.5}Fe_{12.5}$ stable i-alloy (Sahnoune et al. 1992, Pierce et al. 1993c). However, this disagrees with the observed resistivity ratios in table (1). This inconsistency may be explained assuming the presence of a small amount (since it is not detected in the x-ray diffraction pattern) of the crystalline phase impurity, which may strongly changes the resistivity ratio.

The resistivity ratio for the non-magnetic alloys ranges from 0.84 for the Al-Fe-Cr sample with the lowest ρ(300K) to 1.8 for the Al-Cu-Ru stable i-alloy with the highest value of ρ(300K). With one exception (Al-Pd-Fe i-alloy), the TCR values of the studied i-alloys are negative for the resistivities higher than 300 $\mu\Omega$cm. The ρ=300 $\mu\Omega$cm corresponds to the high disorder limit where the g factor starts to decrease below unity (p. 2-30). The high resistivity associated with a positive TCR in Al-Pd-Fe i-alloy may be due to the strong Mott s-d scattering. The resistivity in this alloy is almost temperature independent and its resistivity ratio is also close to one; this agrees with the prediction of the Mott model (figure (2-A)).

The temperature dependence of the resistivity of non-magnetic alloys is plotted in a single graph in figure (2-A). The resistivity values are normalized to the values at 273 K. This plot resembles the unified plot for amorphous and quasicrystalline alloys given by Mizutani (figure (13) of chapter 2). The temperature dependence of the resistivity of the Al-Fe-Ce amorphous alloy is very similar to that for i-Al-Pd-Fe. Therefore, a strong

Mott s-d scattering can also be present in the Al-Fe-Ce amorphous alloy. For ferromagnetic Al-Pd-Mn-B and Al-Cu-Mn-B quasicrystalline alloys (figure (2.B)), one may also expects a high rate of s-d scattering. This is due to the presence of the high density of the d bands at the Fermi level in such alloys (Mizutani 1993a). In particular, the Al-Cu-Mn-B i-alloy has a very high resistivity which is associated with a positive TCR (table (1)). The large positive TCR (table (1)) in this alloy indicates that the high resistivity is not caused by a strong scattering of electrons from structural disorder, but that it is due to the high s-d scattering.

A Mooij plot is shown in figure (3) for the non-magnetic alloys. The Al-Cu-Ru alloy is not included in this plot because its resistivity parameters are out of the scale. However, the resistivity and the TCR of this alloy satisfy the Mooij correlation. The values of the TCR were obtained by fitting a quadratic polynomial to the experimental data in the temperature range of 77-300 K. With one exception (i-Al-Pd-Fe), the sign change of the TCR occurs around 150 $\mu\Omega$cm. This agrees with the reported value for the non-simple amorphous alloys (p. 2-15).

The resistivity curves of type (a), (b), and (c) in figure (2-A) show a pronounced $1+aT^2$ ($a>0$) form of the temperature dependence at low temperatures (equation (11b)). However, for the Al-Ge-Cr-Fe (f) alloy a $-T^2$ term is present over a wide temperature range. The $+T^2$ form of the resistivity is an indication of the multiphonon scattering in the resistivity dependence types (a), (b), and (c). Figures (4-7) show the T^2 dependencies of the Al-Cu-Mn-B, Al-Cr-Fe, Al-Ge-Cr-Fe, and Al-Pd-Fe i-alloys for the temperatures much below the corresponding Debye temperatures. The fitted parameters with the

corresponding standard errors, as well as the determination coefficients (r^2), are given in table (2).

For the temperatures around the Debye temperature the experimental resistivity data of the corresponding alloys show a quadratic polynomial temperature dependence predicted by both the Evans and generalized Ziman models (equations 11a,17). The experimental data and the theoretical fits are shown in figures (8-11) for the appropriate temperature ranges . The corresponding fitted parameters are given in table (3). Table (4) lists the coefficients of the Debye temperatures, $S_0(2k_F)$-1 (equation (13)), and the low- and high-temperature coefficients of the Debye-Waller exponents (W(T)) (p. 2-10). One can'tice that the temperature ranges in which the resistivity data were fitted to the Ziman model (table (2)) are consistent with the θ_D values determined in table (4).

The extracted free-electron parameters from the Evans' model (equations (6-13)) are listed in table (5). The wavevector $\mathbf{k}_p$ corresponds to the first peak wavevector in the experimental structure factor. The exponents of the Debye-Waller factors at 0 K (W(0)) are of the same order of magnitude as those reported for $Fe_{80}C_{20-x}B_x$ amorphous alloys (Kaul et al. 1986). The values of β, extracted from the generalized Ziman model (equation (17)), are comparable to the values obtained for the Al-Ni-Co, Al-Si-Cu-Co, and Al-Cu-Co d-QCs (Yung-ping and Dian-lin 1994). The values of β are nearly the same for all of these i-alloys. The α parameters for Al-Cu-Mn-B and Al-Ge-Cr-Fe alloys are higher than those for the others. This may be an indication of an enhanced inelastic scattering in these alloys with respect to the others. For the Al-Ge-Cr-Fe alloy, which is a highly disordered alloy (results from the WL theory), the large value of α may explain

the large negative TCR (table (1)). However, the origin of the high α value in Al-Cu-Mn-Fe i-alloy is unknown.

The positive sign of $S_0(2k_F)$-1 in the Al-Ge-Cr-Fe alloy (table (4)) should correspond to the negative TCR (equation (10)), which is indeed the case (table (1)). The magnitudes of the high- and low-temperatures coefficients of the Debye-Waller exponents are of the same order of magnitude for the alloys listed in table (4). Therefore, the TCR can be quantitatively explained in terms of $S_0(2k_F)$-1 parameters (equation (10)). The magnitude of $S_0(2k_F)$-1 in the i-Al-Pd-Fe and Al-Fe-Ce alloys are nearly the same, which explains the close TCR values corresponding to these alloys (table (1)). In the Ziman model the Debye-Waller factor leads to a negative TCR (p. 2-12). Thus, the low magnitude of $S_0(2k_F)$-1 in the Al-Cu-Mn-B and Al-Cr-Fe alloys indicates the higher TCRs in these alloys than those for the i-Al-Pd-Fe and Al-Fe-Ce alloys; this agrees with table (1). The high-temperature coefficients of the exponents are almost two orders of magnitude higher than the corresponding low-temperature coefficients. This effect causes the resistivity saturation at low temperatures (figures (2-A,2-B)). The change of the TCR at low temperatures in the Al-Cu-Mn-B alloy (figure (2-B)) is more pronounced than that in others alloys (figure (2-A)). This is due to the larger difference between the high- and low-temperature coefficients of the Debye-Waller exponents in Al-Cu-Mn-B alloy as compared to that difference in other alloys (table (4)).

The coefficients of the quadratic terms in both the low- and high-temperature regions (tables (2,3)) for the Al-Cu-Mn-B ferromagnetic alloy are one order of magnitude larger than those in other alloys. This is related to the magnetic resistivity ($\rho_{mag}(T)$),

which is caused by the coherent electron-magnon interaction (Kaul et al. 1986, Rajaram et al. 1984) and varies as T^2. The total resistivity in a magnetic alloy can be regarded as the sum of the structure-induced and the magnetic resistivities (Matthiessen's rule (Kittel 1986)). The incoherent structural-magnon scattering term, which is of the form $T^{3/2}$ (Kaul et al. 1986), is expected to be twice larger than the spin-wave term (T^2 term). The $T^{3/2}$ form of the resistivity was not found in the studied ferromagnetic samples. However, a pronounced T^2 dependence was found in the Al-Pd-Mn-B ferromagnetic alloy over a wide temperature range (figure (12)). This indicates a large contribution from the coherent electron-magnon scattering to the resistivity in this alloy. The high magnetic contribution to the resistivity in ferromagnetic alloys may also be responsible for the major deviations of these alloys from the Mooij correlation (figure (6) of chapter 2). The Al-Pd-Mn-B alloy shows (figure (2-B)) a wide resistivity maximum similar to those seen for the diamagnetic alloys, such as Al-Pd-Mn quasicrystalline alloy (Matsuo et al. 1994). The origin of this maximum is also related to the ferromagnetic property of this alloy, which will be discussed in section (4.2) in relation to the spin-orbit and the spin effects.

The Evans' model overestimates (table (5)) the free-electron values ($W(0),k_F$) for the Al-Ge-Cr-Fe alloy. The temperature dependence of the resistivity in this alloy has a dominant $-T^2$ term, instead of the $+T^2$ term observed in other alloys. Therefore, the temperature dependence of the resistivity in this alloy can be qualitatively described by the $\rho(T) \propto 1-aT^2$ ($a>0$) relation over a wide temperature range (figure (6)). The coefficient of the $-T^2$ term is comparable (table (2)) to the coefficient of the $+T^2$ term in the other alloys. This alloy has also a large and negative TCR comparable to that found for the

high-resistivity Al-Cu-Fe-Mn alloys.

In the Ziman model the $+T^2$ term arises from the multiphonon scattering and is estimated to be twice larger than the $-T^2$ term caused from the elastic scattering (p. 2-6). However, the $-T^2$ cotribution to the resistivity whose magnitude is the same as that of the $+T^2$ contribution in a typical disordered alloy can only be described by the phonon ineffectiveness phenomenon, i.e., a high contribution from the elastic scattering associated with a low mean-free path (p. 2-7). As it will be discussed later, the strong electron-electron scattering in Al-Ge-Cr-Fe is the dominant cause behind the dephasing of the phase coherence (the WL effect), leading to a small mean-free path. The small mean-free path electrons are ineffectively scattered by phonons (Howson and Galagher 1988).

In the Ziman model one expects a negative TCR when $2k_F$ coincides with the value of the first peak wavevector in the structure factor (Mizutani 1993a). The relation $2k_F=k_p$ does not hold (table (5)) for the studied alloys, except for the Al-Cr-Fe and Al-Cu-Mn-B alloys with positive TCRs (table (1)). It is concluded that the $2k_F=k_p$ predicted by the Ziman theory is not valid generally for the transition-metal containing alloys. The fact that the relation $2k_F=k_p$ is fulfilled for the Al-Cu-Mn-B and Al-Cr-Fe may be an indication of a strong FS-BJZ predicted for i-alloys (Poon 1992, Fujiwara and Yokokawa 1991, Laissardière and Fujiwara 1994b).

The Fermi velocities calculated from the k_F values (table (5)) for the Al-Cu-Mn-B and Al-Cr-Fe i-quasicrystalline alloys are of the same order of magnitude ($\sim 2\times10^8$ cm/s). This value is comparable to the free-electron Fermi velocity value commonly used for QCs (Mizutani 1993a). The small Fermi velocities in Al-Pd-Fe i-alloy and Al-Fe-Ce

amorphous alloy may be due to the strong Mott s-d scattering mechanism.

4.2) QUANTUM INTERFERENCE THEORY

The Al-Cu-Ru, Al-Cu-Mn-Fe, Al-Ge-Cr-Fe, and Al-Pd-Mn-B alloys, which are characterized by high-resistivities and are considered to be strong-scattering i-alloys, are studied in the scope of the quantum interference theory. Other i-alloys which were studied by the classical models are also investigated using the WL theory as an appropriate extension to the classical theories. In the WL theory the alloys are compared based on the degree of the structural disorder and the dominant scattering mechanisms. In some cases the free-electron assumptions are made in order to compare the free-electron-like transport properties of the weak- and the strong-scattering alloys. Three main scattering mechanisms are involved in the current data analysis: the elastic, the inelastic, and the spin-orbit scattering. The spin effect is neglected for the present i-alloys since in general $\tau_s >> \tau_{so}, \tau_i$.

4.2.1) POWER LAW OF THE CONDUCTIVITY

Figures (13,14) show the temperature dependencies of the resistivity of the $Al_{62}Cu_{25.5}Fe_{7.5}Mn_5$ and $Al_{62}Cu_{25.5}Fe_{10}Mn_{2.5}$ alloys on a log-log scale. The values of σ_0 were extracted from the polynomial extrapolation of the resistivity data at low temperatures to 0 K. These plots indicate two separate linear regions with the change in the slope around

36 K. It is concluded that the temperature dependence of the conductivity in these alloys can be explained by the relation: $\sigma(T)=\sigma_0+AT^n$. The same behaviour has been observed in many metallic glasses and other QCs (Howson and Gallagher 1988, Tamura et al. 1994b). Similar plots for $Al_{62}Cu_{25.5}Fe_5Mn_{7.5}$ and E-$Al_{62}Cu_{25.5}Fe_5Mn_{7.5}$ alloys (figures (15,16)) show a rather strange behaviour. The temperature dependence of the conductivity at low (10-20 K) and medium (40-90 K) ranges (tables (6,7)) for these alloys can be described by the same relation. However, at high temperature range no power law of conductivity was found. The strange low temperature electron transport behaviour in $Al_{62}Cu_{25.5}Fe_5Mn_{7.5}$ and E-$Al_{62}Cu_{25.5}Fe_5Mn_{7.5}$ alloys may be due to the impurity scattering or the structural defects which cause the broadening of the peaks in the structure factor.

4.2.2) EEI EFFECT, ELECTRON HOPPING BEHAVIOUR AND logT EFFECTS

As it is seen from table (6), the low temperature values of n are close to 0.5 which is predicted by the EEI theory. For the $Al_{62}Cu_{25.5}Fe_{7.5}Mn_5$ alloy this value is lower, and for the E-$Al_{62}Cu_{25.5}Fe_5Mn_{7.5}$ it is larger than 0.5. This may be due to the fact that the values of n are critically affected by the σ_0 values used. The figures (17-20) show the EEI effect on a $\sigma(T)$ vs. $T^{1/2}$ scale for the corresponding Al-Cu-Fe-Mn i-system.

At higher temperature ranges the fits from the log-log plots (figures (13,14)) suggest that the conductivity of $Al_{62}Cu_{25.5}Fe_{7.5}Mn_5$ and $Al_{62}Cu_{25.5}Fe_{10}Mn_{2.5}$ can be described by the relation: $\sigma(T)=\sigma_0+AT^n$ (p. 2-27) with the n values of 1.58 and 1.33, respectively (table (7)). Figure (21) shows this temperature dependence, i.e., $\sigma(T)=\sigma_0+T^{1.33}$ on a

different scale for the $Al_{62}Cu_{25.5}Fe_{10}Mn_{2.5}$ composition. The similar value of n (1.35) has also been reported by Tamura et al. (Tamura et al. 1995) for the Al-Cu-Ru i-alloy. The comparable value (1.34) was also obtained for a group of Ca-Al-Ga high-resistivity metallic glasses by Naugle et al. (Naugle et al. 1986). Tamura et al. have attempted to explain the n values in the scope of the variable range hopping model (p. 2-27). However, for the three dimensional case the expected n value was estimated to be below unity (p. 2-27). Although the high-temperature power law of conductivity may be explained by invoking the band structure effect, the temperature dependence of the carrier density, or the variable range hopping models, I am aware of no theory which explains the corresponding high-temperature n values. However, the fits obtained from the WL theory, over a wide temperature ranges, are the best for these alloys.

The n values obtained for the $Al_{62}Cu_{25.5}Fe_5Mn_{7.5}$ and E-$Al_{62}Cu_{25.5}Fe_5Mn_{7.5}$ alloys in intermediate temperature range (table (7)) are close. This fact indicates that an identical scattering mechanism (or mechanisms) dominates the electron transport behaviour at this temperature range in both alloys. The low-temperature analysis of these two samples shows (figures (22,23)) that the resistivity varies as logT over a wide range of temperature. The values of the logT fit parameters are given in table (8). The values of ß (table (8)) are much higher than those reported for the $Fe_{80}C_{20-x}B_x$ ferromagnetic amorphous alloy. The logT dependence has been frequently related to Kondo (spin-glass-like behaviour), and occasionally to the TLS effects (p. 2-17). However, none of these effects have received enough theoretical foundation (Cochrane and Ström-Olsen 1984). The strong logT effect in $Al_{62}Cu_{25.5}Fe_{2.5}Mn_{7.5}$ and E-$Al_{62}Cu_{25.5}Fe_{2.5}Mn_{7.5}$ alloys may

indicate another mechanism at low temperatures due to the impurity scattering, which in combination with the EEI effect, leads to the strange low-temperature behaviour in these alloys. The fit temperature ranges for the EEI (table (6)) and the logT effects (table (8)) suggest the existence of another mechanism at low temperatures. It is observed (tables (6,8)) that the logT effect in the $Al_{62}Cu_{25.5}Fe_{2.5}Mn_{7.5}$ alloy continues to much higher temperatures, whereas the EEI effect is overwhelmed by other dominant effects (tables (6,8)). The EEI effect was also observed in the Al-Pd-Mn-B ferromagnetic alloy (figure (24)), which confirms the fact that the EEI is not a magnetic dependent effect (Dugdale 1987). In the other quasicrystalline alloys no such pronounced $\sqrt{T}$ dependence was found at low temperatures.

In the Al-Cu-Ru stable i-alloy, which has the highest room temperature resistivity and the negative TCR, the EEI was not found down to 10 K. The similar log-log plot (figure (25)) for this alloy suggests that the temperature dependence of the resistivity over a large temperature range can be best described by the Mott variable range hopping model (p. 2-27) with n=0.9. As will be discussed later, the fit from the WL theory for this alloy predicts a linear temperature dependence for the dephasing rate ($\tau_i \propto T^p$, p=1). In disordered systems the $\tau_i \propto T^{-1}$ can only be ascribed to the long range electron-electron interaction in the strong-scattering regime (Plenet et al. 1992, Altshuler and Aronov 1985). Therefore, the absence of the EEI at low temperatures is the indication of the deviation from the WL theory in this alloy. The deviation from the WL theory may be due to the very high resistivity found in this alloy. The variable range hopping behaviour on the metallic side of the metal-insulator transition in the Al-Cu-Ru alloy indicates the

vicinity of the metal-insulator transition (Altshuler and Aronov 1985, Xiao and Chien 1986). This suggests the occurence of the localized electronic states at the Fermi level rather than of the weakly localized states (Tamura et al. 1995). The density of the localized states at the Fermi level in the neighbourhood of the metal-insulator transition is very high, so that the Anderson localization collapses and the alloy does not follow the WL prediction (Xiao and Chien 1986). The resistivity data of the Al-Cu-Ru alloy could not be fitted with the $\exp(AT^{-1/2})$ or $\exp(AT^{-1/4})$ forms which are expected for an insulator (Xiao and Chien 1986). This shows that the Al-Cu-Ru alloy behaves as a semimetal.

4.2.3) METAL-INSULATOR TRANSITION

In figure (26) the Al-Cu-Fe-Mn system is compared to the Al-Cu-Ru high-resistivity i-alloy on the metal-insulator transition plot suggested by Klein et al. (Klein et al. 1992). The Al-Cu-Ru alloy was found to be the closest i-alloy to the metal-insulator transition line. However, the parameters of this alloy do not lie on the transition line. Other high-quality QCs have also been previously reported not to lie on this line (Akiyama et al. 1993a). The vicinity of the metal-insulator transition line in the Al-Cu-Ru alloy, as well as the electron hopping transport behaviour, can be taken as evidence of the enhanced density of the localized electronic states and the decrease in the carriers density at the Fermi level (p. 2-28).

4.2.4) WL THEORY

The experimental data on i-QCs were fitted with the exact formula of the WL theory derived by Matsuo et al. (equation (24)), which includes the spin-orbit interaction. The extra $T^{1/2}$ term was also added for the expected EEI effect (Sahnoune et al. 1992). For all of the alloys the best fits were obtained in the appropriate temperature ranges. The temperature dependence of the conductivities along with the theoretical lines are shown in figures (27-35). There were six independent parameters in the fit function (see appendix (B)). Because of the large number of variables used, the standard fit-errors were relatively high. The errors were minimized by fixing two parameters and fitting the other four parameters. The calculated scattering parameters from the fitted parameters together with the coefficients of determination are given in table (9). The fits are relatively good for Al-Cu-Fe-Mn_x with x=2.5, 5 and Al-Ge-Cr-Fe alloys over a wide temperature range. Four scattering parameters are obtained directly from the fitted parameters. These scattering parameters are: 1) the electron elastic mean-free path (l_e), 2) the spin-orbit to the inelastic scattering time ratio ($\tau_{so}/4\tau_{io}$), 3) the elastic to the inelastic scattering time ratio (τ_o/τ_{io}), and 4) the electron-electron or electron-phonon inelastic dephasing power (p). The scattering parameters are related to the fitted parameters by the following relations (see also appendix (B)):

$$l_e=e^2(\sqrt{D})/2\pi^2\hbar B,\ \tau_o/\tau_{io}=D/3,\ \tau_o/\tau_{so}=E/3,\ \tau_i=\tau_{io}T^{-C},\ C=p. \qquad (33)$$

4.2.4.1) ELECTRON-ELECTRON AND ELECTRON-PHONON DEPHASING

For the Al-Cu-Fe-Mn_x with x=2.5, 5 alloys the value of ~1.5 found for the dephasing power. This indicates that the electron-electron inelastic scattering is the dominant cause of the dephasing of the quantum interference in these alloys (p. 2-23). This value corresponds to the electron-electron scattering in the strong-scattering regime (Sahnoune et al. 1992). The p~3/2 value has been reported for several Al-Cu-Fe stable i-alloys (Matsuo et al. 1994, Sahnoune et al. 1992). For the $Al_{62}Cu_{25.5}Fe_5Mn_{7.5}$ and E-$Al_{62}Cu_{25.5}Fe_5Mn_{7.5}$ alloys the higher p values 1.7 and 2.1, respectively were obtained. The value of 1.7 in the former alloy can also be due to the electron-electron dephasing in the strong-scattering regime (p close to 1.5). However, in the latter alloy the value of 2.1 is due to the electron-phonon dephasing in the weak-scattering regime (p. 2-23). The 1.7 value also can be due to the electron-electron inelastic dephasing mechanism (p. 2-23). However, the presence of a dominant $T^{1/2}$ term (EEI) observed at low temperatures (figure (20)) strongly suggests the electron-electron interaction.

For the Al-Cr-Fe i-alloy the value of p~2 is likely due to the dominant electron-phonon inelastic scattering process. The quasi-elastic electron-phonon term observed at low temperature for this alloy (figure (5)) confirms this fact. The p~2 value (table (9)) was also found for the Al-Pd-Mn-B alloy. The low temperature dominant EEI effect (figure (24)) in this alloy suggests that the obtained value corresponds to the electron-electron dephasing in the weak-scattering regime (p. 2-23). In the Al-Ge-Cr-Fe alloy the p=1.3 value (table (9)) is due to the electron-electron scattering in dirty limit ($k_F l_e$<1)

(table (10)). The resistivity ratio for this alloy is comparable to theresistivity ratio for the Al-Cu-Fe-Mn system. The EEI effect was not observed for Al-Ge-Cr-Fe alloy; it might have been overwhelmed at low temperatures by the dominant spin-orbit effect causing the resistivity maximum around 30 K (figure (2-A)). The value of 1.2 for Al-Cu-Mn-B is smaller than 3/2 (which correspond to strong electron-electron scattering regime) and does not belong to $2<p<4$ limit corresponding to the electron-phonon scattering. Therefore, it can't be explained in terms of the electron-electron or electron-phonon scattering. However, from figure (4) one can see that the electron-phonon scattering is dominant at low temperatures. One can thus conclude that the parameters of this alloy correspond to the weak-scattering regime.

In the Al-Cu-Ru i-alloy, with the residual conductivity of ~26 $(\Omega cm)^{-1}$ (which is much lower than the Mott's minimum metallic conductivity of 200 $(\Omega cm)^{-1}$) the $p \sim 1$ value can't be explained in the scope of the WL theory. This value suggests a dephasing rate which varies as: $\tau_i^{-1} \propto T$ (p. 2-23). This temperature dependence is caused by the electron-electron interaction at low temperatures (Plenet et al. 1992), whereas the EEI interaction ($T^{1/2}$ temperature dependence of the conductivity) was not found at low temperatures. However, the absence of the EEI effect shows the deviation from the WL theory.

4.2.4.2) ELECTRON MEAN-FREE PATH

The values for the elastic electron mean-free paths (table (9)) indicate that all the studied i-alloys are strongly disordered. These values are close to the interatomic distances

in a typical crystalline metal (Kittel 1986). For the Al-Cu-Fe-Mn$_x$ with x=2.5, 5 and Al-Pd-Mn-B alloys, the l_e values are larger than 3.2 Å reported for an Al-Cu-Fe i-alloy (Sahnoune et al. 1992). However, they are close to the value reported for the Al-Pd-Mn i-alloy (Matsuo et al. 1994). The unphysically small value of 0.67 Å has also been reported for the Al-Cu-Fe stable i-alloy (Matsuo et al. 1993). The higher values of the mean-free path in Al-Cu-Fe-Mn$_x$ with x=2.5, 5 and Al-Pd-Mn-B alloys confirm the fact that the origin of the low conductivity in the strongly disordered alloys is not solely due to the decrease in the electron elastic mean-free path (p. 2-30). This has also been pointed out by Poon (Poon 1992). In the strong-scattering regime the increase of the resistivity is due to the decrease in the *g* factor (and consequently in the decrease of the Fermi velocity, v_F, and the density of charge carriers, *n*) (p. 2-30). The small value of the electron mean-free path in the Al-Ge-Cr-Fe alloy may explain the origin of the phonon ineffectiveness of the inelastic scattering, which occures at the low mean-free path regime.

4.2.4.3) ELECTRON SCATTERING RELAXATION TIMES

Table (10) lists the electron scattering relaxation times obtained directly from the fitted parameters (equation (33)). In the calculation of the scattering times it has been assumed that $v_F = 0.5\times10^8$ cm/s for the Al-Cu-Fe-Mn$_x$ with x=2.5, 5 and Al-Pd-Mn-B alloys, and $v_F = 2\times10^8$ cm/s for the rest of the alloys. The latter value was found previously from the Evans' model in section 4.1. The reason for the use of 0.5×10^8 cm/s (which is smaller than the free-electron value of 10^8 cm/s) for the Al-Cu-Fe-Mn$_x$ with

x=2.5, 5 and Al-Pd-Mn-B alloys is to account for the reduced g factor (equation (30)) in these alloys rather than for the decrease in the electron mean-free path (Mizutani 1993a). In the high-resistivity limit the Fermi velocity of 0.2×10^8 cm/s has been estimated (Mizutani 1993a). A much lower value of $\sim10^7$ cm/s has also been deduced from the WL theory for the Al-Pd-Mn i-alloy (Matsuo et al. 1994).

The values of the diffusion constant (D) (table (10)) for the Al-Cu-Fe-Mn_x with x=2.5, 5 and Al-Pd-Mn-B alloys are close to the values of 1.7 and 2 cm^2/s reported for the i-Al-Cu-Fe alloy (Matsuo et al. 1993). With one exception (the Al-Ge-Cr-Fe i-alloy), the disorder parameter ($k_F l_e$) (table (10)) is larger than unity for all the i-alloys; this justifies the use of the WL theory. The $k_F l_e$ value of 0.73 in the Al-Ge-Cr- Fe alloy indicates the existence of a high structural disorder. The high value of disorder parameter in this alloy also explains the value of ~1.3 found for the electron-electron dephasing power (table (9)).

The elastic scattering times (table (10)) are much lower than those found in a typical crystalline alloy (Kittel 1986) and are comparable to the corresponding values in metallic glasses (Dugdale 1987). This confirms the fact that the i-QCs are strong elastic scatterers. This is consistent with the Mooij correlation (p. 2-18) which predicts a negative TCR for the strong elastic scattering alloys. The elastic scattering times are also of the same order of magnitude as the values reported for the Al-Cu-Mg (Poon 1992) and Al-Cu-Fe (Matsuo et al. 1993) i-alloys. The values of the spin-orbit and inelastic scattering times vary over a wider range, but are typically of the same order as those determined by Matsuo et al. (Matsuo et al. 1993) for the Al-Fe-Cu QCs.

According to equation (27), the electron-electron dephasing relaxation time (Altshuler and Aronov 1985) can be estimated by using the disorder parameters from table (10). If we assume the Fermi energy of 1 eV for i-QCs (Sahnoune et al. 1992), then the values of the dephasing relaxation times are respectively 1.39×10^{-10} s and 0.2×10^{-10} s for the Al-Cu-Fe-Mn_x with x=2.5,5 and Al-Ge-Cr-Fe alloys. These electron-electron scattering times are very close to the corresponding inelastic scattering times. This shows that the dephasing of the quantum interference in these alloys is mostly due to the electron-electron scattering.

The inelastic scattering time in the Al-Cr-Fe alloy is much larger than that in others alloys (table (10)). Consequently, a lower contribution to the negative TCR, which is caused by the dephasing of the phase coherence by the inelastic scattering, is expected for this alloy. This agrees with the large positive TCR found for this alloy (table (1)). In the Al-Ge-Cr-Fe alloy a resistivity maximum occurs around 30 K (figures (2-A)). This resistivity maximum is caused by the high spin-orbit scattering rate ($1/\tau_{so}$) with respect to other alloys (table (10)) which contributes to the antilocalization effect (p. 2-25). The spin-orbit effect in the Al-Cu-Fe-Mn_x with x=5 alloy leads to the resistivity saturation at low temperatures (figure (2-A)). Further investigations based on the magnetoresistivity measurements are needed in order to elucidate the role of the spin-orbit effect in these alloys. The values of τ_{so}^{-1} in the Al-Cu-Fe-Mn_x with x=5 and Al-Ge-Cr-Fe alloys are an order of magnitude larger than the τ_{so}^{-1} value reported for the Al-Pd-Mn i-alloy (Matsuo et al. 1994); this indicates the presence of a strong spin-orbit effect.

4.2.4.4) SPIN SCATTERING IN THE FERROMAGNETIC ALLOYS

The resistivity maximum observed in the intermediate temperature range in the Al-Pd-Mn-B alloy suggests the presence of the strong spin-orbit scattering at low temperatures. The spin-orbit scattering causes the antilocalization at low temperatures and the change of the sign of the TCR (figure (1-B)). However, the high inelastic scattering found from fitting the equation (25) to the experimental data of the Al-Pd-Mn-B and Al-Cu-Mn-B alloys (table (10)) would not allow the spin-orbit effect to act. Therefore, the values of the inelastic and the spin-orbit scattering times are not consistent with the resistivity maximum in the Al-Pd-Mn-B alloy, although they are close to the corresponding values reported for the Al-Pd-Mn i-alloy (Matsuo et al. 1994). The origin of the enhanced values of the inelastic scattering rates (table (10)) in these alloys is neglecting the spin-magnon interaction effect. It was shown in section 4.1 that the spin-magnon scattering is important to account for the electron transport properties of these ferromagnetic alloys.

According to the formula given by Matsuo et al. (Matsuo et al. 1994), which includes the spin effect, the modified values of the parameters in equation (25) are:

$$t=(1/\tau_{io}+6/\tau_s)/4(1/\tau_{so}-1/\tau_s),\ t_1=3\tau_o(1/\tau_{so}-1/\tau_s),\ t_2=3\tau_o(1/\tau_{io}+6/\tau_s). \qquad (34)$$

This equation includes the new parameter τ_s which is the spin relaxation time. The scattering parameters in equation (25) are changed from $1/\tau_{io}$ to $(1/\tau_{io}+6/\tau_s)$, and from

$1/\tau_{so}$ to $(1/\tau_{so}-1/\tau_s)$ in equation (34). The comparison between equations (34) and (25) shows that neglecting the spin effect will underestimate the spin-orbit and overestimate the inelastic scattering rates. This comparison also shows that ignoring the spin effect modifies the inelastic scattering rate more than the spin-orbit scattering rate.

By comparing the TCR values of the Al-Pd-Mn-B and Al-Cu-Fe-Mn alloys in table (1) it can be concluded that the inelastic scattering time in the former alloy should be relatively larger than that in the latter alloy. Therefore, one expects the inelastic scattering time of about 10^{-9} s for the Al-Pd-Mn-B alloy which is one order of magnitude larger than that for the Al-Cu-Mn-Fe_x with x=2.5,5 alloys. Assigning a value of 1.3×10^{-11} s for the spin scattering time for the Al-Pd-Mn-B alloy the values of 8.4×10^{-10} s and 0.84×10^{-13} s are obtained from equation (34) for the inelastic scattering and the spin-orbit scattering times, respectively. Therefore, the ratio of τ_{so}/τ_{io} obtained for the Al-Pd-Mn-B alloy is much lower than the corresponding values for other alloys (table (9)) and explains the presence of the strong spin-orbit scattering effect at low temperatures. By assuming the same τ_{so} for the Al-Cu-Mn-B alloy, a similar analysis gives 8.4×10^{-10} s and 31×10^{-13} s for the inelastic and the spin-orbit scattering times, respectively.

The fit with the modified formula gave 9.1×10^{9} s^{-1} for $1/\tau_s$ in the Al-Pd-Mn i-alloy (Matsuo et al. 1994) which exhibits the spin scattering effect. The corresponding spin scattering rate in the Al-Pd-Mn-B alloy is one order of magnitude larger than that obtained for the i-Al-Pd-Mn i-alloy (Matsuo et al. 1994). It can be concluded that the spin effect in the Al-Pd-Mn-B ferromagnetic alloy is larger than that reported for the Al-Pd-Mn i-alloy.

It should be noted that the modification of the variables from equation (25) to equation (34) would not change the l_e values. The presence of the strong spin-orbit scattering in the Al-Pd-Mn-B alloy may be due to the existence of the Pd element which exhibits a strong spin-orbit scattering effect (Kobayashi and Komori 1985). The question to be answered is that: how the spin-orbit effect can dominate in the presence of a high internal magnetic field which destroys the antilocalization effect.

4.2.5) SCALING THEORY

According to the scaling theory, a correlation gap opens in either side of the metal-insulator-transition (Cochrane and Ström-Olsen 1984, Altshuler and Aronov 1985, Xiao and Chien 1986). This gap is characterized by a reduction in the single-electron DOS which is related to the temperature dependence of the conductivity via the scaling theory (Xiao and Chien 1986). The single electron density and the conductivity are scaled by the following relations (Cochrane and Ström-Olsen 1984, Altshuler and Aronov 1985, Xiao and Chien 1986):

$$N(E) = N(0)(1+ \sqrt{E/\Delta})) \quad \text{and} \quad \sigma = \sigma_0(1+ C\sqrt{T}) \ , \tag{35}$$

where N(E) is the single-electron DOS, E is the electron energy, Δ is the correlation gap, and $C=\sqrt{(k_B/\Delta)}$. The second relation in equation (34) describes the low temperature EEI on the metallic side of the metal-insulator transition. The values of the gap were estimated

from the $T^{1/2}$ dependence of the conductivity data at low temperatures for the Al-Cu-Fe-Mn system. The fit parameters and the values of the correlation gap are given in table (11). The values of the gap are comparable to those reported for amorphous alloys (Cochrane and Ström-Olsen 1984). The highest value is observed for the Al-Cu-Fe-Mn_x alloy with x=5, which is the closest composition to the metal-insulator transition line. However, these values decrease quickly with decreasing the residual conductivity (table (11)) and resistivity ratio (table (1)) in the Al-Cu-Fe-Mn i-system (table (1)). Figure (36) shows the correlation plot for the Al-Cu-Fe-Mn system. As can be noticed from the figure the correlation of the form $\Delta \propto \rho_0^{-2} = \sigma_0^2$, which has been reported for amorphous alloys (Cochrane and Ström-Olsen 1984), is not observed in this system. This correlation suggests an increase in the gap with increasing the residual conductivity. Consequently, a smooth vanishing of the gap in the vicinity of the metal-insulator transition is expected for amorphous alloys (Xiao and Chien 1986, Cochrane and Ström-Olsen 1984). For the Al-Cu-Fe-Mn i-alloys, the opposite correlation is observed (figure (36)). The strong composition dependence of the gap value can be noted for the Al-Cu-Fe-Mn system (table (11)). This may be related to the possible composition dependence of the pseudogap at the Fermi level which is believed to be related to the stability of QCs (Poon 1992).

For the high-resistivity Al-Ru-Cu alloy, which is the closest i-alloy to the metal-insulator transition line, no gap was found. The absence of the gap is an indication of the presence of the enhanced localized electronic states at the Fermi level (Xiao and Chien 1986). The variable range hopping behaviour found in this alloy, similar to the insulating-like Al-Pd-Re i-QCs (Pierce et al. 1994), also indicates the presence of the strongly

localized states at the Fermi level (Tamura et al. 1995).

SAMPLE COMPOSITION	ρ(300) (μΩcm)	TCR=(1/ρ(300))dρ/dT ± 0.1 % (K^{-1})	ρ(4.2)/ρ(300) ± 0.1 %	PHASE
$Al_{65}Cu_{20}Ru_{15}$	35000 ± 7000	-37×10^{-4}	1.8	i-alloy
$Al_{62}Cu_{25.5}Fe_{10}Mn_{2.5}$	1529 ± 350	-10×10^{-4}	1.29	i-alloy
$Al_{62}Cu_{25.5}Fe_{7.5}Mn_{5}$	1834 ± 367	-14×10^{-4}	1.36	i-alloy
$Al_{62}Cu_{25.5}Fe_{5}Mn_{7.5}$	501.5 ± 100	-1.0×10^{-4}	1.12	i-alloy
E-$Al_{62}Cu_{25.5}Fe_{5}Mn_{7.5}$	1325 ± 265	-2.0×10^{-4}	1.18	i-alloy
$Al_{60}Ge_{20}Cr_{19.9}Fe_{0.1}$	343 ± 69	-6.1×10^{-4}	1.16	i-alloy
$Al_{64}Pd_{15}Mn_{15}B_{6}$ *	4262 ± 852	-3.9×10^{-4}	1.04	i-alloy
$Al_{65}Cu_{10}Mn_{20}B_{5}$ *	1550 ± 310	28×10^{-4}	0.70	i-alloy
$Al_{86}Cr_{8}Fe_{6}$	90 ± 18	8.3×10^{-4}	0.84	i-alloy
$Al_{70.5}Pd_{24.94}Fe_{0.06}$	124 ± 25	4.8×10^{-4}	0.95	d-alloy
$Al_{70}Pd_{20}Fe_{10}$	1265 ± 253	2.64×10^{-4}	0.97	i-alloy
$Al_{87}Fe_{6.7}Ce_{6.3}$	138 ± 28	2.61×10^{-4}	0.95	amorphous

TABLE (1): List of the studied samples, the corresponding ρ values at 300 K, the TCRs, and the resisistivity ratios. In the fifth column, i- refers to the icosahedral phase, and d- refers to the decagonal phase. E- in the first column refers to the etched sample and the star sign refers to the ferromagnetic alloys.

SAMPLE COMPOSITION	α_2 (K^{-2}) ± 0.1%	α_0 ± 0.1%	TEMPERATURE RANGE (K)	r^2
$Al_{65}Cu_{10}Mn_{20}B_5$	1.60×10^{-5}	0.70	10 - 47	0.9997
$Al_{86}Cr_8Fe_6$	0.39×10^{-5}	0.83	31.6 - 95	0.9991
$Al_{60}Ge_{20}Cr_{19.9}Fe_{0.1}$	-0.31×10^{-5}	1.19	54.7 - 122.5	0.9993
$Al_{87}Fe_{6.7}Ce_{6.3}$	0.49×10^{-5}	0.95	12 - 24.5	0.9669
$Al_{70}Pd_{20}Fe_{10}$	0.27×10^{-5}	0.97	24.5 - 55	0.9988

TABLE (2): The coefficients obtained from the Ziman T^2 law ($T<\theta_D$), i.e., $\rho(T)/\rho(300)=\alpha_0+\alpha_2T^2$ (equation (11b)). The coefficients of determination (r^2) are given in the table. The data were fitted for the indicated temperature range.

SAMPLE COMPOSITION	α_0' ± 0.1%	α_1' (K^{-1}) ± 0.1%	α_2' (K^{-2}) ± 0.1%	T (RANGE) (K)	r^2
$Al_{65}Cu_{10}Mn_{20}B_5$	0.59	3.2×10^{-3}	-65×10^{-7}	60 - 200	0.9997
$Al_{86}Cr_8Fe_6$	0.79	0.87×10^{-3}	-5.1×10^{-7}	100 - 300	0.9999
$Al_{60}Ge_{20}Cr_{19.9}Fe_{0.1}$	1.23	-0.67×10^{-3}	-3.0×10^{-7}	110 - 280	0.9999
$Al_{87}Fe_{6.7}Ce_{6.3}$	0.95	0.26×10^{-3}	-3.5×10^{-7}	100 - 260	0.9994
$Al_{70}Pd_{20}Fe_{10}$	0.96	0.28×10^{-3}	-5.5×10^{-7}	90 - 230	0.9994

TABLE (3): The coefficients obtained from the generalized Ziman temperature dependence ($T\approx\theta_D$), i.e., $\rho(T)/\rho(300)=\alpha_0'+\alpha_1'T+\alpha_2'T^2$ (equation (11a)). The data were fitted for the indicated temperature range.

SAMPLE COMPOSITION	θ_D (K)	$S_0(2k_F)$-1	$W(0)/\theta_D^2$ (K^{-2}) (10^{-7})	$W(0)/\theta_D$ (K^{-1}) (10^{-5})
$Al_{65}Cu_{10}Mn_{20}B_5$	233 ± 1	-0.900 ± 0.004	4.2 ± 0.1	9.90 ± 0.08
$Al_{86}Cr_8Fe_6$	324 ± 3	-0.700 ± 0.007	1.6 ± 0.04	5.28 ± 0.07
$Al_{60}Ge_{20}Cr_{19.9}Fe_{0.1}$	391 ± 7	1.928 ± 0.003	-	-
$Al_{87}Fe_{6.7}Ce_{6.3}$	81 ± 2	-0.368 ± 0.002	7.5 ± 0.2	6.00 ± 0.14
$Al_{70}Pd_{20}Fe_{10}$	140 ± 2	-0.321 ± 0.001	5.5 ± 0.1	7.80 ± 0.11

TABLE (4): The Debye temperatures were deduced from low- and high-temperature fit parameters in tables (2,3) by using equation (12). The the low-temperature coefficients of the Debye-Waller exponents (W(T)) (fourth column) and corresponding high-temperature values (fifth column) are also given.

SAMPLE COMPOSITION	α (10^{-3}) ($\mu\Omega$cm/K)	$\beta \pm 1\%$ (10^{-4}) (K^{-1})	W(0)	$2k_F$ ($Å^{-1}$)	k_p ($Å^{-1}$)	υ_F (10^8) (cm/s)
$Al_{65}Cu_{10}Mn_{20}B_5$	3.7 ± 0.7	7.9	0.02298 ± 0.00006	3.227 ± 0.013	3.020 ± 0.013	1.868 ± 0.007
$Al_{86}Cr_8Fe_6$	1.2 ± 0.2	4.2	0.01715 ± 0.00007	3.0646 ± 0.021	3.026 ± 0.013	1.774 ± 0.012
$Al_{60}Ge_{20}Cr_{19.9}Fe_{0.1}$	3.6 ± 0.7	8.4	0.0409 ± 0.0004	6.007 ± 0.084	3.023 ± 0.013	3.477 ± 0.049
$Al_{87}Fe_{6.7}Ce_{6.3}$	0.73 ± 0.15	4.9	0.00496 ± 0.00002	1.0289 ± 0.012	2.616 ± 0.020	0.595 ± 0.007
$Al_{70}Pd_{20}Fe_{10}$	0.87 ± 0.17	6.2	0.01089 ± 0.00005	1.9545 ± 0.018	3.078 ± 0.010	1.131 ± 0.010

TABLE (5): The free electron parameters obtained from the Evans' ($W(0),k_F$) (equations (6-13)) and the generalized Ziman model (α,β) (equation (17)). W(0) is the 0 K Debye-Waller factor. k_p values correspond to the first peak wavevectors in the experimental structure factor and v_F is the velocity of the electrons at the Fermi level.

SAMPLE	n	T (RANGE) (K)	r^2
$Al_{62}Cu_{25.5}Fe_{10}Mn_{2.5}$	0.62 ± 0.01	10 - 25	0.9888
$Al_{62}Cu_{25.5}Fe_{7.5}Mn_5$	0.32 ± 0.01	10 - 25	0.9399
$Al_{62}Cu_{25.5}Fe_5Mn_{7.5}$	0.61 ± 0.01	10 - 20	0.9997
E-$Al_{62}Cu_{25.5}Fe_5Mn_{7.5}$	0.83 ± 0.01	10 - 16	0.996

TABLE (6): The low-temperature fit parameteres for the power law of conductivity, i.e., $\sigma=\sigma_0+AT^n$. The fits were obtained from the log $[(\sigma-\sigma_0)/\sigma_0]$ vs. log T graphs (figures (13-16)).

SAMPLE	n	T (RANGE) (K)	r^2
$Al_{62}Cu_{25.5}Fe_{10}Mn_{2.5}$	1.33 ± 0.01	63 - 281	0.9998
$Al_{62}Cu_{25.5}Fe_{7.5}Mn_5$	1.58 ± 0.01	63 - 141	0.9998
$Al_{62}Cu_{25.5}Fe_5Mn_{7.5}$	0.36 ± 0.01	40 - 89	0.9989
E-$Al_{62}Cu_{25.5}Fe_5Mn_{7.5}$	0.34 ± 0.01	50 - 80	0.9959

TABLE (7): The high-temperature fit parameteres for the power law of conductivity, i.e., $\sigma=\sigma_0+AT^n$. The fits were obtained from the log $[(\sigma-\sigma_0)/\sigma_0]$ vs. log(T) graphs (figures (13-16)).

SAMPLE	β ($(logK)^{-1}$)	β_0	T (RANGE) (K)	r^2
$Al_{62}Cu_{25.5}Fe_5Mn_{7.5}$	-0.04116 ± 0.00002	1.140 ± 0.001	10 - 63	0.9997
E-$Al_{62}Cu_{25.5}Fe_5Mn_{7.5}$	-0.01728 ± 0.00005	0.700 ± 0.001	10 - 25	0.9987

TABLE (8): The low-temperature fit parameteres obtained from the fitting of the resistivity data to: $\rho(T)/\rho(300)=\beta_0+\beta\log T$. The fits were obtained from the $\rho(T)$ vs. log(T) graphs (figures (22,23)).

SAMPLE	l_ϕ (Å)	$\tau_{so}/4\tau_{io}$ (10^{-4})	τ/τ_{io} (10^{-6})	p	T-RANGE (K)	r^2
$Al_{62}Cu_{25.5}Fe_{10}Mn_{2.5}$	10.7 ± 0.3	3.4 ± 0.2	7.8 ± 0.2	1.50 ± 0.007	10 - 200	0.99997
$Al_{62}Cu_{25.5}Fe_{7.5}Mn_5$	10.9 ± 0.3	2.6 ± 0.1	7.4 ± 0.1	1.57 ± 0.005	10 - 200	0.99998
$Al_{62}Cu_{25.5}Fe_5Mn_{7.5}$	2.0 ± 0.1	18.3 ± 0.2	1.50 ± 0.01	1.71 ± 0.004	10 - 95	0.99991
E-$Al_{62}Cu_{25.5}Fe_5Mn_{7.5}$	4.4 ± 0.1	0.054 ± 0.001	0.170 ± 0.003	2.08 ± 0.004	10 - 90	0.99959
$Al_{86}Cr_8Fe_6$	3.7 ± 0.1	1590 ± 97	87 ± 5	1.94 ± 0.01	10 - 80	0.99903
$Al_{64}Pd_{15}Mn_{15}B_6$	11.3 ± 0.2	0.021 ± 0.001	0.050 ± 0.003	2.29 ± 0.003	10 - 85	0.99957
$Al_{65}Cu_{10}Mn_{20}B_5$	4.2 ± 0.3	5960 ± 495	470 ± 9	1.22 ± 0.004	10 - 47	0.99985
$Al_{60}Ge_{20}Cr_{19.9}Fe_{0.1}$	1.3 ± 0.1	69 ± 3.5	16.9 ± 4	1.26 ± 0.004	10 - 250	0.99997
$Al_{65}Cu_{20}Ru_{15}$	2.7 ± 0.09	0.40 ± 0.01	1.30 ± 0.02	0.96 ± 0.003	10 - 125	0.99990

TABLE (9): The fit parameters obtained from the WL theory including the EEI and the spin-orbit effects (equations (24,25)).

SAMPLE	D (cm^2/s)	τ_0 (s) (10^{-16})	τ_{in} (s) (10^{-13})	τ_{in} (s) (10^{-10})	$(k_F l_e)^{-1}$
$Al_{62}Cu_{25.5}Fe_{10}Mn_{2.5}$	1.8 ± 0.06	5.5 ± 0.1	1.0 ± 0.1	0.7 ± 0.1	0.64 ± 0.02
$Al_{62}Cu_{25.5}Fe_{7.5}Mn_5$	1.8 ± 0.1	5.5 ± 0.1	0.75 ± 0.05	0.75 ± 0.05	0.64 ± 0.02
$Al_{62}Cu_{25.5}Fe_5Mn_{7.5}$	1.34 ± 0.004	4.0 ± 0.01	2.0 ± 0.09	0.0020 ± 0.0001	0.86 ± 0.01
E-$Al_{62}Cu_{25.5}Fe_5Mn_{7.5}$	2.94 ± 0.02	8.8 ± 0.04	1.1 ± 0.1	2.6 ± 0.06	0.390 ± 0.002
$Al_{86}Cr_8Fe_6$	2.46 ± 0.02	7.4 ± 0.1	54 ± 0.6	52 ± 4	0.47 ± 0.03
$Al_{64}Pd_{15}Mn_{15}B_6$	1.9 ± 0.03	5.6 ± 0.1	0.85 ± 0.02	0.021 ± 0.001	0.6 ± 0.1
$Al_{65}Cu_{10}Mn_{20}B_5$	2.8 ± 0.2	8.4 ± 0.6	42 ± 6	0.020 ± 0.002	0.41 ± 0.03
$Al_{60}Ge_{20}Cr_{19.9}Fe_{0.1}$	0.84 ± 0.4	2.54 ± 0.04	0.40 ± 0.02	0.15 ± 0.01	1.37 ± 0.03

TABLE (10): List of the scattering parameters, assuming a Fermi velocity of 0.5×10^8 cm/s for Al-Pd-Mn-B, Al-Cu-Fe-Mn_x with x=2.5, 5 and of 2×10^8 cm/s for the rest of alloys. The parameteres have been obtained from the values in table (9). The last column lists the values of the reciprocals of disorder parameters. In the calculation of these parameters the free electron relations: $l_e=v_F\tau_0$, $D=v_F l_e/3$ (Poon 1992) and equation (32) were used.

SAMPLE COMPOSITION	C ($K^{-1/2}$)	Δ (eV)	log Δ (log(eV))	log σ_0 (log(Ωcm)$^{-1}$)	r^2
$Al_{62}Cu_{25.5}Fe_{10}Mn_{2.5}$	1.82 ± 0.01	6.5 ± 0.1	0.8 ± 0.01	2.7 ± 0.2	0.99
$Al_{62}Cu_{25.5}Fe_{7.5}Mn_5$	0.71 ± 0.02	28 ± 2	1.4 ± 0.1	2.6 ± 0.2	0.94
E-$Al_{62}Cu_{25.5}Fe_5Mn_{7.5}$	6.70 ± 0.03	2.3 ± 0.02	0.4 ± 0.01	3.0 ± 0.2	0.99
$Al_{62}Cu_{25.5}Fe_5Mn_{7.5}$	14.93 ± 0.05	1.2 ± 0.01	0.1 ± 0.01	3.3 ± 0.2	0.99

Table (11): The values of the correlation gap (Δ) for Al-Cu-Fe-Mn i-alloys. The values were obtained from the fit of the low-temperature conductivity data to the function $\sigma=\sigma_0(1+C\sqrt{T})$, $C=\sqrt{(k_B/\Delta)}$, where k_B is the Boltzmann constant.

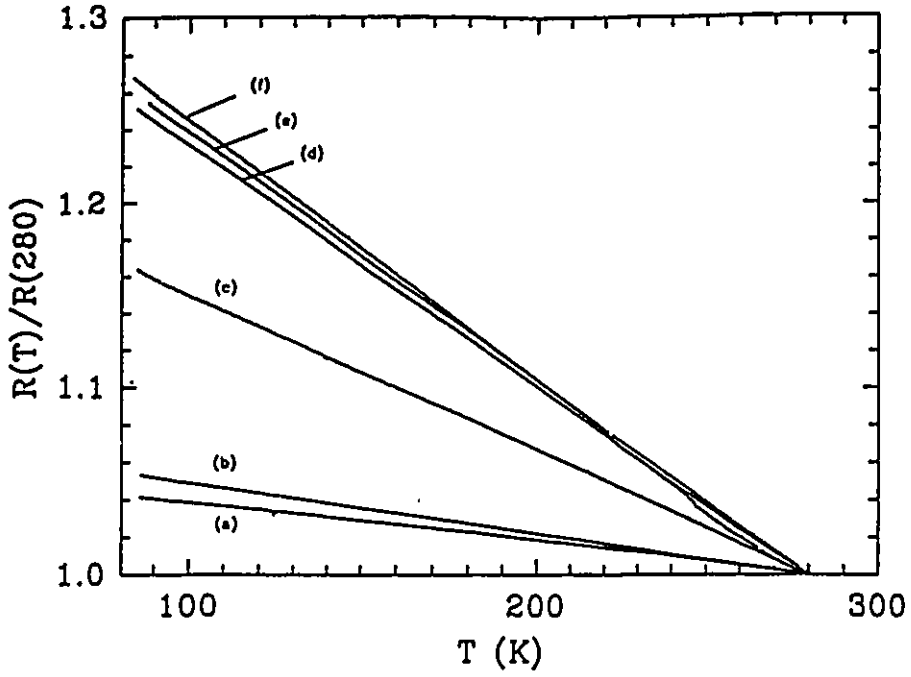

FIG. (1): Etching effect on Al-Cu-Fe-Mn quasicrystalline system. (a) $Al_{62}Cu_{25.5}Fe_3Mn_{7.5}$, (b) $Al_{62}Cu_{25.5}Fe_3Mn_{7.5}$ (etched), (c) $Al_{62}Cu_{25.5}Fe_{10}Mn_{2.5}$, (d) $Al_{62}Cu_{25.5}Fe_{7.5}Mn_5$ (etched), (e) $Al_{62}Cu_{25.5}Fe_{7.5}Mn_5$, (f) $Al_{62}Cu_{25.5}Fe_{10}Mn_{2.5}$ (etched).

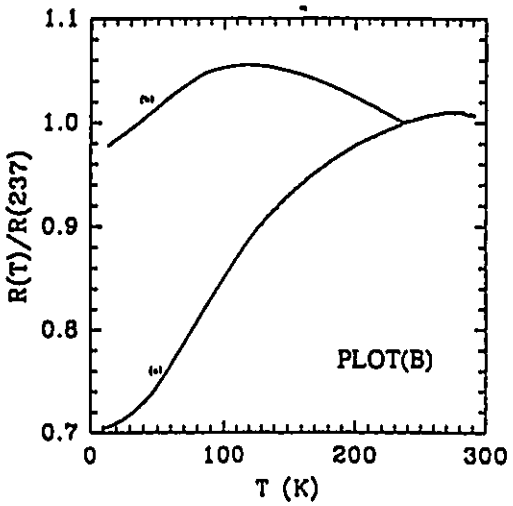

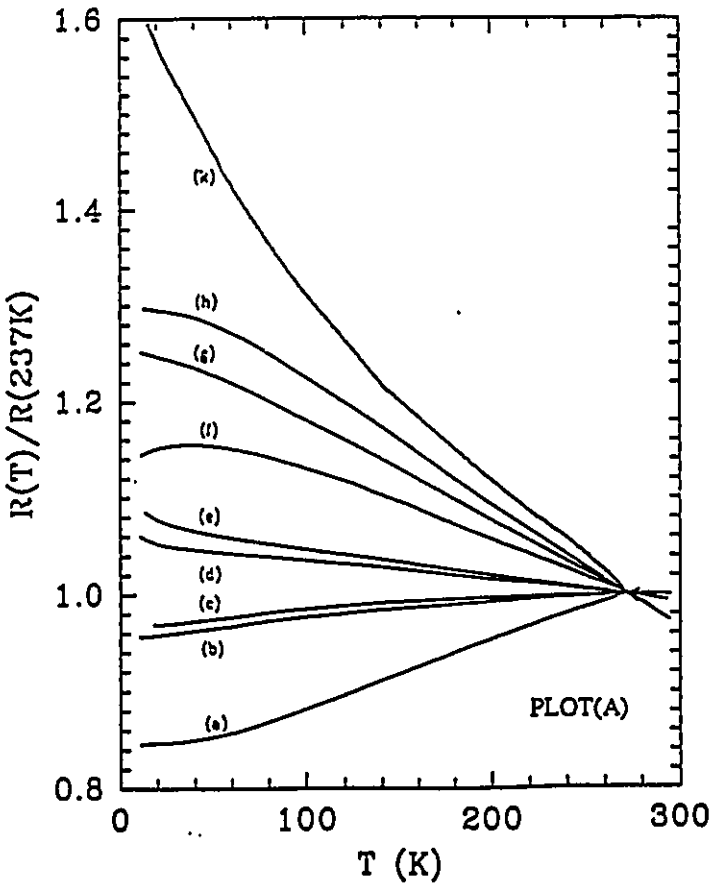

FIG. (2-A): The temperature dependence of the normalized resistivities for: (a) Al-Cr-Fe, (b) Al-Fe-Ce, (c) Al-Pd-Fe (icosahedral) (d) $Al_{62}Cu_{25.5}Fe_3Mn_{7.5}$, (e) $Al_{62}Cu_{25.5}Fe_3Mn_{7.5}$ (etched), (f) Al-Ge-Cr-Fe, (g) $Al_{62}Cu_{25.5}Fe_{10}Mn_{2.5}$, (h) $Al_{62}Cu_{25.5}Fe_{7.5}Mn_5$, and (k) Al-Cu-Ru alloys.
FIG. (2-B): The temperature dependence of the normalized resistivities for the ferromagnetic (a) Al-Cu-Mn-B and (b) Al-Pd-Mn-B alloys.

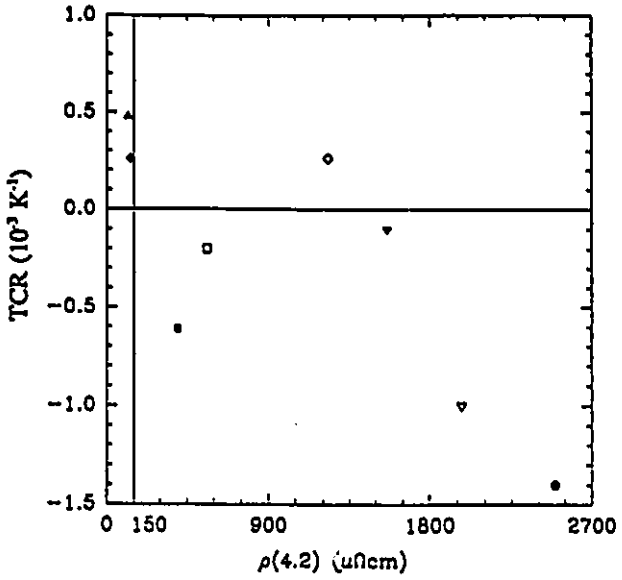

FIG. (3): Mooij correlation for: (◆) Al-Fe-Ce, (◇) i-Al-Pd-Fe, (▲) d-Al-Pd-Fe, (□) $Al_{62}Cu_{25.5}Fe_5Mn_{7.5}$, (▼) $Al_{62}Cu_{25.5}Fe_5Mn_{7.5}$ (etched), (■) Al-Ge-Cr-Fe, (▽) $Al_{62}Cu_{25.5}Fe_{10}Mn_{2.5}$, and (●) $Al_{62}Cu_{25.5}Fe_{7.5}Mn_5$ alloys.

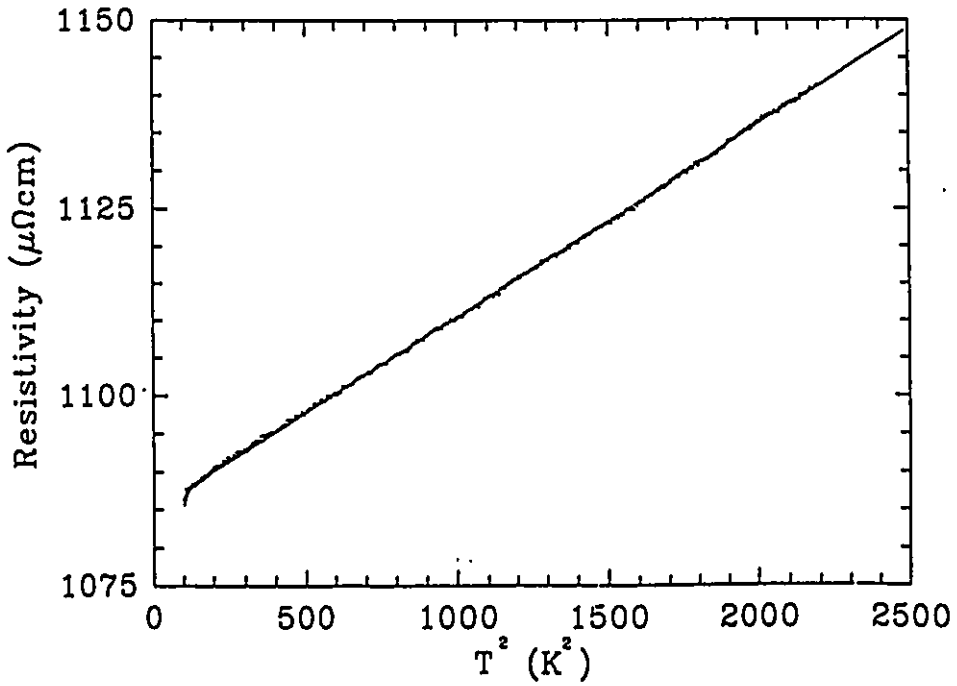

FIG. (4) Low-temperature Ziman T^2 law for Al-Cu-Mn-B i-alloy. The linear fit is shown by the solid line.

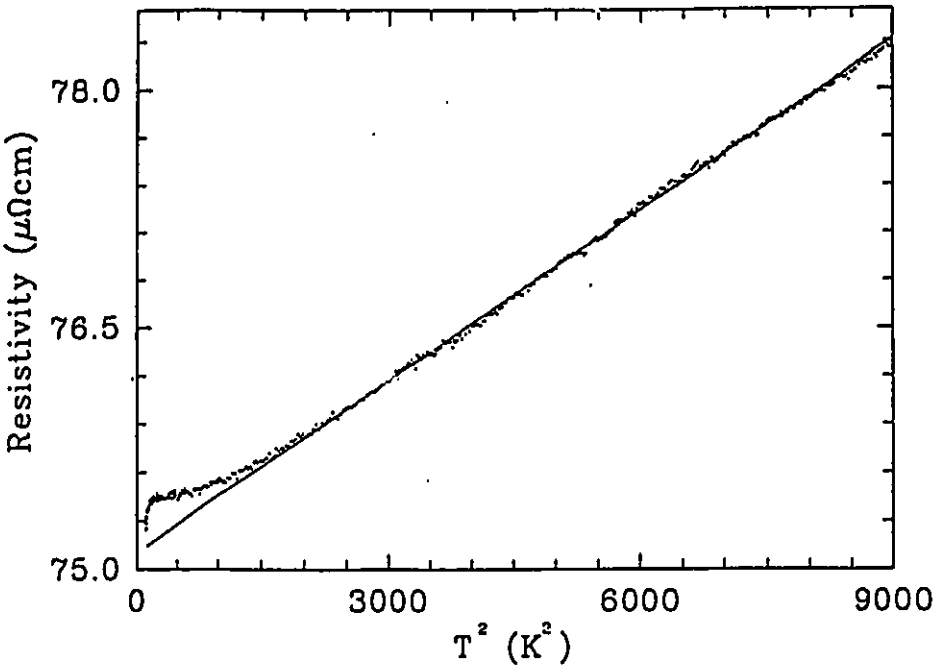

FIG. (5): Low-temperature Ziman T^2 law for Al-Cr-Fe i-alloy. The linear fit is shown by the solid line.

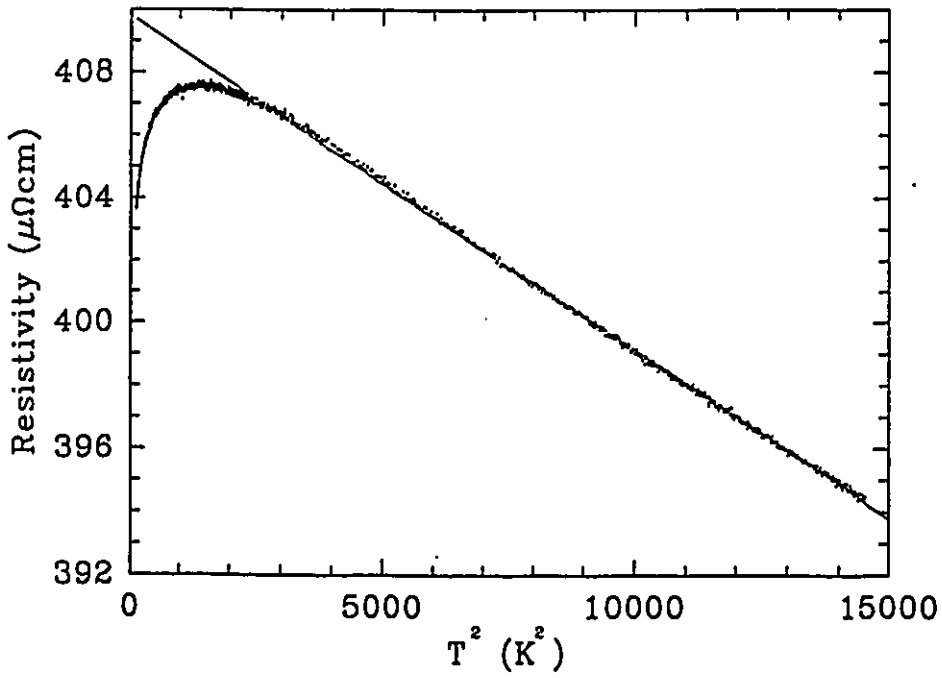

FIG. (6): Low-temperature Ziman T^2 law for Al-Ge-Cr-Fe i-alloy. The linear fit is shown by the solid line.

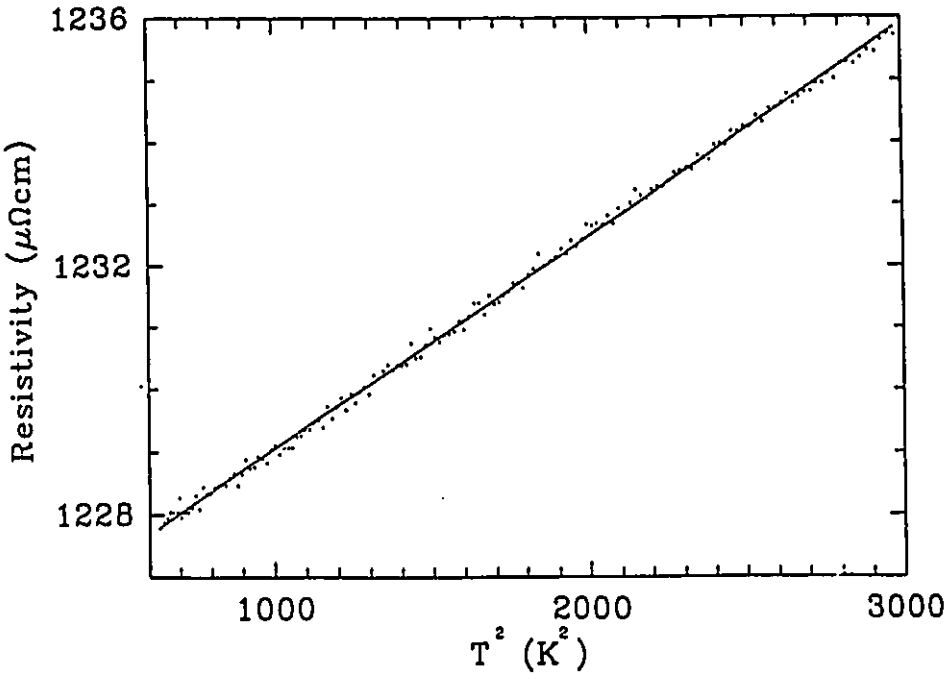

FIG. (7): Low-temperature Ziman T^2 law for Al-Pd-Fe i-alloy. The linear fit is shown by the solid line.

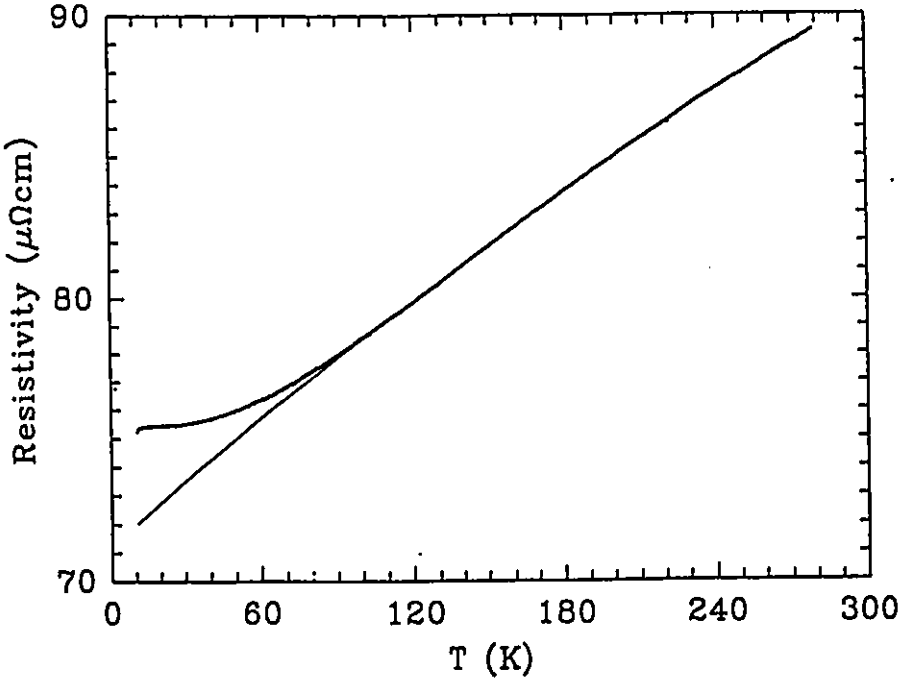

FIG. (8): High-temperature generalized Ziman dependence for Al-Cr-Fe i-alloy. The polynomial fit is shown by the solid line.

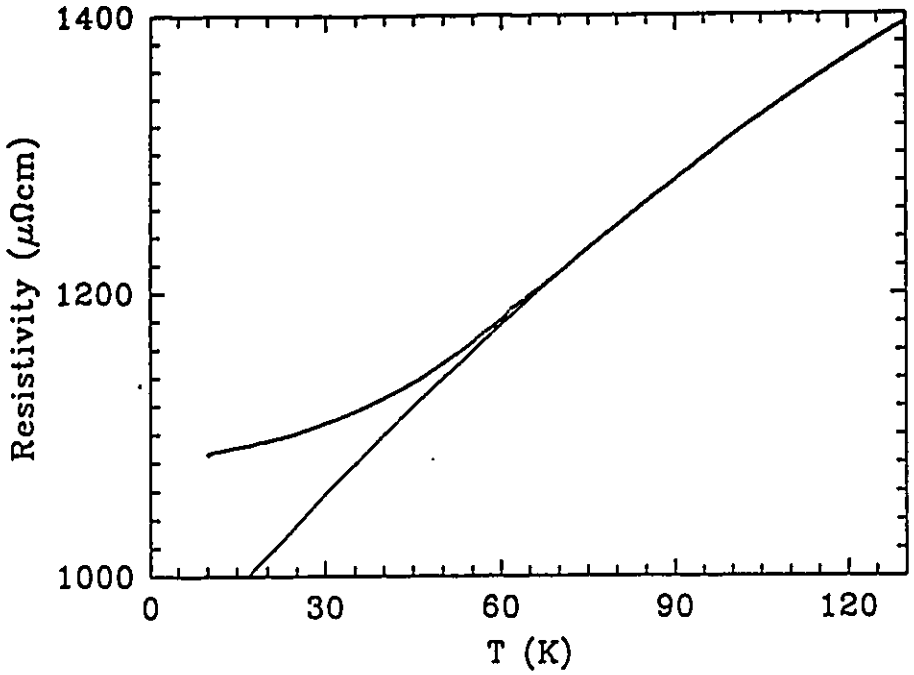

FIG. (9): High-temperature generalized Ziman dependence for Al-Cu-Mn-B i-alloy. The polynomial fit is shown by the solid line.

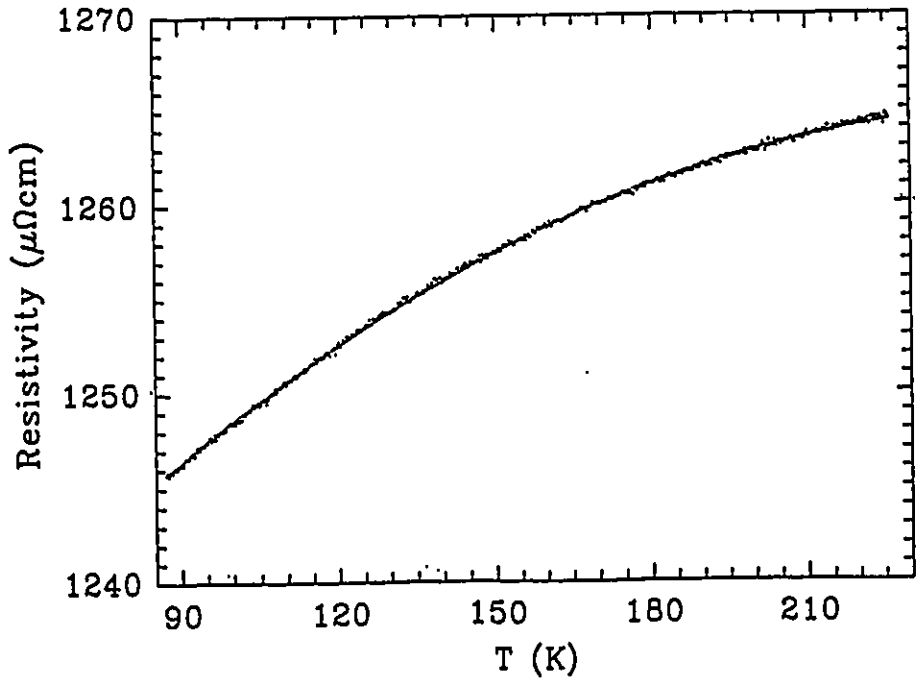

FIG. (10): High-temperature generalized Ziman dependence for Al-Pd-Fe i-alloy. The polynomial fit is shown by the solid line.

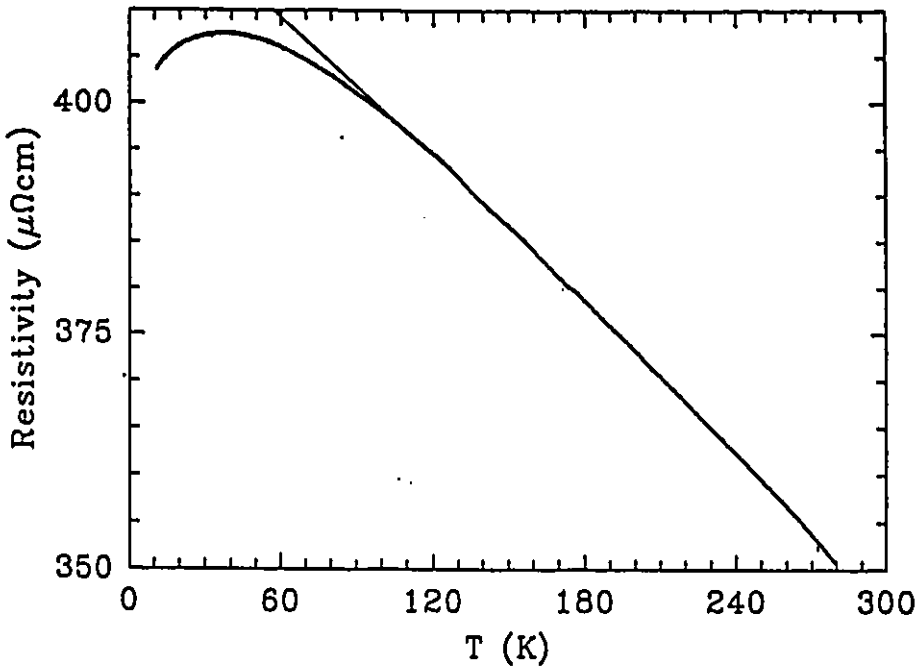

FIG. (11): High-temperature generalized Ziman dependence for Al-Ge-Cr-Fe i-alloy. The polynomial fit is shown by the solid line.

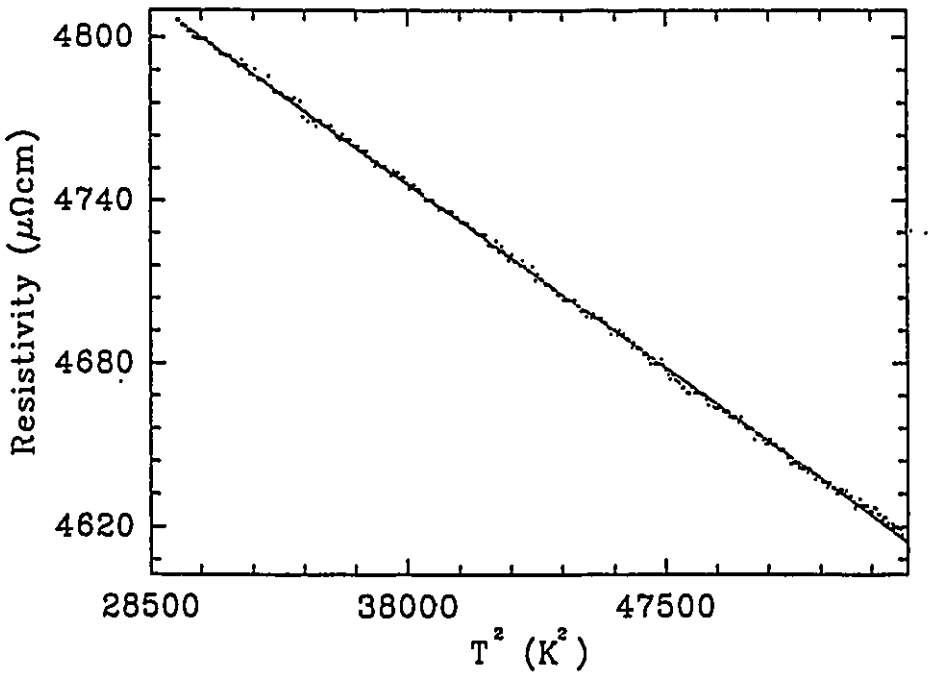

FIG. (12) High-temperature T^2 dependence of the resistivity due to the strong magnetic contribution to the resistivity in the ferromagnetic i-Al-Pd-Mn-B alloy.

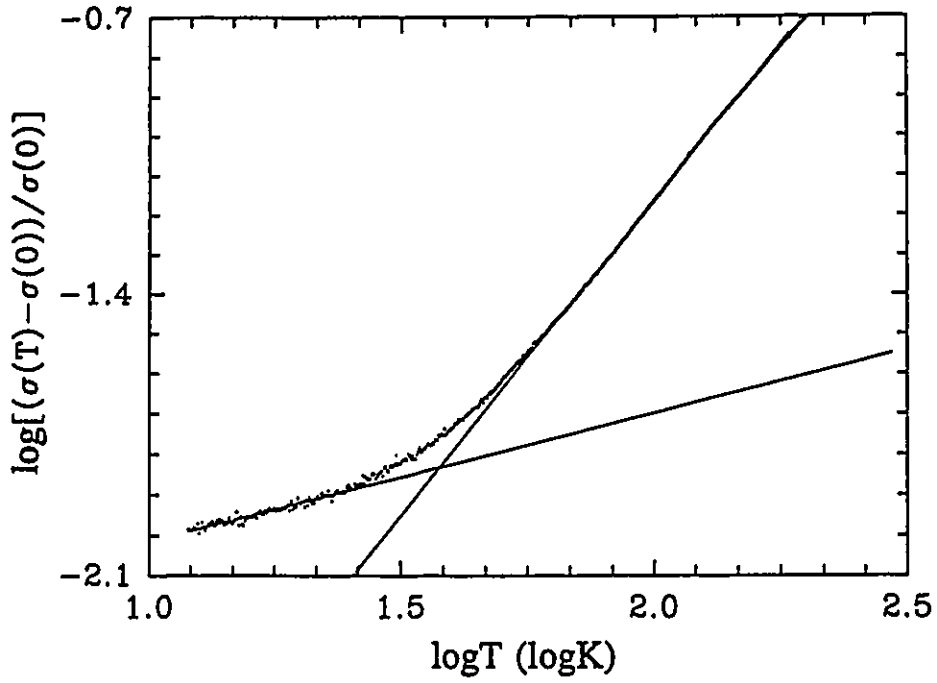

FIG. (13): Temperature dependence of the conductivity on a log-log scale for $Al_{62}Cu_{25.5}Fe_{7.5}Mn_5$ i-alloy. The linear regions indicate the power law of conductivity.

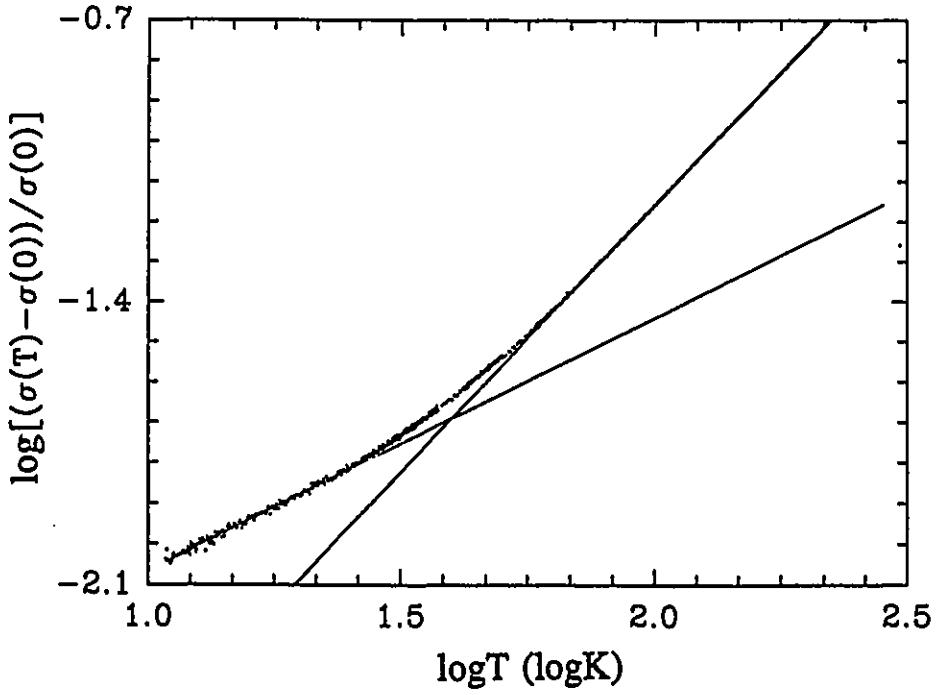

FIG. (14): Temperature dependence of the conductivity on a log-log scale for $Al_{62}Cu_{25.5}Fe_{10}Mn_{2.5}$ i-alloy. The linear regions indicate the power law of conductivity.

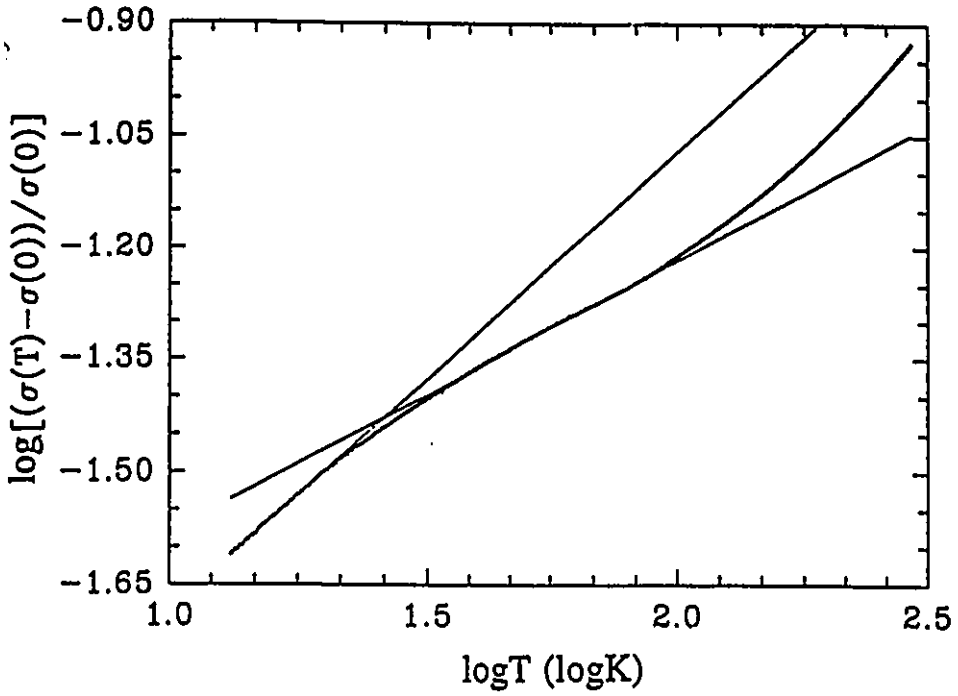

FIG. (15): Temperature dependence of the conductivity on a log-log scale for $Al_{62}Cu_{25.5}Fe_5Mn_{7.5}$ i-alloy. The linear regions indicate the power law of conductivity.

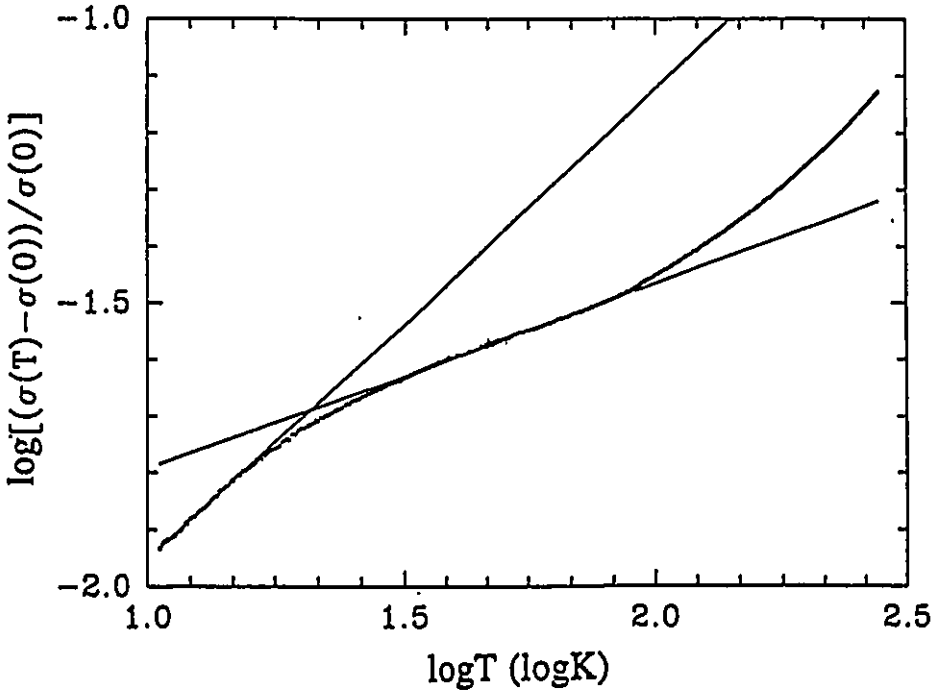

FIG. (16): Temperature dependence of the conductivity on a log-log scale for E-$Al_{62}Cu_{25.5}Fe_5Mn_{7.5}$ i-alloy. The linear regions indicate the power law of conductivity.

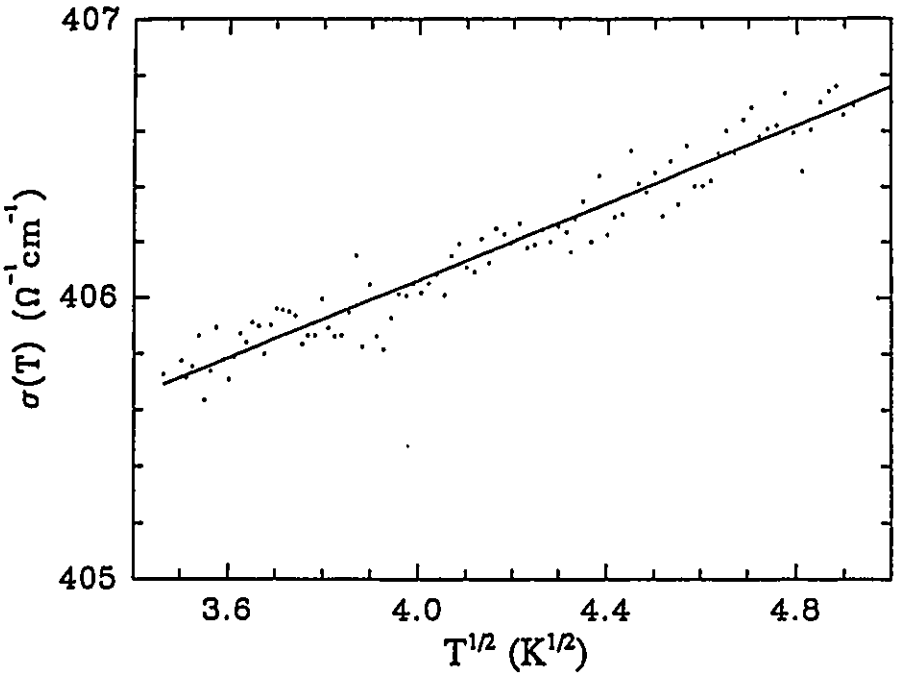

FIG. (17): Temperature dependence of the conductivity on a $T^{1/2}$ scale for $Al_{62}Cu_{25.5}Fe_{7.5}Mn_5$ i-alloy. The linear fit is shown by the solid line.

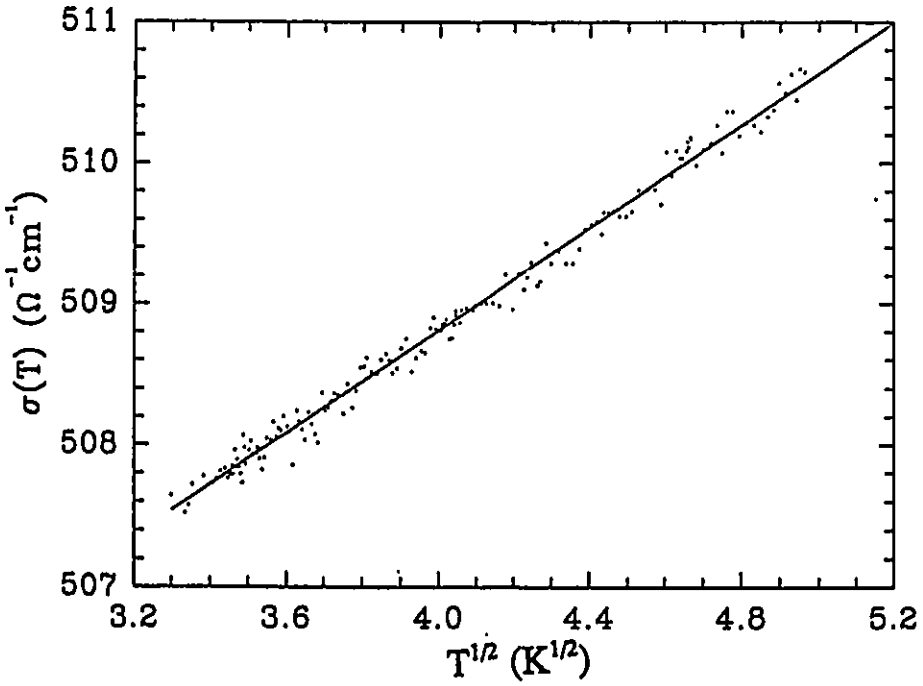

FIG. (18): Temperature dependence of the conductivity on a $T^{1/2}$ scale for $Al_{62}Cu_{25.5}Fe_{10}Mn_{2.5}$ i-alloy. The linear fit is shown by the solid line.

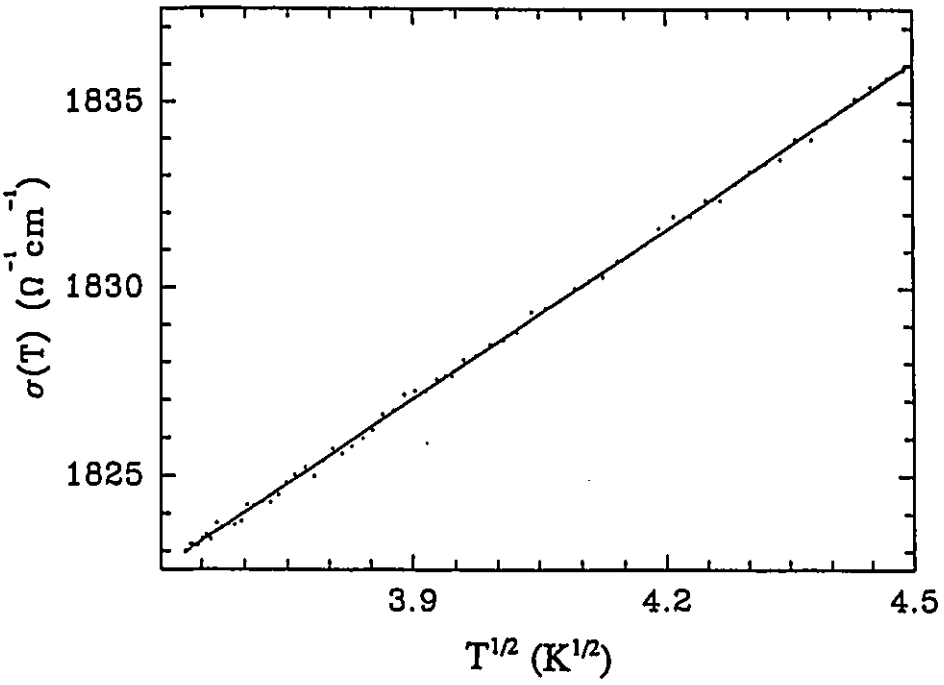

FIG. (19): Temperature dependence of the conductivity on a $T^{1/2}$ scale for $Al_{62}Cu_{25.5}Fe_3Mn_{7.5}$ i-alloy. The linear fit is shown by the solid line.

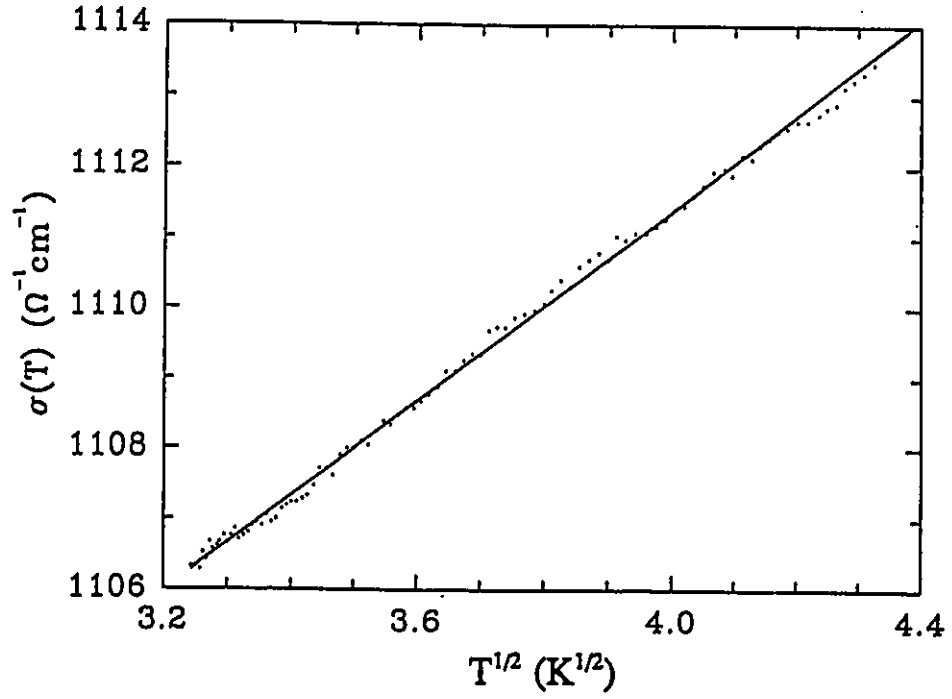

FIG. (20): Temperature dependence of the conductivity on a $T^{1/2}$ scale for E-$Al_{62}Cu_{25.5}Fe_3Mn_{7.5}$ i-alloy. The linear fit is shown by the solid line.

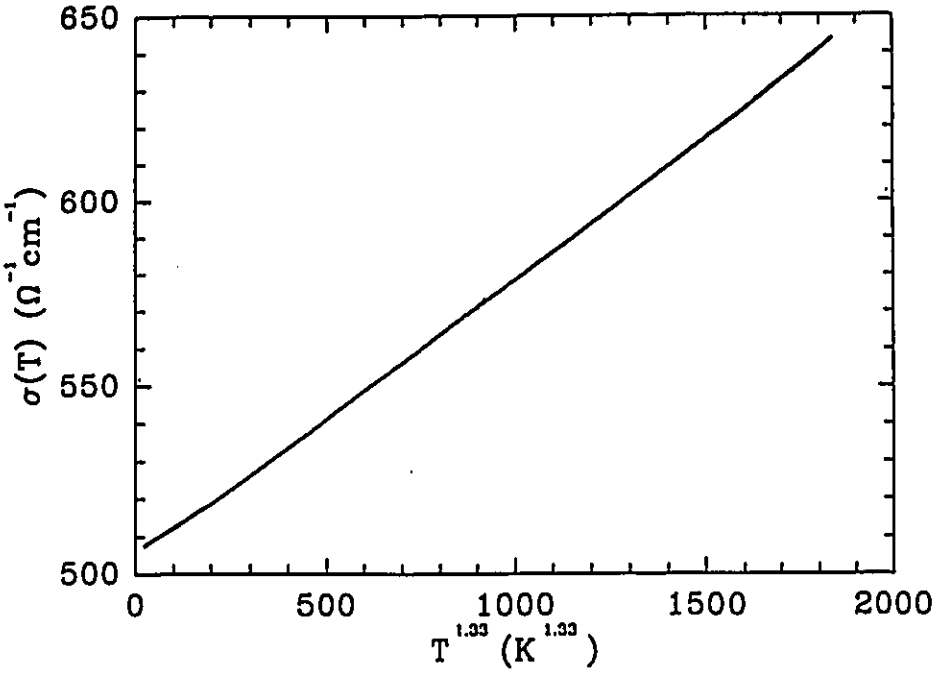

FIG. (21): Temperature dependence of the resistivity on a $T^{1.33}$ scale for $Al_{62}Cu_{25.5}Fe_{10}Mn_{2.5}$ i-alloy.

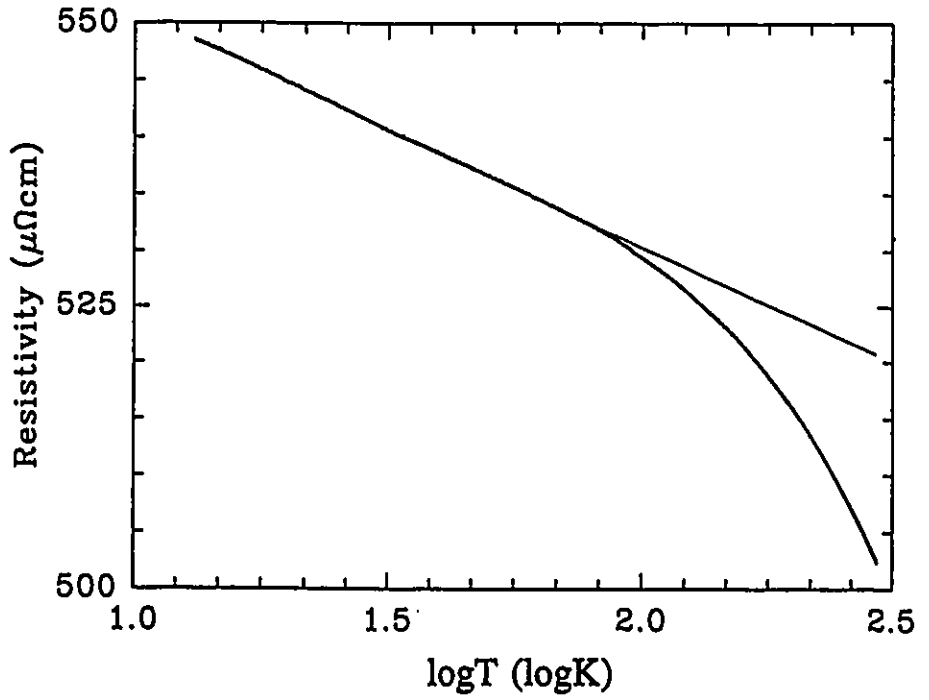

FIG. (22): Temperature dependence of the resistivity on a logT scale for $Al_{62}Cu_{25.5}Fe_3Mn_{7.5}$ i-alloy. The possible TLS effect is shown by a linear dependence on this scale. The linear fit is also shown by the solid line.

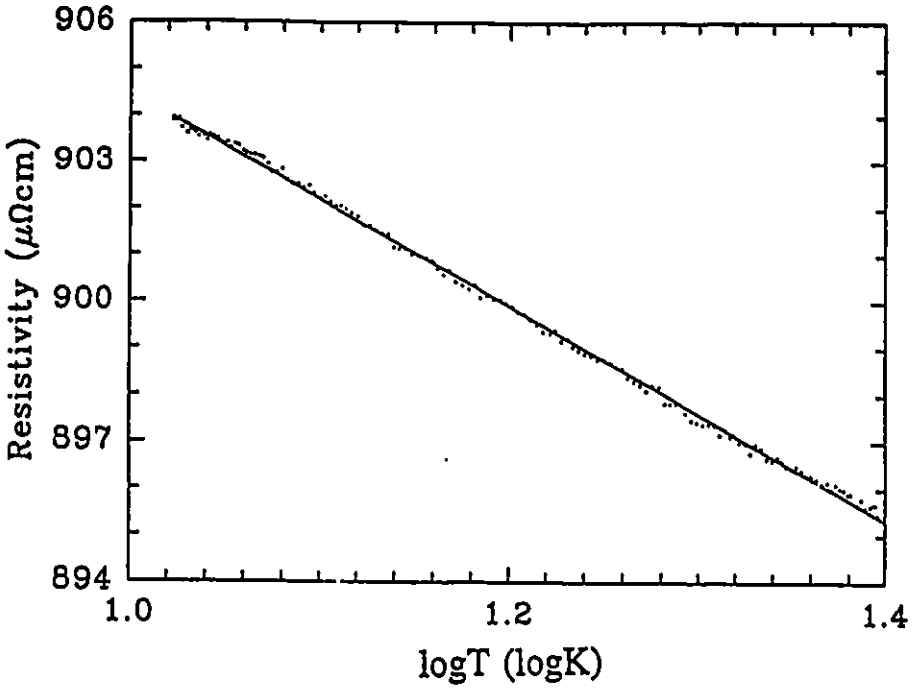

FIG. (23): Temperature dependence of the resistivity on a logT scale for E-$Al_{62}Cu_{25.5}Fe_5Mn_{7.5}$ i-alloy. The possible TLS effect is shown by a linear dependence on this scale. The linear fit is also shown by the solid line.

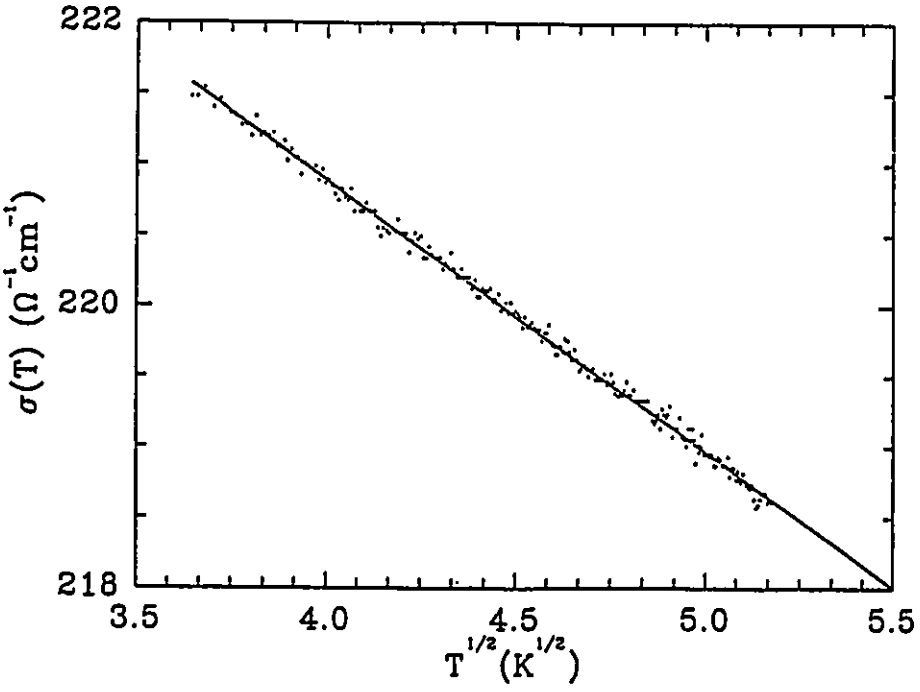

FIG. (24): The EEI effect in ferromagnetic Al-Pd-Mn-B i-alloy. The linear fit is given by the solid line.

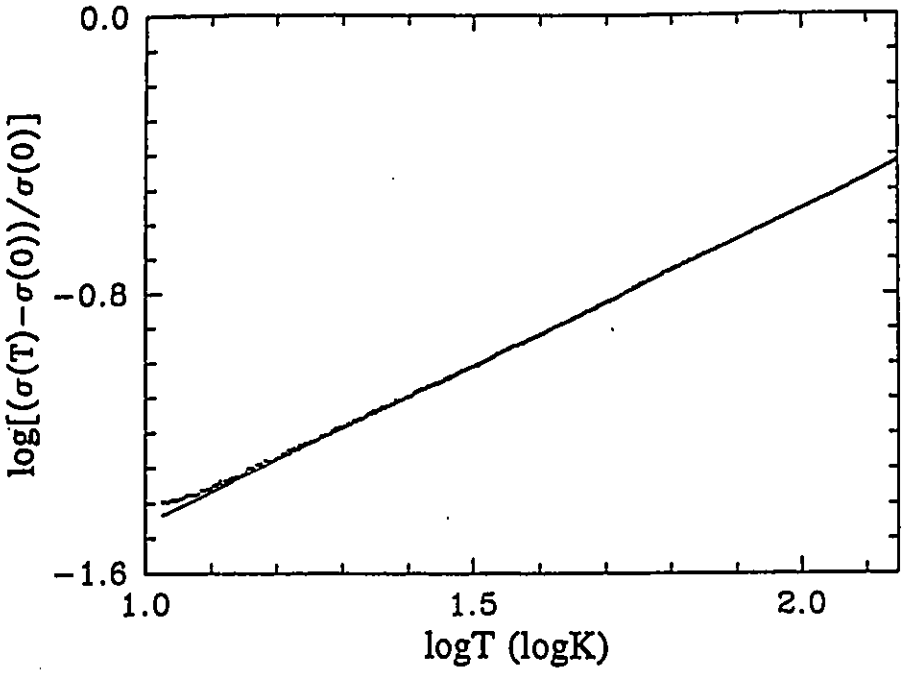

FIG. (25): Log-log plot for Al-Cu-Ru high resistivity stable i-alloy. The linear fit, which is shown by the solid line, suggests a pow law of conductivity at low temperatures

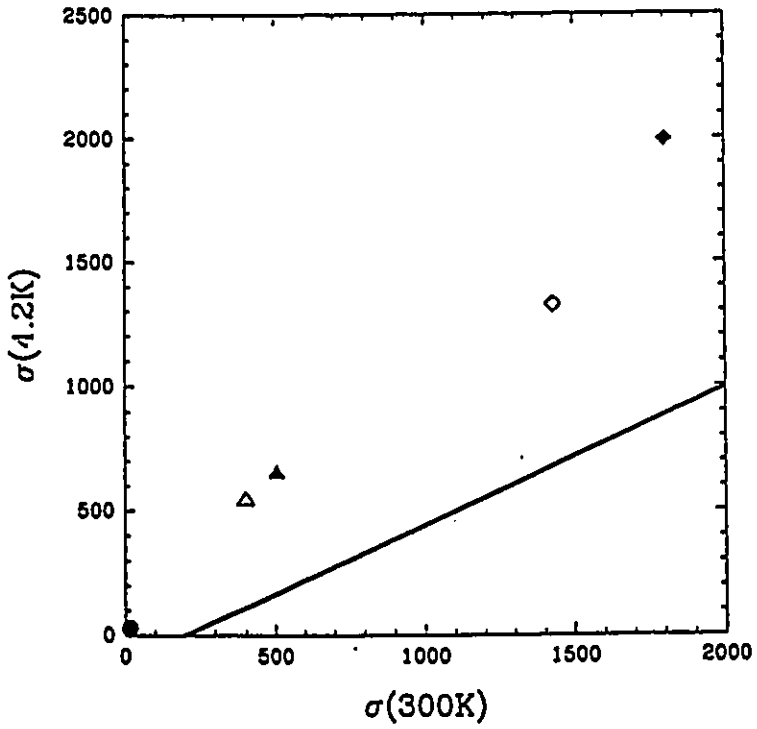

FIG. (26): The metal-insulator transition line based on Klein et al. (see the text) for (◆) $Al_{62}Cu_{25.5}Fe_3Mn_{7.5}$, (◇) etched-$Al_{62}Cu_{25.5}Fe_3Mn_{7.5}$, (▲) $Al_{62}Cu_{25.5}Fe_{10}Mn_{2.5}$, (△) $Al_{62}Cu_{25.5}Fe_{7.5}Mn_5$, and (●) Al-Cu-Ru i-alloys

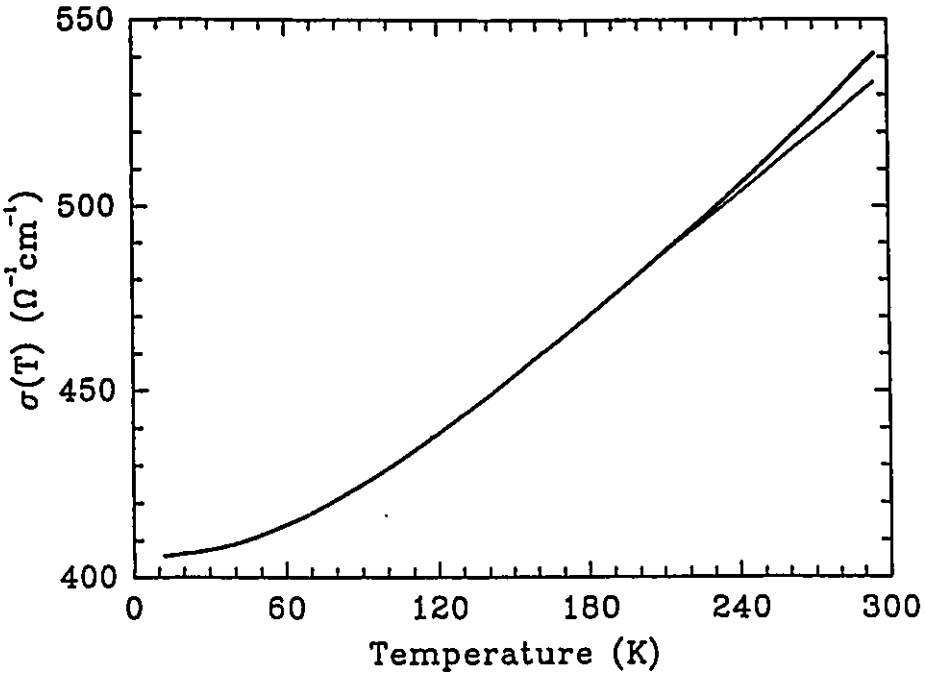

FIG. (27): Fit for $Al_{62}Cu_{25.5}Fe_{7.5}Mn_5$ i-alloy based on WL theory (including the EEI and the spin-orbit effects). The narrow line indicates the theoretical prediction and the thick line represents the experimental data.

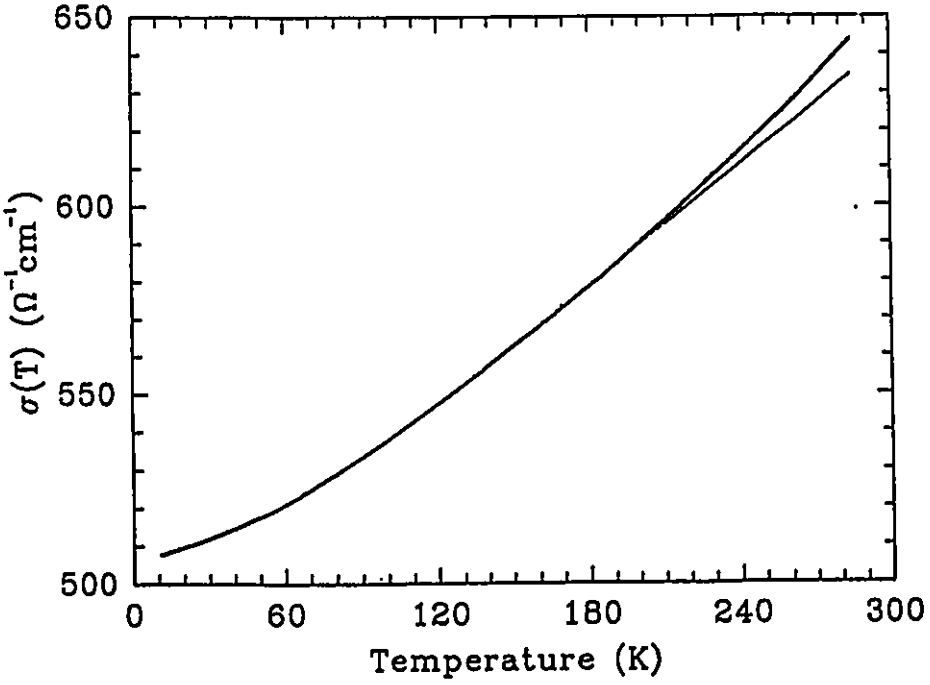

FIG. (28): Fit for $Al_{62}Cu_{25.5}Fe_{10}Mn_{2.5}$ i-alloy based on WL theory (including the EEI and the spin-orbit effects). The narrow line indicates the theoretical prediction and the thick line represents the experimental data.

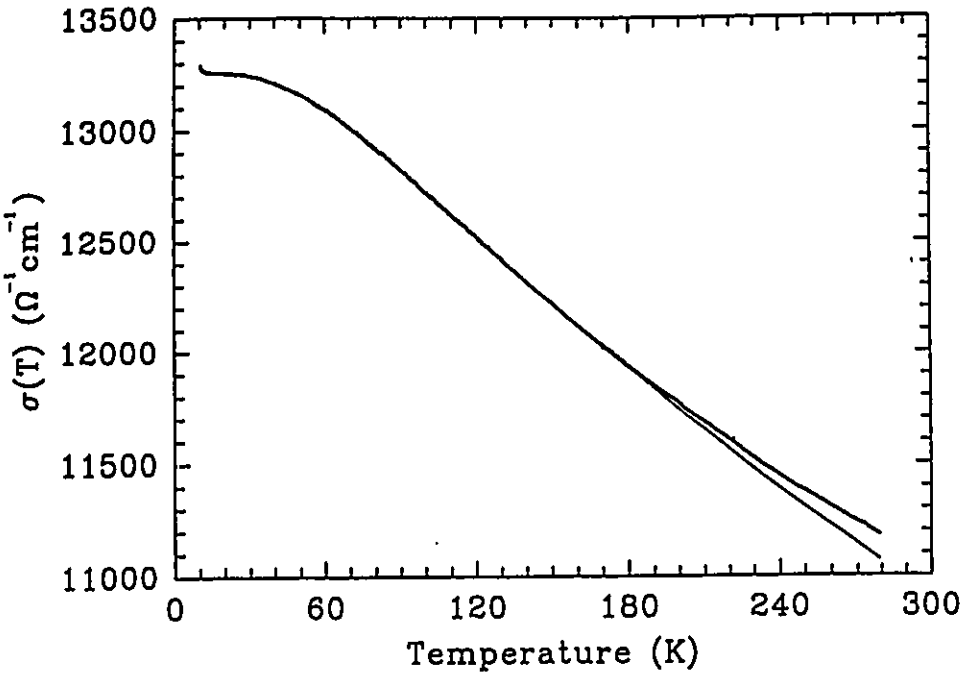

FIG. (29): Fit for Al-Cr-Fe i-alloy based on WL theory (including the EEI and the spin-orbit effects). The narrow line indicates the theoretical prediction and the thick line represents the experimental data.

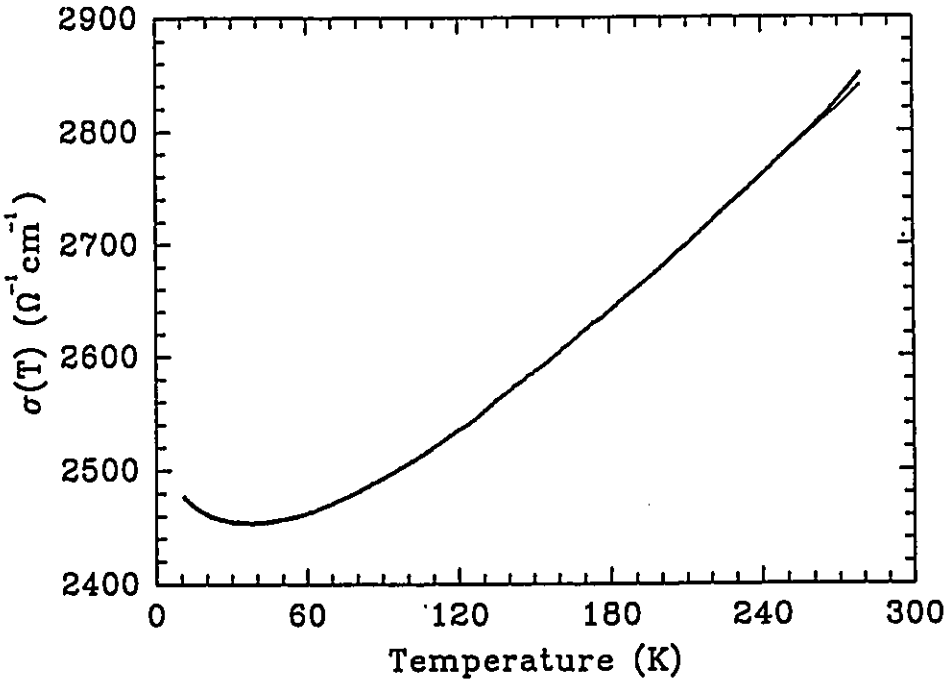

FIG. (30): Fit for Al-Ge-Cr-Fe i-alloy based on WL theory (including the EEI and the spin-orbit effects). The narrow line indicates the theoretical prediction and the thick line represents the experimental data.

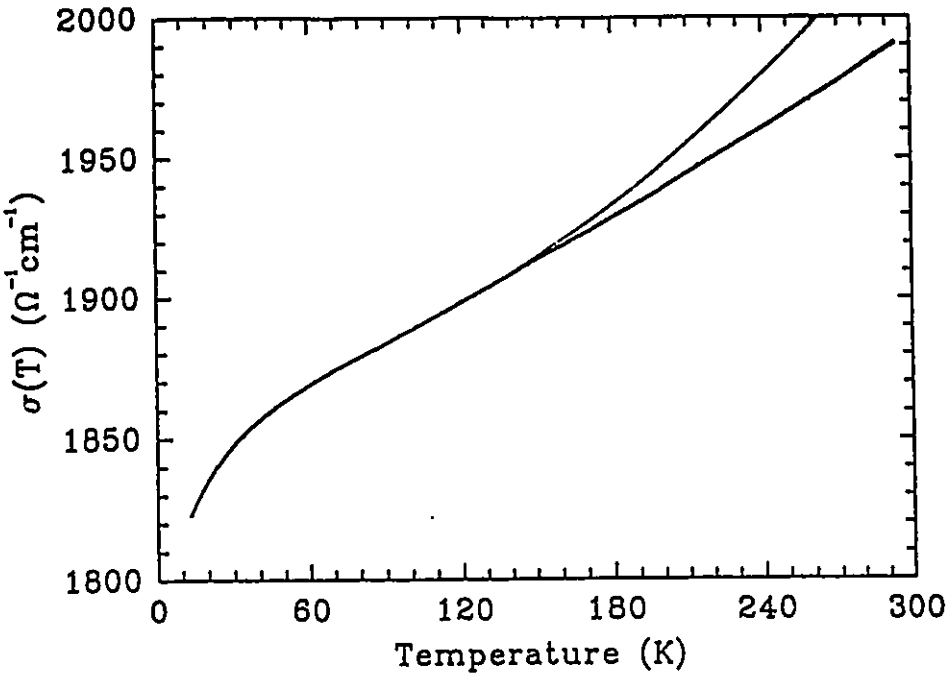

FIG. (31): Fit for $Al_{62}Cu_{25.5}Fe_5Mn_{7.5}$ i-alloy based on WL theory (including the EEI and the spin-orbit effects). The narrow line indicates the theoretical prediction and the thick line represents the experimental data.

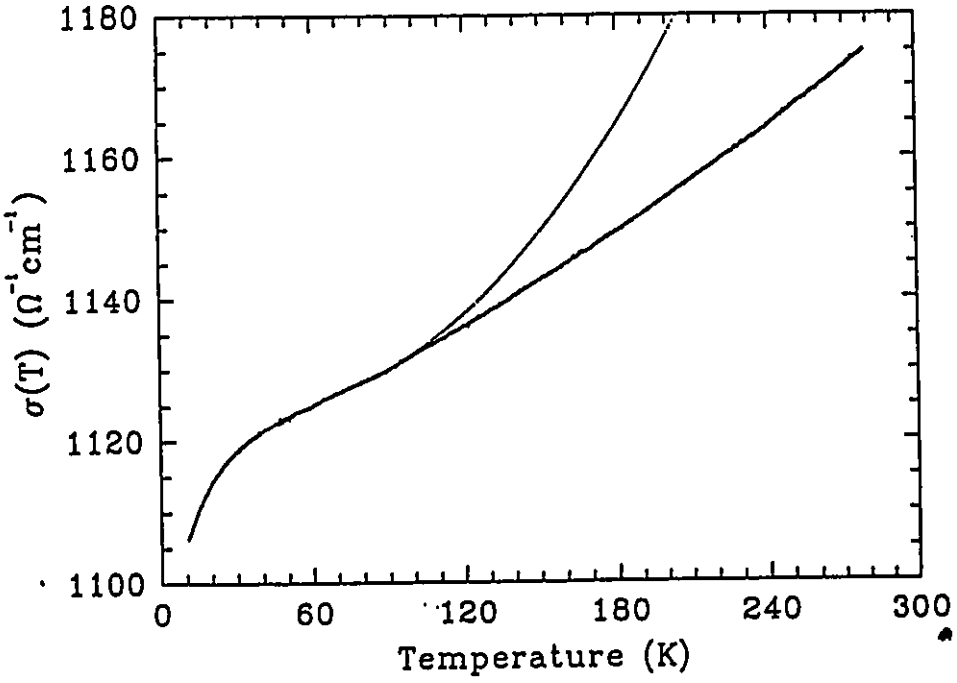

FIG. (32): Fit for E-$Al_{62}Cu_{25.5}Fe_5Mn_{7.5}$ i-alloy based on WL theory (including the EEI and the spin-orbit effects). The narrow line indicates the theoretical prediction and the thick line represents the experimental data.

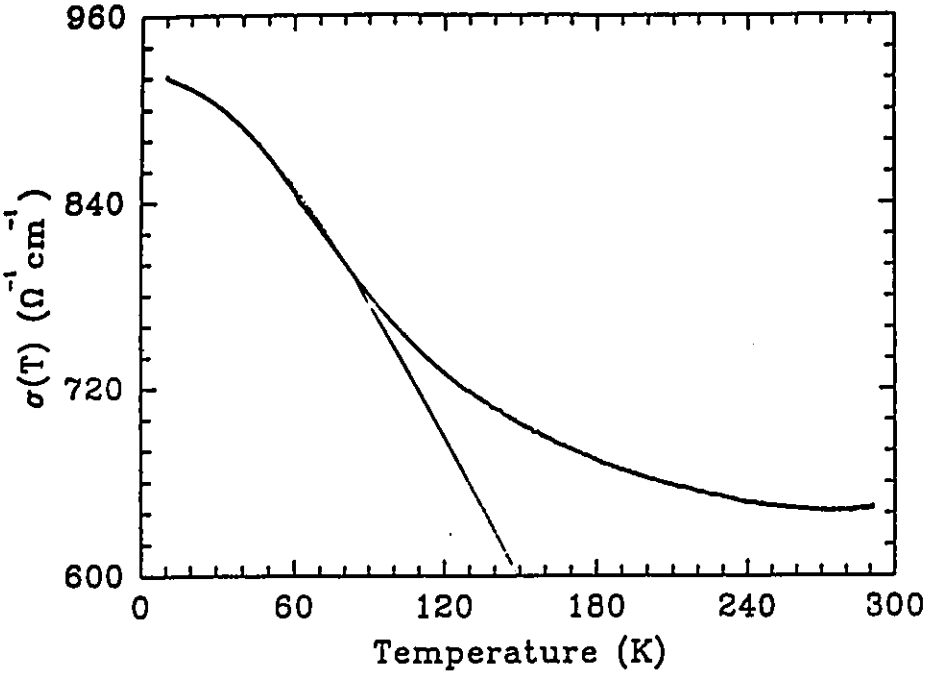

FIG. (33): Fit for Al-Cu-Mn-B i-alloy based on WL theory (including the EEI and the spin-orbit effects). The narrow line indicates the theoretical prediction and the thick line represents the experimental data.

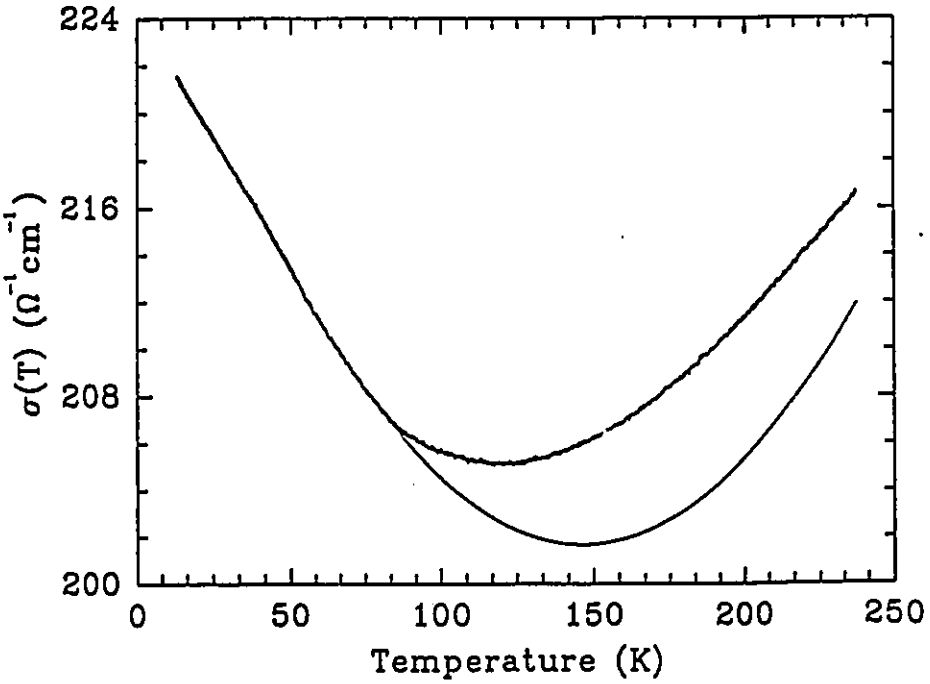

FIG. (34): Fit for Al-Pd-Mn-B i-alloy based on WL theory (including the EEI and the spin-orbit effects). The narrow line indicates the theoretical prediction and the thick line represents the experimental data.

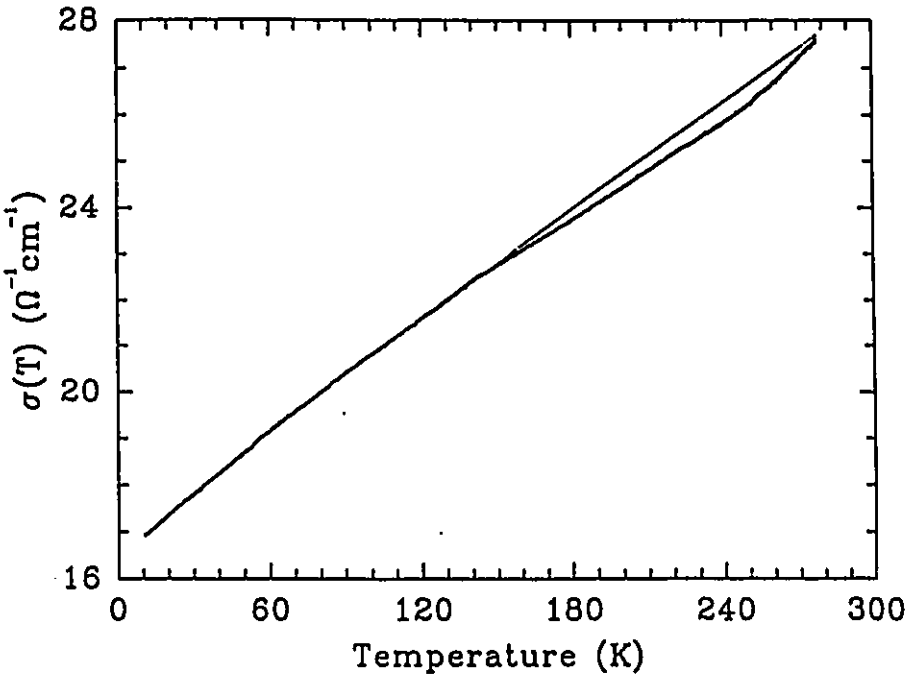

FIG. (35): Fit for Al-Cu-Ru i-alloy based on WL theory (including the EEI and the spin-orbit effects). The narrow line indicates the theoretical prediction and the thick line represents the experimental data.

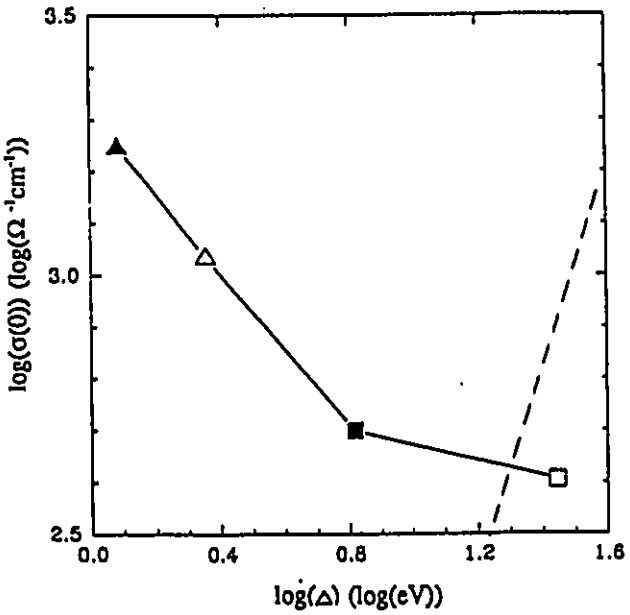

FIG. (36): Correlation plot for Al-Cu-Fe-Mn system. (▲) $Al_{62}Cu_{25.5}Fe_5Mn_{7.5}$, (△) $Al_{62}Cu_{25.5}Fe_5Mn_{7.5}$ (etched), (●) $Al_{62}Cu_{25.5}Fe_{10}Mn_{2.5}$ and (□) $Al_{62}Cu_{25.5}F_{7.5}Mn_5$. The dashed line represents the correlation for amorphous systems ($\sigma(0)=\Delta^{1/2}$).

CHAPTER 5

CONCLUSIONS

The study of the temperature dependence of the resistivity in (a), (b), and (c) type i-alloys (figures (2-A)) showed that the transport properties of these alloys can be qualitatively explained in terms of the classical theories. The low- and high-temperature variation of the resistivity is also consistent with the prediction of the extended Ziman theory. These alloys have positive TCRs associated with the relatively low resistivities. Therefore, these alloys are weak-scattering alloys in which the EEI and multiple scattering effects can be neglected.

With one exception (i-Al-Pd-Fe), the Mooij correlation holds for the studied QCs. The deviation from the Mooij correlation in the i-Al-Pd-Fe alloy is caused by the strong Mott s-d scattering which introduces a high resistivity associated with a negligibly small TCR. The strong Mott s-d scattering is also present in the studied ferromagnetic alloys.

The relation $k_p=2k_F$ (table (5)) holds for the Al-Cu-Mn-B and Al-Cr-Fe alloys, which is an indication of a strong FS-BJZ interaction in these alloys. The deduced value of the Fermi velocity for these alloys ($\sim 2\times10^8$ cm/s) (table (5)) is comparable to the free electron value (10^8 cm/s) commonly used for QCs. A large contribution to the resistivity from the magnetic channel is concluded from the enhanced magnitude of the quadratic low- and high-temperature terms in the i-Al-Cu-Mn-B alloy as compared to other alloys (tables (2,3)). In the i-Al-Pd-Mn-B ferromagnetic alloy the pronounced quadratic

temperature dependence was only detected at high temperatures.

The power law of the conductivity in the Al-Cu-Fe-Mn i-system suggests a general dependence of the form T^n for the inelastic scattering rate ($1/\tau_i$). The low-temperature dependence of the conductivity in these alloys and in the Al-Pd-Mn-B alloy is consistent with the prediction of the WL and EEI theories. The high-temperature dependence of the conductivity may be explained in terms of the temperature dependence of the charge carrier density and electron hopping models. The low-temperature dependence of the resistivity in Al-Cu-Fe-Mn_x with x=7.5 can be described by the log(T) form, the origin of which is unknown.

The low temperature analysis based on the WL and EEI theories showed that the studied i-alloys can be satisfactorily explained in terms of the quantum interference theory. The extracted low values of the electron mean-free path (table (9)) indicated that all of the studied i-alloys are highly disordered. It is concluded from the temperature dependence of the inelastic scattering rate (table (9)) that the strong electron-electron scattering is generally present for the i-Al-Cu-Fe-Mn and Al-Ge-Cr-Fe alloys, whereas for the i-Al-Pd-Mn-B alloy a weak electron-electron scattering is found. The dephasing of the quantum interference in the Al-Cr-Fe and Al-Cu-Mn-B alloys was found to be due to the electron-phonon scattering, which is similar to what is known for the low-resistivity amorphous alloys.

The resistivity maximum in the Al-Ge-Cr-Fe alloy around 30 K (figure (2-A)) and the Al-Pd-Mn-B alloy is caused by the strong spin-orbit scattering and antilocalization effect. Based on the analysis of the inelastic scattering times of the ferromagnetic alloys,

it is concluded that the magnitudes of the corresponding times can only be explained by invoking the spin scattering mechanism. The value of $\sim 10^{-13}$ s was estimated for the spin-magnon scattering time in these alloys.

The temperature dependence of the conductivity of the stable i-Al-Cu-Ru alloy can not be explained in the scope of the WL theory. However, it can be described by the variable range hopping model. It is concluded that the semimetallic behaviour observed in this alloy is responsible for the deviation from the WL theory. The vicinity of the suggested metal-insulator transition line for this alloy with respect to the Al-Cu-Fe-Mn i-system also indicates the increased density of localized states, which leads to the collapse of the Anderson localization.

It is concluded from the variation of the values of the correlation gap in the Al-Cu-Fe-Mn i-system that the nature of the pseudogap at the Fermi level is significantly different than that in an amorphous system. The correlation gap in the Al-Cu-Fe-Mn i-system was found to be strongly composition dependent. Hence, a small change in the residual resistivity can lead to an anomalously different transport behaviour.

RFERENCES

Akiyama, H., Honda, Y., Hashimoto, T., Edagawa, K., Takeuchi, S.: Jpn. J. Appl. Phys. B **32**, L1003(1993b)

Akiyama, H., Hashimoto, T., Shibuya, T., Edagawa, K., Takeuchi, S.: J. Phys. Soc. Jpn. **62**, 639(1993a)

Altshuler, B.L., Aronov, A.G.: Electron-Electron Interaction in Disordered Systems. eds. Efors, A.L., Pollak, M., North-Holand, Amsterdam 1985, p. 1

Anlage, S.M., Johnson, W.L., Cotts, E.J., Follstaedt, D.M., Knapp, J.A.: Phys. Rev. B **38**, 7802(1988)

Aronov, A.G.: Europhys. News **24**, 98(1993)

Baeck, E. Czycholl, G.: J. Phys. C **17**, 3569(1984)

Belin, E.: Physics and Chemistry of Finite Systems: From Cluster to Crystals. The Netherlands: Kluwer Academic Publishers 1992, Vol. II, p. 829

Bendersky, L.: Phys. Rev. Lett. **55**, 1461(1985)

Bieri, J.B., Fert, A., Creuzet, G., Ousset, J.C.: Solid State Commun. **49**, 849(1984)

Biggs, B.D., Poon, S.J., Munirathnam, N.R.: Phys. Rev. Lett. **65**, 2700(1990)

Biggs, B.D., Pierce, F.S., Poon, S.J.: Europhys. Lett. **19**, 415(1992)

Burkov, S.E., Timusk, T., Ashcroft, N.W.: J. Phys. Condens. Matter **4**, 9447(1992)

Carlsson, A.: Nature **353**, 15(1991)

Chen, H., Burkov, S.E., He, Y., Poon, S.J., Shiflet, G.J.: Phys. Rev. Lett. **65**, 72(1990)

Chernikov, M.A., Bernasconi, A., Beeli, C., Ott, H.R.: Europhys. Lett. **21**, 767(1993)

Cochrane, R.W., Ström-Olsen, J.O.: Phys. Rev. B **29**, 1088(1984)

Coffey, L., Muttalib, K.A., Levin, K.: Phys. Rev. Lett. **52**, 783(1984)

Dugdale, J.S.: Contemp. Phys. **28**, 547(1987)

Evans, R., Greenwood, D.A., Lloyd, P.: Phys. Lett. A **35**, 57(1971)

Frésard, R., Beck, H., Itoh, M.: J. Phys. Condens. Matter **2**, 8827(1990)

Friedel, J.: Suppl. Nuovo Cim. **7**, 287(1958)

Friedel, J.: Helv. Phys. Acta **61**, 538(1988)

Fujiwara, T.: Phys. Rev. B **40**, 942(1989)

Fujiwara, T., Yokokawa, T.: Phys. Rev. Lett. **66**, 333(1991)

Fujiwara, T., Yamamoto, S., Laissardiére, G.T.: Phys. Rev. Lett. **71**, 4166(1993)

Fujiwara, T., Laissardiére, G.T., Yamamoto, S.: Mater. Sci. Forum **150/151**, 387(1994a)

Fujiwara, T.: Mater. Sci. Forum **150/151**, 491(1994b)

Fukuyama, H., Hoshino, K.: J. Phys. Soc. Jpn. **50**, 2131(1981)

Goldman, A.I., Widom, M.: Ann. Rev. Phys. Chem. **42**, 685(1991)

Haberkern, R., Lindqvist, P., Fritsch, G.: J. Non-Cryst. Solids **153/154**, 303(1993)

Howson, M.A., Gallagher, B.L.: Phys. Rep. **170**, 265(1988)

Kaiser, A.B.: Physica Status Sol. (b) **136**, 779(1986)

Kaiser, A.B.: Phys. Rev. Lett. **58**, 1384(1987)

Kaul, S.N., Kettler, W., Rosenberg, M.: Phys. Rev. B **33**, 4987(1986)

Keithley, J.F., Yeager, J.R., Erdam, R.J.: Low Level Measurements. Cleveland, Ohio: Keithley Measurement Inc. 1984

Kimura, K., Yamane, H., Hashimoto, T., Takeuchi, S.: Mater. Sci. Forum **22-24**, 471(1987)

Kimura, K., Yamane, H., Hoshimoto, T., Takeuchi, S.: Mater. Sci. Eng. **99**, 435(1988)

Kimura, K., Hashimoto, T., Takeuchi, S.: J. Non-Cryst. Solids **117/118**, 828(1990)

Kimura, K., Takeuchi, S.: Quasicrystals, The State of the Art. edited by DiVincenzo, D.P., Steinhardt, P., Singapore: World Scientific 1991, p. 313

Kittel, C.: Introduction to Solid State Physics. New York, Chichester, Brisbane, Toronto, Singapore: John Wiley and Sons Inc. 1986

Klein, T., Berger, C., Mayou, D., Cyrot-Lackmann, F.: Phys. Rev. Lett. **66**, 2907(1991)

Kobayashi, S., Komori, F.: Suppl. Prog. Theor. Phys. No. 84, 224(1985)

Kohmoto, M., Kadanoff, L.P., Tang, C.: Phys. Rev. Lett. **50**, 1870(1983)

Kohmoto, M., Sutherland, B., Tang, C.: Phys. Rev. Lett. B **35**, 1024(1987)

Laissardière, G.T., Fujiwara, T.: Mater. Sci. Forum **150/151**, 417(1994a)

Laissardière, G.T., Fujiwara, T.: Phys. Rev. B **50**, 5999(1994b)

Lee, P.A., Ramakrishnan, T.V.: Rev. Mod. Phys. **57**, 287(1985)

Lubensky, T.C., Socolar, J.E., Steinhardt, P.J., Bancel, P.A., Heinley, P.A.: Phys. Rev. Lett. **57**, 1440(1986)

Martin, S., Hebard, A.F., Kortan, A.R., Thiel, F.A.: Phys. Rev. Lett. **67**, 719(1991)

Matsuo, S., Nakano, H., Saito, K., Mori, M., Ishimasa, T.: Solid State Commun. **86**, 707(1993)

Matsuo, S., Nakano, H., Ishimasa, T., Mori, M.: Solid State Commun. **92**, 811(1994)

Mayou, D., Berger, C., Cyrot-Lackmann, F., Klein, T., Lanco, P.: Phys. Rev. Lett. **70**, 3915(1993)

Mizutani, U.: Prog. Mater. Sci. **28**, 97(1983)

Mizutani, U., Sakabe, Sibuya, T., Kishi, K., Kimura, K., Takeuchi, S.T.: J. Phys. : Condens. Matter **2**, 6169(1990)

Mizutani, U., Kimura, K., Matsuda, T., Takeuchi, S.: Mater. Sci. Eng. A **133**, 111(1991)

Mizutani, U.: Mater. Sci. Eng. **B19**, 82(1993b)

Mizutani, U.: Current Topics in Amorphous Materials: Physics and Technology. eds. Sakurai, Y., Hamakawa, Y., Masumoto, T., Shirae, K., Susuki, K. (The Netherlands: Elsevier Science Publishers B.V. 1993a) p. 74

Moruzzi, V.L., Oelhafen, P., Williams, A.R., Lapta, P., Guntherodt, H.J., Lapka, R., Kübler, J.: Phys. Rev. B **27**, 2049(1983)

Mott, N.F., Jones, H.F.: Theory of Properties of Metals and Alloys. Oxford: Oxford Univ. Press 1936

Mott, N.F., Davis, E.A., Electronic Processes in Non-Crystalline Materials. Oxford: Clarendon Press 1971

Mott, N.F., Jones, H.: Conduction in Non-Crystalline Solids. Oxford: Clarendon Press 1987

Nakamura, Y., Mizutani, U.: Mater. Sci. Eng. **A181/A182**, 790(1994)

Naugle, D.G., Delgado, R., Armbrüster, H., Tsai, C.L., Callaway, T.O., Reynolds, D., Morruzi, V.L.: Phys. Rev. B **34**, 8279(1986)

Niizeki, K., Akamatsu, T.: J. Phys. Condens. Matter **2**, 2759(1990)

Peakfit: Jandel Scientific 1990, ver. 3.0

Peltser, W.: Research and Development. Keithley Instrument Inc. 1988, p. 80

Phillips, J.C., Rabe, K.M.: Phys. Rev. Lett. **66**, 923(1991)

Pierce, F.S., Poon, S.J., Guo, Q.: Science **261**, 737(1993a)

Pierce, F.S., Poon, S.J., Biggs, B.D.: Phys. Rev. Lett. **70**, 3919(1993b)

Pierce, F.S., Bancel, P.A., Biggs, B.D., Guo, Q., Poon, S.J.: Phys. Rev. B **47**, 5670(1993c)

Pierce, F.S., Guo, Q., Poon, S.J.: Phys. Rev. Lett. **73**, 2220(1994)

Plenet, J.C., Perez, A., Rivory, J., Frigerio, J.M., Laborde, O.: Phys. Lett. A **162**, 193(1992)

Poon, S.J.: Adv. Phys. **41**, 303(1992)

Poon, S.J.: Mater. Sci. Eng. B **19**, 72(1993)

Rajaram, G., Chandra, G., Prasad, S., Srinivas, V., Shringi, S.N., Krishnan, R.: IEEE Trans. Magn. **20**, 1347(1984)

Rapp, Ö., Bhagat, S.M., Gudmundsen, H.: Solid State Commun. **42**, 741(1982)

Rapp, Ö.: Europhys. News **24**, 102(1993)

Sadoc, A., Belin, E., Dankhazi, Z., Flank, A.M.: J. Non-Cryst. Solids **153/154**, 338(1993)

Sahnoune, A., Ström-Olsen, J.O., Zaluska, A.: Phys. Rev. B **46**, 10629(1992)

Saito, K., Matsuo, S., Nakano, H., Ishimasa, T., Mori, M.: J. Phys. Soc. Jpn. **63**, 1940(1994)

Schmid, S.: Z. Phys. **271**, 251(1974)

Shechtman, D., Blech, I., Gratias, D., Cahn, J.W.: Phys. Rev. Lett. **53**, 1951(1984)

Smith, A.P., Ashcroft, N.W.: Phys. Rev. Lett. **59**, 1365(1987)

Stadnik, Z.M., Zhang, G.W.: (Unpublished results 1995)

Takeuchi, S., Akiyama, H., Naito, N., Shibuya, T., Hashimoto, T., Edagawa, K., Kimura, K.: J. Non-Cryst. Solids **153/154**, 353(1993)

Tamura, R., Waseda, A., Kimura, K., Ino, H.: Phys. Rev. B **50**, 9640(1994a)

Tamura, R., Waseda, A., Kimura, K., Ino, H.: Mater. Sci. Eng. **A181/A182**, 794(1994b)

Tamura, R., Waseda, A., Kimura, K., Ino, H.: Proceeding of the International Conference Aperiodic Crystals, Les Diableretes, Switzerland 1994, edited by Chapuis, G. (World Scientific, Singapore, 1995), in press.

Tsai, A.P., Inoue, A., Masumoto, T.: Jpn. J. Appl. Phys. **26**, 1505(1987)

Tsai, A.P., Inoue, A., Masumoto, T.: Jpn. J. Appl. Phys. **27**, 2252(1988)

Tsuei, C.C.: Phys. Rev. Lett. **57**, 1943(1986)

Tsunetsugu, H., Udea, K.: Phys. Rev. B **43**, 8893(1991)

Wagner, J.L., Biggs, B.D., Wong, K.M., Poon, S.J.: Phys. Rev. B **38**, 7436(1988)

Wagner, J.L., Biggs, B.D., Poon, S.J.: Phys. Rev. Lett. **65**, 203(1990)

Xiao, G., Chien, C.L.: Phys. Rev. B **34**, 8430(1986)

Yokoyama, Y., Inoue, A., Masumoto, T.: Mater. Trans. Jpn. Inst. Metals **33**, 1012(1991)

Yun-ping, W., Dian-lin, Z.: Phys. Rev. B **49**, 13204(1994)

Ziman, J.M.: Philos. Mag. **6**, 1013(1961)

Ziman, J.M.: Principles of the Theory of the Solids. Cambridge: Cambridge Univ. Press 1971, 2nd ed.

APPENDIX (A)

The following program (written in basic language) has been used as a driver program to control the electronic equipment together with the IEEE digital interface. The corresponding primary and secondary address as well as the timout settings are shown for each device.

```
70  OPEN "O" ,#1, "OSON"
71  WHILE CHAR$ <> "Q"
72  CHAR$ = INKEY$
74  EOT% = 1 : EOS% = 0
87  REM
88  RM$ = SPACE$(15)
89  RN$ = SPACE$(15)
110 RL$ = SPACE$(7)
112 CALL IBCLR(DCMVOLT%)
116 BRDINDX% = 0 : PAD% = 5 : SAD% = 0 : TMO% = 14
117 EOT% = 1 : EOS% = 0
118 CALL IBDEV(BRDINDX%,PAD%,SAD%,TMO%,EOT%,EOS%,DCMVOLT%)
120 CALL IBTRG(DCMVOLT%)
125 CALL IBRD(DCMVOLT%,RM$)
126 CALL IBCLR(DCMLAMP%)
128 BRDINDX% = 0 : PAD% = 3 : SAD% = 0 : TMO% = 14
129 EOT% = 1 : EOS% = 0
130 CALL IBDEV(BRDINDX%,PAD%,SAD%,TMO%,EOT%,EOS%,DCMLAMP%)
131 CALL IBTRG(DCMLAMP%)
133 WRT$ = "ROT1G1B0"
134 CALL IBWRT(DCMLAMP%,WRT$)
135 CALL IBRD(DCMLAMP%,RN$)
136 CALL IBCLR(THERMTR%)
138 BRDINDX% = 0 : PAD% = 12 : SAD% = 0 : TMO% = 14
139 EOT% = 1 : EOS% = 0
140 CALL IBDEV(BRDINDX%,PAD%,SAD%,TMO%,EOT%,EOS%,THERMTR%)
141 CALL IBTRG(THERMTR%)
145 CALL IBRD(THERMTR%,RL$)
152 TL = VAL(RL$)
180 PRINT RM$;" ";RN$;" ";RL$
181 REM T "EXPRIMENT IS RUNNING !!!"
190 PRINT#1 ,RM$;" ";RN$
191 PRINT#1 ,RL$
200 GP% = 0
210 CALL IBONL(DCMVOLT%,GP%)
220 CALL IBONL(DCMLAMP%,GP%)
230 CALL IBONL(THERMTR%,GP%)
231 PRINT "                                        ";"EXPRIMENT IS RUNNING !!!"
240 WEND
250 CLOSE#1
260 END
```

APPENDIX (B)

The quantum correction to the conductivity is given by equations (24,25). The experimental conductivity data were fitted by the quantum corrected formula which includes the Boltzman temperature-independent term (equation 26). The $T^{1/2}$ term (the last term in the following equation) was also added for the expected EEI effect (Altshuler and Aronov 1985). The total conductivity function is related to the fit parameters by:

$$\sigma(T) = A + (B/\pi)[F_1 + F_2 - F_3 + F_4 + (1/2)E^{1/2}(F_5 + F_6)] + GT^{1/2} \quad ,$$

where T is the temperature and:

$$F_1 = -2(D/(4E))^{1/2}(T^{C/2})\times\tan^{-1}(D^{-1/2})(T^{-C/2})$$

$$F_2 = ((DT^C+4)/E)^{1/2}\times\tan^{-1}(DT^C+4)^{-1/2}$$

$$F_3 = 3((4E+DT^C+4)/E)^{1/2}\times\tan^{-1}((4E+DT^C+4)/E)^{-1/2}$$

$$F_4 = 3((4E+DT^C)/E)^{1/2}\times\tan^{-1}((4E+DT^C)/E)^{-1/2}$$

$$F_5 = \log((DT^C+5)/(DT^C+1))$$

$$F_6 = 3\log((4E+DT^C+1)/(4E+DT^C+5)).$$

The fit parameters A, B, C, D, E, and G are defined as:

$A = e^2DN(E_F) + \text{constant}$ $\qquad$ $D = 3\tau_o/\tau_{io}$

$B =$ $\qquad$ $E = 3\tau_o/\tau_{so}$

$\tau_i = \tau_{io}T^C$ $\qquad$ $G = 0.915(F_\sigma - 3/2)\sigma(0)(e^2/2\pi\hbar)(k_B/\hbar D)^{1/2}$,

where τ_{io} is the coefficient of the temperature dependence of the inelastic scattering, F_σ is the screening factor in the electron-electron interaction term (Sahnoune et al. 1992), and other parameters have their usual meanings.

The parameters A and G in the fitted function were fixed to the values based on an educated guess and the other four parameters were obtained from the fit. In this way, standard errors associated with the fitted parameters were minimized. The typical fixed parameters for Al-Ge-Cr-Fe i-alloy are A=5000 $(\Omega cm)^{-1}$ and G=29.19 $((\Omega cm)^{-1} K^{-1/2})$. The electron mean-free path was calculated from the fitted values of B and D by using the relation:

$l_e = e^2(\sqrt{D})/(2\pi^2\hbar B)$.